VILNIUS UNIVERSITY

INSTITUTE OF PHYSICS OF CENTER FOR PHYSICAL SCIENCES AND TECHNOLOGY

RŪTA MACKEVIČIŪTĖ

ELECTRICAL INVESTIGATION OF THIN FERROELECTRIC FILMS AND NANO STRUCTURES

Doctoral dissertation

Physical sciences, Physics (02P)

Vilnius, 2017

The thesis was prepared at Vilnius University (Vilnius, Lithuania) in 2013 – 2017.

Scientific supervisor:

Prof. dr. Robertas Grigalaitis (Vilnius University, Physical sciences, Physics 02P).

Acknowledgments

This dissertation is a result of my work done during doctoral studies in Vilnius University – collaboration with many people who helped me on different parts of this work. I would like to acknowledge all of them.

First of all, huge gratitude to my scientific supervisor prof. Robertas Grigalaitis for supervision and help in achieving the goal of getting results and writing the thesis.

Furthermore, sincere gratitude to prof. habil. dr. Jūras Banys for the invitation to Phase transition laboratory, advices and help throughout the years in the laboratory.

Also, I would like to thank all scientist and students for valuable discussions, collaboration in various projects, help with experiments: dr. Šarūnas Bagdzevičius, dr. Maksim Ivanov, dr. Edita Palaimienė, prof. Vytautas Samulionis, dr. Jan Macutkevič, dr. Andrius Džiaugys, dr. Martynas Kinka, dr. Saulius Rudys, PhD students Jaroslavas Belovickis, Ieva Kranauskaitė, Mantas Šimėnas, Džiugas Jablonskas, Šarūnas Svirskas, Ilona Zamaraitė and Sergejus Balčiūnas.

The most important gratitude to my family and friends for the infinite understanding and moral support during my PhD studies.

Table of Contents

1. Introduction

Today widely used ferroelectrics are investigated since the discovery of the ferroelectricity in Rochelle salt in 1920. The main property of ferroelectrics is appearance of spontaneous polarization at certain temperature, which direction can be changed by an external electric field. Ferroelectrics and related materials, such as ferroelectric relaxors, are widely investigated class of materials due to both scientific and engineering point of view. From scientific point of view, there is a variety of different phenomena taking place in both bulk and nanoscale materials. Formation of domain walls, stresses, interface effects are just a few of the most interesting topics. Meanwhile, from engineering point of view ferroelectric materials are attractive because of their high dielectric constant, low dielectric loss, good thermal stability, and good high frequency characteristics. These properties allow producing high density dynamic random access memories, IR detectors, tunable microwave devices, humidity and gas sensors and etc. It is important to notice that modern technologies are driven towards in order to minimize devices. For this reason, it is very important to understand, how properties of ferroelectric materials changes in nanoscale.

Real ferroelectric materials have internal electric fields due to finite size, charged defects, and inhomogeneities in the material. This is even more pronounced in thin films. These inevitable fields are often considered a hurdle, typically causing degradation of properties. Several recent studies showed strongly enhanced properties (piezoelectric, dielectric, photovoltaic) originating from internal fields, hinting that internal fields could be beneficial if properly addressed. This triggered to propose the present thesis, in which all attention was dedicated for understanding of internal fields in ferroelectrics. So, in this work, electrical investigation of thin ferroic films and nanostructures are presented. Here, heterostructure of $Ba_{0.7}Sr_{0.3}TiO_3$ / $La_{0.8}Sr_{0.2}MnO_3$ // $SrTiO_3$ and $Ba_{0.7}Sr_{0.3}TiO_3$ / $SrRuO_3$ // $SrTiO_3$ where investigated and also, $0.71Pb(Mg_{1/3}Nb_{2/3})O_3 - 0.29PbTiO_3$ single crystals oriented and poled along

three different crystallographic directions and $0.67Pb(Mg_{1/3}Nb_{2/3})O_3 - 0.33PbTiO_3$ epitaxial thin films were analysed in a broad temperature and frequency ranges. The impedance analysis of the complex $Ba_{0.7}Sr_{0.3}TiO_3$ heterostructure allowed to present the model of a thin dielectric film with a bottom electrode of negligible distributed resistance, which in a physical proper way describes a situation when the dispersions of complex impedance, observed in thin film and bottom electrode, are overlapped and cannot be separated in order to perform further analysis. This theoretical model was verified for complicated thin film heterostructure where leaky functional layer and bad conduction of electrode layer is met. Dielectric and complex impedance measurements were performed in 20 Hz – 1 MHz frequency and 300 – 500 K temperature ranges. Meanwhile, pyroelectric measurements were investigated in 220 – 420 K temperature intervals.

1.1. The aim and tasks of the work

The aim of this thesis is to investigation electrical properties of epitaxial $Ba_{0.7}Sr_{0.3}TiO_3$ and $0.67Pb(Mg_{1/3}Nb_{2/3})O_3 - 0.33PbTiO_3$ thin film heterostructures and $0.71Pb(Mg_{1/3}Nb_{2/3})O_3 - 0.29PbTiO_3$ single crystals in a broad temperature and frequency ranges.

The tasks of dissertation are:

1. To investigate a complex thin film heterostructure, where leaky functional layer and low conduction of electrode layer are met.
2. Experimentally investigate misfit strain, between substrate crystal lattice and film crystal lattice, influence on $Ba_{0.7}Sr_{0.3}TiO_3$ phase transition temperature, dielectric properties and electric field tunability.
3. To investigate the dielectric properties of $0.71Pb(Mg_{1/3}Nb_{2/3})O_3 - 0.29PbTiO_3$ single crystals and epitaxial $0.67Pb(Mg_{1/3}Nb_{2/3})O_3 - 0.33PbTiO_3$ thin film.

In all cases investigation was meant to be performed by means of broadband dielectric spectroscopy.

1.2. Scientific novelty

1. The model of a thin dielectric film with a bottom electrode of negligible distributed resistance was developed and verified for complicated thin film heterostructure. It was found that this model is applicable in the cases when the dispersions of complex impedance, observed in thin film and bottom electrode, are overlapped and cannot be separated in order to perform further analysis.
2. The effectiveness of characterized theoretical model was presented by approximation of experimental data of epitaxial $Ba_{0.7}Sr_{0.3}TiO_3$ thin film. It was shown that the model of a thin dielectric film with a bottom electrode of negligible distributed resistance describes the experimental data in a physically proper way, unlike equivalent circuit model.
3. Epitaxial $Ba_{0.7}Sr_{0.3}TiO_3$ thin film was investigated in 20 Hz – 1 MHz frequency, 300 – 500 K temperature and -1 MV/cm – 1 MV/cm electric field ranges. The influence of misfit strain to phase transition temperature and activation energy was investigated.
4. Pyroelectric properties of $0.71Pb(Mg_{1/3}Nb_{2/3})O_3 – 0.29PbTiO_3$ single crystals oriented and poled along three different crystallographic directions, <001>, <011> and <111> were investigated in 220 – 420 K temperature range.
5. The investigation of specific impedance and electrical field tunability of epitaxial $0.67Pb(Mg_{1/3}Nb_{2/3})O_3 – 0.33PbTiO_3$ thin film was presented in 20 Hz – 1 MHz frequency, 300 – 500 K temperature and in -100 kV/cm – 100 kV/cm electric field ranges, respectively.

1.3. Statements presented for defence

1. The model of a thin dielectric film with a bottom electrode of negligible distributed resistance characterizes complicated epitaxial heterostructure in a physically proper way.

2. The values of dielectric permittivity of epitaxial $Ba_{0.7}Sr_{0.3}TiO_3$ and $0.67Pb(Mg_{1/3}Nb_{2/3})O_3 - 0.33PbTiO_3$ thin films diminishes comparing with their bulk material.
3. Either built in electric or misfit strain field do not deteriorate dielectric tunability of epitaxial $Ba_{0.7}Sr_{0.3}TiO_3$ and $0.67Pb(Mg_{1/3}Nb_{2/3})O_3 - 0.33PbTiO_3$ thin films.

1.4. Author's contribution

The author of this dissertation carried out the impedance and dielectric spectroscopy, electric field tunability and ferroelectric hysteresis measurements of epitaxial $Ba_{0.7}Sr_{0.3}TiO_3$ and $0.67Pb(Mg_{1/3}Nb_{2/3})O_3 - 0.33PbTiO_3$ thin film heterostructures. Moreover, she carried out the dielectric spectroscopy and pyroelectric measurements of $0.71Pb(Mg_{1/3}Nb_{2/3})O_3 - 0.29PbTiO_3$ single crystals. She has also analysed the results and prepared manuscripts of most publications. The author has prepared presentations for the conferences and most of them she has presented herself.

A part of results were obtained in collaboration with partners from other institutions. The preparation of $Ba_{0.7}Sr_{0.3}TiO_3$ heterostructures were conducted in Ecole Polytechnique Federale De Lausanne (Switzerland). $0.67Pb(Mg_{1/3}Nb_{2/3})O_3 - 0.33PbTiO_3$ thin film heterostructures were prepared in University of Twente (Netherlands). Meanwhile, $0.71Pb(Mg_{1/3}Nb_{2/3})O_3 - 0.29PbTiO_3$ single crystals oriented along three different crystallographic directions, <001>, <011> and <111> were supplied by H.C. Materials Corporation (USA). XRD and PFM measurements were conducted in Ecole Polytechnique Federale De Lausanne (Switzerland).

1.5. Articles published in the topic of dissertation

1. **R. Mackeviciute, R. Grigalaitis, M. Ivanov, R. Sliteris, and J. Banys**, Dielectric and Pyroelectric Properties of PMN29PT Single Crystals Near

MPB. Ferroelectrics, 479, 1–6 (2015): http://dx.doi.org/10.1080/00150193.2015.1008382

2. **R. Mackevičiūtė, M. Ivanov, Š. Bagdzevičius, R. Grigalaitis, J. Banys**, Electrical model of a thin dielectric film with a bottom electrode of non-negligible distributed resistance. Ferroelectrics, 497, 114–125 (2016): http://dx.doi.org/10.1080/00150193.2016.1165023
3. **S. Bagdzevicius, R. Mackeviciute, M. Ivanov, B. Fraygola, C. S. Sandu, N. Setter, and J. Banys**, Internal electrical and strain fields influence on the electrical tunability of epitaxial $Ba_{0.7}Sr_{0.3}TiO_3$ thin films. Appl. Phys. Lett. 108, 132901 (2016): http://dx.doi.org/10.1063/1.4944997
4. **R. Mackevičiūtė, Š. Bagdzevičius, M. Ivanov, B. Fraygola, R. Grigalaitis, N. Setter, and J. Banys**, Strain engineering of electrical conductivity in epitaxial thin $Ba_{0.7}Sr_{0.3}TiO_3$ film heerostructures. Lith. J. Phys. 56, 173–181 (2016): http://dx.doi.org/10.3952/physics.v56i3.3366
5. **R. Mackeviciute, R. Grigalaitis, J. Banys, M. Boota, A. Ghosh, and G. Rijnders**, Electrical properties of PMN-33PT thin film at MPB. Submitted in Ferroelectri: http://dx.doi.org/ 10.1080/00150193.2017.1355140

1.6. Other publications

1. **F. B. Tahar, C. Hrizi, S. Chaabouni, N. C. Boudjada, N. R. Ramond, S.s Balčiūnas, M. Ivanov, R. Mackevičiūtė, J. Banys, R. Chtourou**, Synthesis, Crystal structure, Vibrational, Optical and Dielectric properties Of 2-(2-Aminoethyl)-1-methylpyrrolidinum chloride hexachlorobismuthate (III) monohydrate $[C_7H_{18}N_2]_2ClBiCl_6.H_2O$. Journal of Advances in Chemistry, 9, 3 (2014)
2. **R. Mackeviciute , V. Goian , S. Greicius , R. Grigalaitis, D. Nuzhnyy, J. Holc , J. Banys , S. Kamba**, Lattice dynamics and broadband dielectric properties of multiferroic $Pb(Fe_{1/2}Nb_{1/2})O_3$ ceramics, J. Appl. Phys. 117, 8 (2015): http://dx.doi.org/10.1063/1.4913286

1.7. Presentations at conferences

1. **R. Mackeviciute**, J. Banys, P. Szklarz. „Dielectric properties of diammonium hypodiphosphate $(NH_4)_2H_2P_2O_6$ (ADhP)“, European Conference on Application of Polar Dielectrics 2014 (ECAPD), Vilnius, Lietuva, 07 – 11 of June 2014
2. **R. Mackeviciute**, R. Grigalaitis, M. Ivanov, R. Sliteris, J. Banys. „Dielectric and pyroelectric properties of PMN-29PT single crystal near MPB”, European Conference on Application of Polar Dielectrics 2014 (ECAPD), Vilnius, Lietuva, 07 – 11 of June 2014
3. **R. Mackeviciute**, J. Banys, P. Szklarz, „Dielectric properties of diammonium hypodiphosphate $(NH_4)_2H_2P_2O_6$ (ADhP)“, III Polish-Lithuanian-Ukrainian Meeting on Ferroelectrics Physics (PLU 2014), Wroclaw – Pawlowice, Poland, 31 of August – 04 of September 2014
4. **R. Mackeviciute**, R. Grigalaitis, M. Ivanov, R. Sliteris, J. Banys „Dielectric and pyroelectric properties of PMN-29PT single crystal near MPB”, III Polish-Lithuanian-Ukrainian Meeting on Ferroelectrics Physics (PLU 2014), Wroclaw – Pawlowice, Poland, 31 of August – 04 of September 2014
5. **R. Mackeviciute**, J. Banys, P. Szklarz, „Dielectric properties of diammonium hypodiphosphate $(NH_4)_2H_2P_2O_6$ (ADhP)“, Russia/CIS/Baltic/Japan Symposium on Ferroelectricity – 2014 – Functional Materials and Nanotechnologies (RCBJSF – 2014 – FM&NT), Riga, Latvia, 29 of September – 02 of October 2014
6. S. Bagdzevicius, R. Mackeviciute, N. Setter, J. Banys, "Structural and Electrical Characterization of Epitaxially Strained $Ba_{0.7}Sr_{0.3}TiO_3$”, Russia/CIS/Baltic/Japan Symposium on Ferroelectricity – 2014 – Functional Materials and Nanotechnologies (RCBJSF – 2014 – FM&NT), Riga, Latvia, 29 of September – 02 of October 2014
7. **R. Mackevičiūtė**, Š. Bagdzevičius, M. Ivanov, R. Grigalaitis, and J. Banys, „Complex impedance spectroscopy of $Ba_{0.7}Sr_{0.3}TiO_3$ thin films“, 13th

European Meeting on Ferroelectricity (EMF 2015), Porto, Portugal, 28 of June – 03 of July 2015

8. **R. Mackevičiūtė**, Š. Bagdzevičius, M. Ivanov, R. Grigalaitis, and J. Banys, „Complex impedance spectroscopy of $Ba_{0.7}Sr_{0.3}TiO_3$ thin films“, International School of Oxide Electronics 2015, Cargèse, Corsica (France), 12 – 24 of October 2015
9. **R. Mackeviciute**, R. Grigalaitis, J. Banys, M. Boota, A. Ghosh, and G. Rijnders, "Electrical properties of $Pb(Mg_{1/3}Nb_{2/3})O_3$-$33PbTiO_3$ thin film at MPB", 13th Russia/CIS/Baltic/Japan Symposium on Ferroelectricity nad 8th International Workshop on Relaxor Ferroelectrics (Joint RCBJSF-IWRF 2016 Conference), Shimane, Japan, 19 – 23 of June 2016
10. R. Mackevičiūtė, R. Grigalaitis, Š. Bagdzevičius, M. Ivanov, B. Fraygola, N. Setter, J. Banys, "Electrical conductivity studies in partially strained epitaxial thin $Ba_{0.7}Sr0_3TiO_3$ films", 13th Russia/CIS/Baltic/Japan Symposium on Ferroelectricity nad 8th International Workshop on Relaxor Ferroelectrics (Joint RCBJSF-IWRF 2016 Conference), Shimane, Japan, 19 – 23 of June 2016

2. Overview

2.1. The perspectives of crystal structural symmetry

2.1.1. Hierarchic classification of crystalline materials

According to Neumann's principle [B.1], symmetry elements of all physical properties in a crystal should include all symmetry elements of the point group of this crystal. Thus, if a physical parameter is subjected to a symmetry operation of the crystal, the value of this physical parameter should remain invariant.

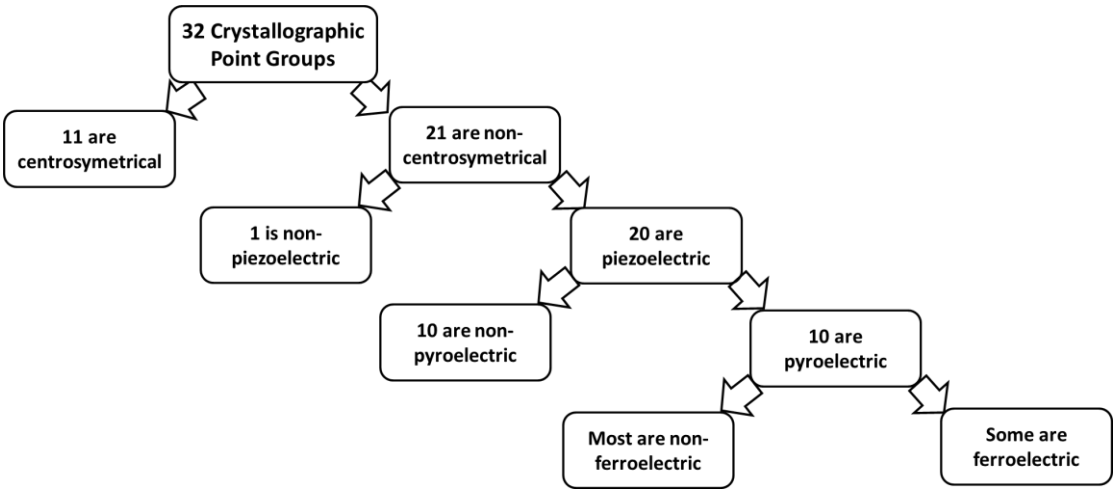

Fig. 2.1 Hierarchic classification of crystalline materials according to crystallographic point groups.

In the nature, there are 32 macroscopic symmetry types (point groups or crystal classes) and 11 of them possess a centre of symmetry (Fig. 2.1). Of the 21 non-centrosymmetric crystal classes, all except one produce an electric field when subjected to stress. The effect is linear, and it is called the piezoelectric effect. The reverse effect is always present: the crystal contracts or expands when subjected to an external field. Applying a mechanical stress or an electric field can polarize piezoelectric materials. Of the 20 piezoelectric crystal classes 10 are characterized by the fact that they have a unique polar axis. Crystals belonging to these classes are called polar because they possess spontaneous polarization or electric moment per unit volume. The spontaneous polarization

is in general temperature dependant and it can be detected by observing the flow of charge to and from the surfaces on change temperature. This is the pyroelectric effect and the 10 polar classes are often referred to as the pyroelectric classes. All ferroelectric materials are a subset of pyroelectric materials in which the direction of the spontaneous polarization can be changed between two or more orientation states by an applied electric field. The orientation states have the same crystal structure, but differ in the direction of the spontaneous polarization at zero applied electric field.

1.1.1. Miller indices

The orientation of a surface or a crystal plane may be defined by considering how the plane (or indeed any parallel plane) intersects the main crystallographic axes of the solid. The application of a set of rules leads to the assignment of the Miller indices (hkl); a set of numbers which quantify the intercepts and thus may be used to uniquely identify the plane or surface.

Also, tere are also several related notations [B.2]:

- the notation {hkℓ} denotes the set of all planes that are equivalent to (hkℓ) by the symmetry of the lattice.

In the context of crystal directions (not planes), the corresponding notations are:

- [hkℓ], with square instead of round brackets, denotes a direction in the basis of the direct lattice vectors instead of the reciprocal lattice.
- The notation <hkℓ> denotes the set of all directions that are equivalent to [hkℓ] by symmetry.

2.2. Ferroelectric crystals

1.2.1. General properties of ferroelectrics

A ferroelectric crystal is defined as a crystal which exhibits spontaneous electric dipole moment. In the ferroelectric state the centre of positive charge of the crystal does not coincide with a centre of negative charge. The plot of

polarizations versus electric field for the ferroelectric state shows a hysteresis loop (see Fig. 2.2).

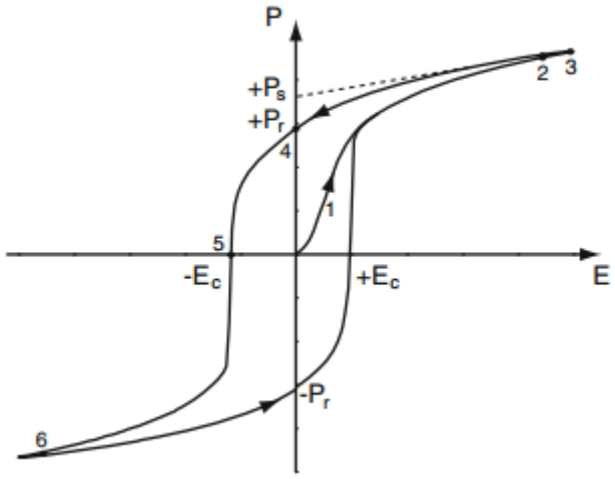

Fig. 2.2 Ideal hysteretic behaviour of the ferroelectric polarization in an applied electric field, considered at a macroscopic scale, adapted from [B.3].

Starting at the origin ($P = 0$, $E = 0$, possible macroscopically if the sample has multiple domains compensating each other) and ramping up the field (1), to the total polarization gradually increases towards a saturation value (2) corresponding to all unit cells coherently oriented with the field. Further increasing the field, the polarization is still increasing by dielectric charging (3). When the field is decreased back to zero, the total polarization decreases a little but remains finite, and the polarization value reached at $E = 0$ is called the remanent polarization $+P_r$. When the field is increased in the opposite direction, the polarization state switches suddenly for a specific field intensity called the coercive field $-E_c$. Upon further increase, the polarization saturates and a simple dielectric response is reached again (6). Generally, the same behaviour is observed when the electric field is reversed, and repeated cycling results in a symmetric hysteresis loop, with switching events at $\pm E_c$. In the presence of internal fields, e.g. due to charge accumulation in a ferroelectric transistor, the hysteresis loop may however be offset with respect to $E = 0$, a phenomenon known as imprint. The spontaneous polarization $\pm P_s$ is usually defined as the extrapolation at zero field of the polarization value at

high fields, where the slight decrease is due to charging. Ideally, P_r and P_s should be identical. In reality, P_s is often higher in polycrystalline materials (due for instance to the formation of opposite domains during the ramping of the field to zero), but can be very close in single crystals [B.4]. At high temperatures, most ferroelectric materials exist in a paraelectric, generally centrosymmetric phase, and exhibit a simple dielectric response to applied electric fields. As they are cooled down below a critical temperature, called the Curie temperature T_c, they undergo a structural phase transition to a lower crystal symmetry phase, which allows the appearance of the spontaneous polarization.

The ferroelectric crystals may be classified into two main groups: displacive and order – disorder. For the displacive ferroelectrics, below the phase transition a spontaneous polarization appears due a concerted displacement of ions in one or more sub-lattices. For the order – disorder ferroelectrics, below the phase transition a spontaneous polarization appears due an orientation of dipoles in one direction.

There is an important distinction between displacive and order – disorder systems in respect to the lowest frequency ("soft") optical phonon mode dynamics. If the soft mode can propagate in the crystal at the transition, then the transition is displacive. If the soft mode is only diffusive (non-propagating) there is really not a phonon at all, but only a large amplitude hopping motion between the wells of the ordered – disordered systems.

2.2.2. Domains and domain wall relaxation

Ferroelectric materials are characterized by a finite electric polarization in absence of an external electric field. Furthermore, this polarization must contain at least two stable states, and must have the ability to be reversibly switched from one state to another after applying an electric field. Thus, regions with different orientations of the polarization vector may coexist within a ferroelectric sample, and are called ferroelectric domains. In other words, domains are continuous areas of the materials which have uniform

polarization. Historically, domains and their structure were first investigated in ferromagnetic materials and only later obtained results had been applied to ferroelectric domains. Therefore, Kittel first of all described a few possible domain configurations in ferromagnetic thin films [B.5] which are presented in Figure 2.3.

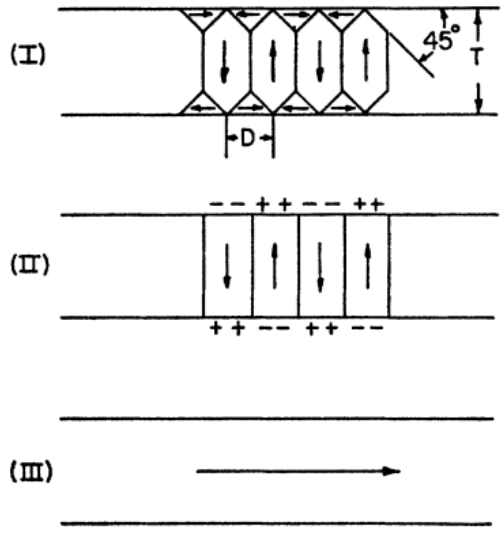

Fig. 2.3 Domain configuration in freestanding films and slabs.

Here, possible states were considered for the magnetization, corresponding to an out-of-plane polydomain structure, with (I) or without (II) flux-closure magnetization rotation (so-called Landau-Lifshitz domains[1]) near the film top and bottom surfaces, or a purely monodomain in-plane magnetization (III). In ferromagnetic materials, where the magnetization is related to the ordering of microscopic spins and no monopoles exist, the type of domain structure is defined by the energy balance between the energy cost of divergent or unclosed field lines originating from the magnetic structure, and the energy cost of the domain wall. For a periodic, out-of-plane domain structure, the balance between these two terms will determine the period width, obeying the Landau-Lifshitz-Kittel scaling relation (see Eq. 2.1):

[1] Landau-Lifshitz domain is a type of magnetic domains in which ferromagnetic material tend to split in order to reduce internal energy. This energy can be described by Landau-Lifshitz energy equation [B.6].

$$D = \sqrt{\frac{\sigma}{U}d}, \tag{2.1}$$

where: D is the period of the domain structure, d the thickness of the film, U is domain energy density per unit volume, σ is domain wall energy density per unit area. In ferroelectric materials this relation was found to be valid over a wide range of thicknesses, providing the polarization is unscreened or only weekly screened [B.7]. However, the fundamentally different physical origins of ferromagnetism and ferroelectrics still lead to significant differences between domain structures in these two types of materials. As shown by studies of domain periodicity in various ferroic materials at comparable film thicknesses significantly narrower domains are encountered in ferroelectric with respect to ferromagnetic thin films [B.8]. Moreover, the structural nature of the interface between two domains, referred to as domain wall, differs also significantly between ferromagnetic and ferroelectric materials and more detailed explanation will be presented further.

In ferromagnets, the typical energy of a domain wall is primarily governed by exchange, which favours parallel alignment of the spins, and magnetic domain walls. In switching by 180°, the magnetization vector either rotates in a plane parallel to the domain wall Bloch or normal to the domain wall Neel. These rotations typically take place over many microns, a length scale that is a consequence of the ability of spins to overcome the weak spontaneous magnetostriction that couples lattice strain and magnetization. In ferroelectrics, the domain wall energy is rather dominated by the very strong coupling between the polarization and the strain, and polarization reversal therefore occurs on a much shorter scale of a few unit cells. Thus a 180° ferroelectric wall is predominantly Ising-type, i.e. with no in-plane component associated with polarization rotation. Different types of magnetic walls are presented in Fig 2.4.

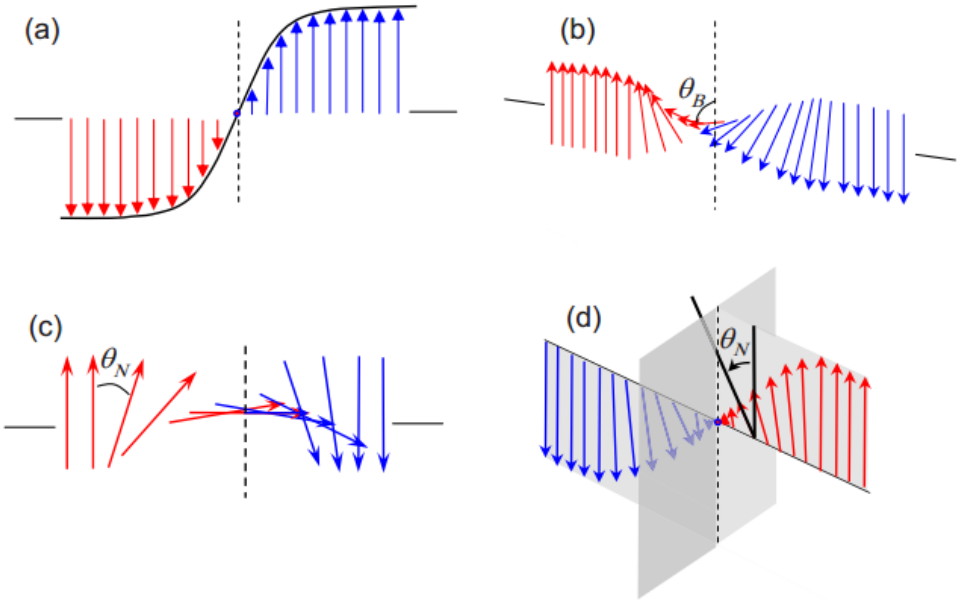

Fig. 2.4 Different types of domain walls: a) Ising type, b) Bloch type, c) Neel type, and d) Mixed Ising-Néel type walls. A mixed Ising-Bloch type would look similar to (d) except that the rotation B would be out of the plane of the polarization vector, adapted from [B.9].

Lee et al. [B.9] showed that using density functional theory, and molecular dynamics simulations, the 180° domain walls in prototypical ferroelectrics lead titanate ($PbTiO_3$) and lithium niobate ($LiNbO_3$) are showed to have mixed character; predominantly Ising-like domain walls also manifest some Bloch- and Neel-like character. Also, using the example of classic ferroelectric $BaTiO_3$, and by incorporating the flexoelectric effect into a phase-field model, *Gu et al.* [B.10] demonstrated that the flexoelectric effect arising from stress inhomogeneity around the domain wall leads to the additional Bloch and Neel polarization components in Ising type domain walls. In the cases described above the evidence of ferroelectric domain walls are presented only from the theoretical point of view. Meanwhile, *Wei et al.* [B.11] proposed theoretical and direct experimental evidence for the existence of Neel-like domain walls in ferroelectric materials. The dynamics of ferroelectric domain walls becomes extremely interesting and should be discussed further.

However, domain patterns are highly periodic only in the static limit. In case of alternating small electric field the domains would respond to it by changing size. The domain containing more energy would grow at the expense of less favourable ones. This is very often considered as movement of domain walls, as it is the same from mathematical point of view. One of the first observations of ferroelectric domain wall motions was done by Walter J. Merz at 1954 in barium titanate single crystals [B.12]. Three types of domain walls were distinguished from optical observations.

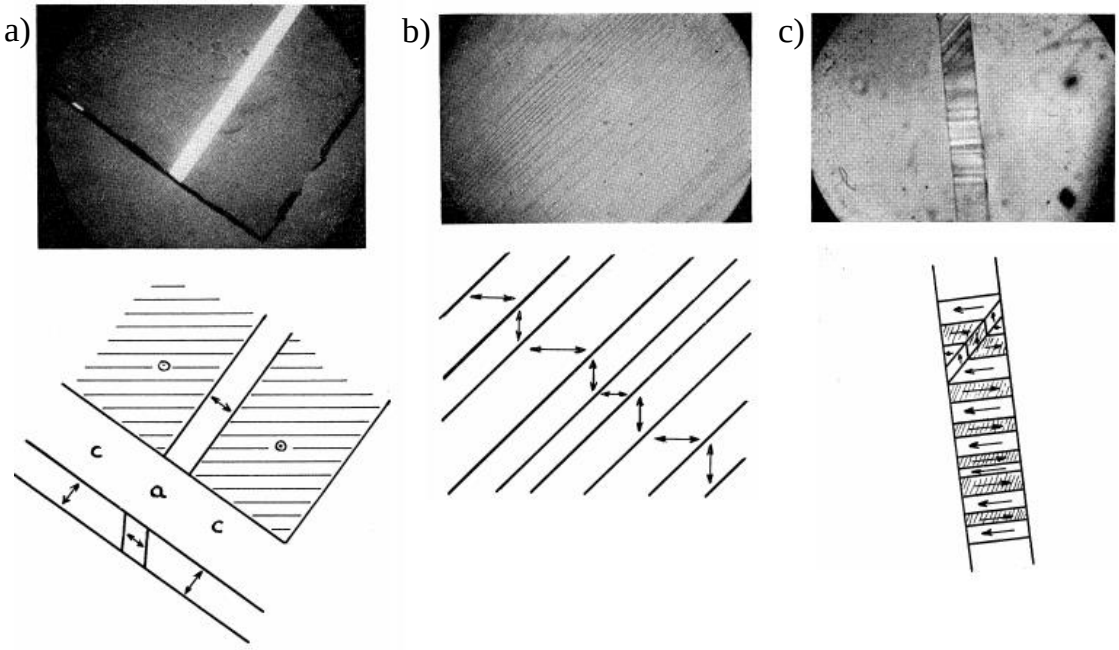

Fig. 2.5 Photo and schematic sketch of three different types of domain walls observed in $BaTiO_3$ single crystals by Walter J. Merz at 1954: a) 90º walls between an a domain and two c domains, b) 90º walls between a domains and c) 180º walls (antiparallel domains) at the edge of the crystal [B.12].

The first one is the boundary between a domain in which all the dipoles are aligned perpendicular to the crystal plate under investigation (*c* domain) and a domain in which all the dipoles are aligned in a direction parallel to the crystal plate surface (*a* domain). This type of boundary was called a 90º wall because the two domains are polarized at 90º to each other. In the second case, the boundary is also a 90º wall, but the polarization on both sides of the wall lies parallel to the major surfaces of the crystal plate (*a* domains). The third type of

boundary is the 180º wall that is a boundary between domains with antiparallel polarization. In all these examples, domains arrange themselves in such a way that no surface charges are built up on the 90º walls: head-to-tail zig-zag arrangement. Domain wall movement and alignment can be induced after applying electric field to the crystal and this property was investigated by Walter J. Merz at 1952 [B.13]. The behaviour has been studied both in so-called *a* plates, where the polar axis lies in the plane of the plate, and in *c* plates, where it is perpendicular. Here, the schematic illustration of domain wall movement is proposed (see Fig. 2.6).

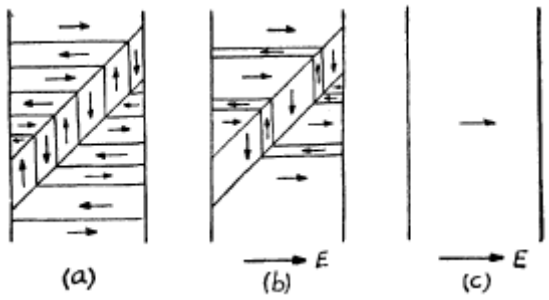

Fig. 2.6 Schematic arrangements of when a field is applied. Observe the head-to-tail arrangement, adapted from [B.13].

If electric field is applied in the direction as it is shown in Fig 2.6 b), the whole zig-zag line is moved and domain increases. Further increasing electric field, material becomes monodomain, as is shown in Fig 2.6 c). Such movement of domain walls changes net polarization of the crystal in response to external electric field and this change can be associated with dielectric permittivity. It means that domain walls may give additional contribution to the total dielectric permittivity of the material. The contribution might be quite big (see references [B.14, B.15]) and sometimes exceeding other contributions by orders of magnitude [B.16, B.17]. One of the best examples of domain walls contribution to the total dielectric permittivity was presented by Wang at ell [B.17], where contribution was observed in $BaTiO_3$ single crystal (see Fig. 2.7).

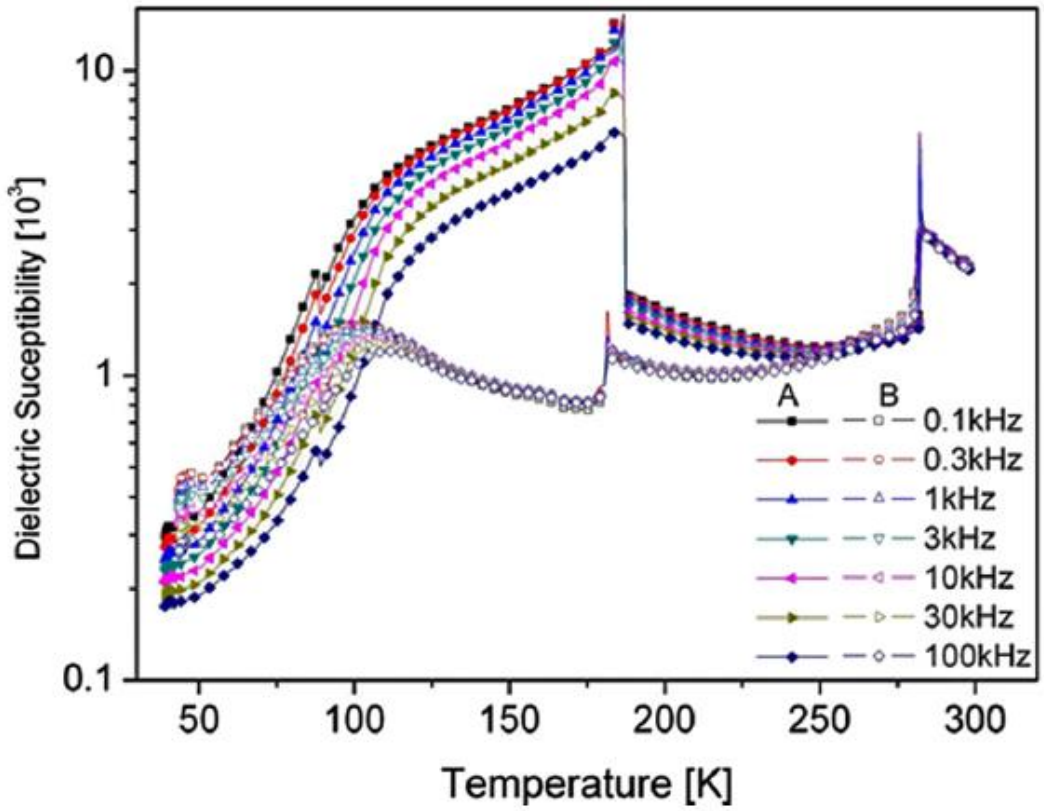

Fig. 2.7 Temperature dependency of dielectric permittivity of <111> oriented $BaTiO_3$ single crystals under 2 V amplitude on cooling.
Sample A: Solid marks, depoled at room temperature before measurement; sample B: open marks, annealed at 450 ºC for 10 h before measurement, adapted from [B.17].

Here, notable differences, both in magnitude and in frequency dependence of the dielectric permittivity, are found already in the orthorhombic phase when approaching the O/R transition temperature (around 180 K), e.g., the dielectric susceptibility of sample A at 200 K and 100 Hz is around 30% higher than that of sample B. More detailed explanation ad discussion can be found in [B.17].

However, domain walls contribution to the total dielectric permittivity is associated with a huge amount of atoms and it is relatively slow. Contributions of ions usually have their characteristic frequencies in THz or far infrared range. In the case of domains, characteristic frequencies lies in radio- and microwave range.

As it was described above, ferroelectric materials consist of domains that are spontaneously polarized in one of the symmetry-permitted directions of the material. Each two adjacent domains are separated by compositionally homogeneous interface. These interfaces usually meet the condition of electrostatic compatibility, i.e. the normal component of the spontaneous polarization is continuous across the interface [B.18]. They carry no net bound charge and are hence called neutral domain walls (NDW). Alternatively, charged domain walls (CDW) may exist, which carry bound charge due to a jump of this polarization component at the wall, breaking the condition of electrostatic compatibility. Figure 2.8 illustrates simple examples of 180° NDW (Fig. 2.8 a)) and CDWs (Fig. 2.8 b) – d)) between domains with antiparallel polarization orientation.

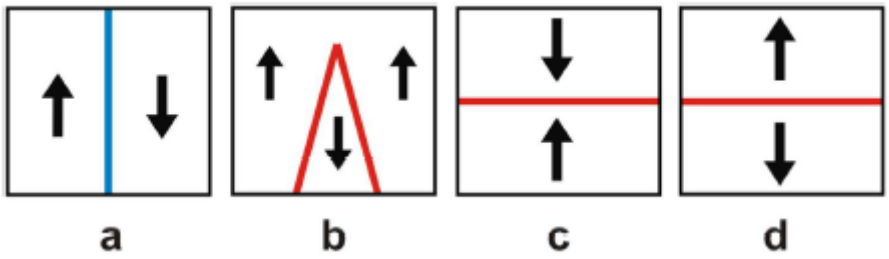

Fig. 2.8 Schematic illustration of neutral and charged 180° domain walls. a) Neutral domain wall. b) Domain configuration containing domain walls that are partly charged. The head-to head configuration of charge domain wall c). Charge domain wall, where tail-to-tail configuration is presented b) and d), adapted from [B.19].

Here, NDW fully satisfies the condition of electrostatic compatibility, i.e. the normal component of the spontaneous polarization (indicated with arrows) is continuous across the wall. Domain configuration containing domain walls that are partly charged due to their slight inclination with respect to the polarization direction is presented in Fig. 2.8 b). Figure 2.8 c) – d) presents a schematic illustration of charged domain walls, where the condition of electrostatic compatibility is strongly broken, i.e. the jump of the normal component of the spontaneous polarization comparable to the polarization itself. The head-to

head (H-H) configuration (2.8 c)) carries positive bound charge and the tail-to-tail (T-T) configuration (2.8 b), d)) negative bound charge. Recently, the scientific field of charged domain walls in ferroelectrics are breaking topic due to their potential use in nanoelectronic devices. For this reason, the physics of charged domain walls has to be discussed more in details. Classification of CDW and requirements for formation of CDW will be presented in the next paragraphs.

Talking about charged domain walls, we should also talk about depolarizing field, which is determined by appearance of the bound charge at the CDWs. The bound charge ρ_b at CDWs produces an electric field, which interferes CDW formation with increased electrostatic energy. However, the main disturbance comes from the fact that the field always has a depolarizing effect on the adjacent domains as it is always directed (at least partly) against the polarization. There is a way how to reduce the depolarization field below the critical limit: the bound charges need to be compensated either by mobile defects or free electrons or holes. Therefore, CDWs can be divided into two types: (1) weakly charged domain walls (wCDW) when the depolarization field created by the bound charge is not large enough to destabilise ferroelectricity in the adjacent domains and (2) strongly charged walls (sCDW) corresponding to the case where the bound charge at the CDW is enough to create a depolarization field which destabilises ferroelectricity in the adjacent domains. The division into wCDW and sCDW was made taking into account of the absence of screening charges. *Bednyakov et al.* [B.19] showed that in a $BaTiO_3$-type material strongly charged domain walls cannot exist without screening of the bound charge with free charge carriers. The depolarization electric field created only by the bound charges at the H-H sCDW is shown in Fig. 2.9 a).

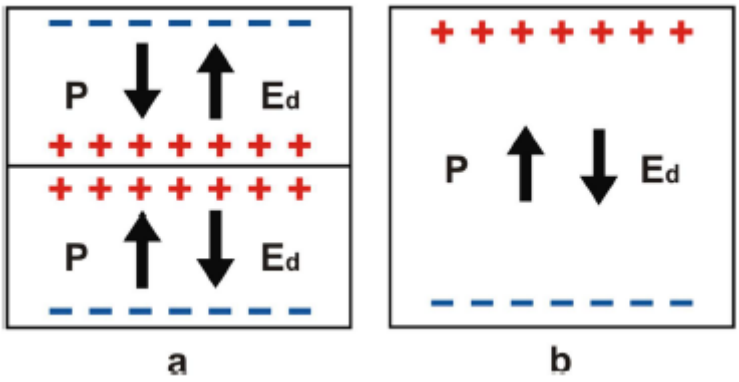

Fig. 2.9 The creation of depolarization field. a) sample with a head-to-head charged domain wall. b) single domain ferroelectric plate, adapted from [B.19].

Also, it was seen that depolarization field of the same size appears in a ferroelectric single-domain plate with a normal orientation of the polarization, when the absence of free charge carriers are taken into account (see Fig. 2.9 b)). Thus, the problem of a destabilisation of ferroelectricity in a sample with sCDW is quantitatively identical to the one of a ferroelectric plate where it was seen that such a depolarization field leads to a drop of the Curie temperature by a term expressed in Eq. 2.2 [B.18].

$$\Delta T_0 = C\frac{\varepsilon_0}{\varepsilon_b}, \tag{2.2}$$

here: C is the Curie-Weiss constant and ε_0 is the dielectric permittivity of vacuum. According to Eq. (2.2), in $BaTiO_3$ (with $C = 1.7 \cdot 10^5$ K and $\varepsilon_b/\varepsilon_0 = 7$) [B.20], Curie temperature would be shifted by ΔT_0 = 24000 K. Such shifts of Curie temperature are physically impossible. Hence, such sCDW cannot exist with absence of free carrier charges. In order to have sCDW, free charge screening is required. Exists two types of screenings: external and internal screening. External screening is fundamentally impossible, because of the fact that positive bound charge is located inside the insulating material (Fig. 2.9). Thus, the existence of sCDW requires internal screening, i.e. screening by free charges from the bulk of the material. There are several ways, how internal screening can be performed and these ways will be presented further.

The occurrence of strongly charged domain wall is very sensitive to the details of the screening mechanism. Bipolar electron-hole screening, unipolar screening, screening with photon generated carriers, mixed electron/ion screening and screening of sCDW with charge provided from external source are one of the possible screening mechanism, but only bipolar electron-hole and mixed electron/ion screenings are the main once. In the case of bipolar electron-hole screening in typical perovskite ferroelectrics, the main source of compensating free carriers is electron transfer from the valence to the conduction band over the bandgap of the ferroelectric. Thus, according to the work provided by *Gureev et al*. [B.21], the formation energy of a single wall in a sample can be evaluated using the following equation:

$$W_{CDW} \approx \frac{2P_s E_g}{e}, \tag{2.3}$$

where: E_g is the bandgap, P_s is the spontaneous polarization and e is the elementary electron charge.

For a bandgap of about 3eV, which is typical for perovskites, the formation energy of sCDWs are some two-order of magnitude larger than the energy of neutral DWs (W_{NDW}):

$$W_{CDW} \cong 10^2 W_{NDW}. \tag{2.4}$$

Meanwhile, in the case of mixed electron/ion screening, screening of sCDW through the collection of free equilibrium carriers from adjacent domains leads to very high sCDW formation energy due to the space charge of the ionised impurities in the bulk of the crystal. However, this energy is basically reduced if the ionised impurities are mobile, i.e. if they can be redistributed during the formation of the sCDW. If the total amount of charge in the crystal is large enough to neutralise the bound charge at the walls, such a screening mechanism is energetically more favourable than the pure electron-hole screening, because no energy is lost during the electron transfer across the bandgap. Therefore, the sCDW formation energy can be evaluated as following [B.21]:

$$W_{mix} \cong \frac{t_{CDW}}{t_{CDW}} W_{NDW}, \tag{2.5}$$

here: t_{CDW} is the half-width of the sCDW, t_{NDW}, is the half-width of the NDW.

For typical perovskite ferroelectrics, t_{CDW} is expected to be one order of magnitude larger than t_{NDW}. Comparing Eq. 2.4 with Eq. 2.5 it was seen that in perovskite ferroelectrics, strongly charged domain walls formation with a mixed electron-ion screening mechanism is more favourable energetically than in the case of bipolar electron-hole screening. Experimental data proved that in bulk crystals of $BaTiO_3$, the mixed screening mechanism is dominant [B.22]. A possible way to create strongly CDWs is so called frustrative polling method [B.19, B.22]. This method is based on the crystal cooling through its ferroelectric phase transition with a dc field applied along a direction different from the allowed spontaneous polarization direction. One of the first roles of the frustrative field is a reduction of the number of preferable polarization states in the sample, which increases the probability of the appearance of 90-degree strongly CDWs. Another role is that frustrative field reduces the polarization component perpendicular to the sCDW. Hence, the amount of bound charge at the wall is smaller and accordingly the amount of mobile carriers needed for screening is smaller too. One of the nicest examples of the creation of charged domain walls in tetragonal $BaTiO_3$ using frustrative field method was presented by *Sluka et al.* [B.22] and can be seen in the following figure.

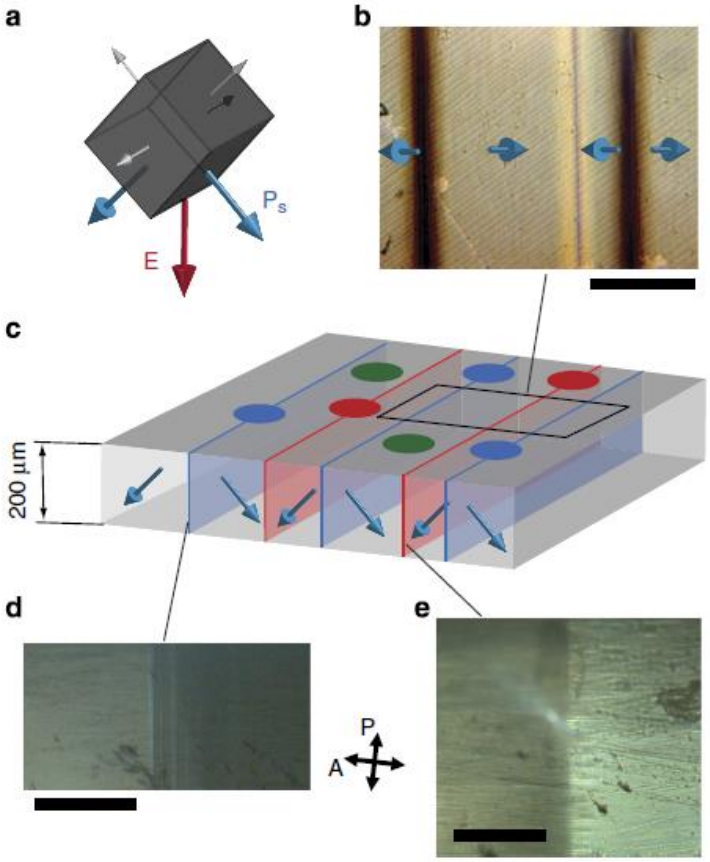

Fig. 2.10 Charged domain walls in tetragonal $BaTiO_3$. a) Crystal poling in a $[110]_c$-like direction (red arrow) allowing two equally preferred ferroelectric domain states (blue arrows). When the frustrated poling is applied during a slow paraelectric-ferroelectric phase transition, tail-to-tail b) - d) and head-to-head b), c), e) domain walls are formed. The picture is adapted from [B.22].

Here in the Fig. 2.10 a) is shown that poling of a crystal in a $[110]_c$-like direction (red arrow) allowing two equally preferred ferroelectric domain states (blue arrows) out of the six permitted (blue and grey arrows). When the frustrated poling is applied during a slow paraelectric-ferroelectric phase transition, tail-to-tail b) - d) and head-to-head b), c), e) domain walls are formed. *Sluka et al*. observed that conduction between electrodes connected by tail-to-tail sCDW was almost identical to the conduction through the bulk. Meanwhile, the conduction between electrodes touching head-to-head sCDW was reproducibly and steadily (for > 120 h) 10^4–10^6 times higher.

Another way to create stable and easy controlled charged domain walls in ferroelectric thin films is a polarization switching using either a conductive probe or patterned top electrodes. This method was presented by *Feigl et al.* [B.23]. The epitaxial (110) oriented (Pb,Sr)TiO_3 (PST in short) thin film for the demonstration of the concept was used. Like in the case of BTO single crystal [B.22], applying an electric field along [110] of the tetragonal PST thin film is required in order to create CDW. First of all, *Feigl et al.* demonstrated the creation of CDWs in (110) oriented tetragonal ferroelectric PST thin film during 180º polarization switching by using piezoresponse force microscopy (PFM). It was seen that so called "secondary domain" is created resulting the creation of CDW. The existence of "secondary domain" and CDW is presented in Fig. 2.11.

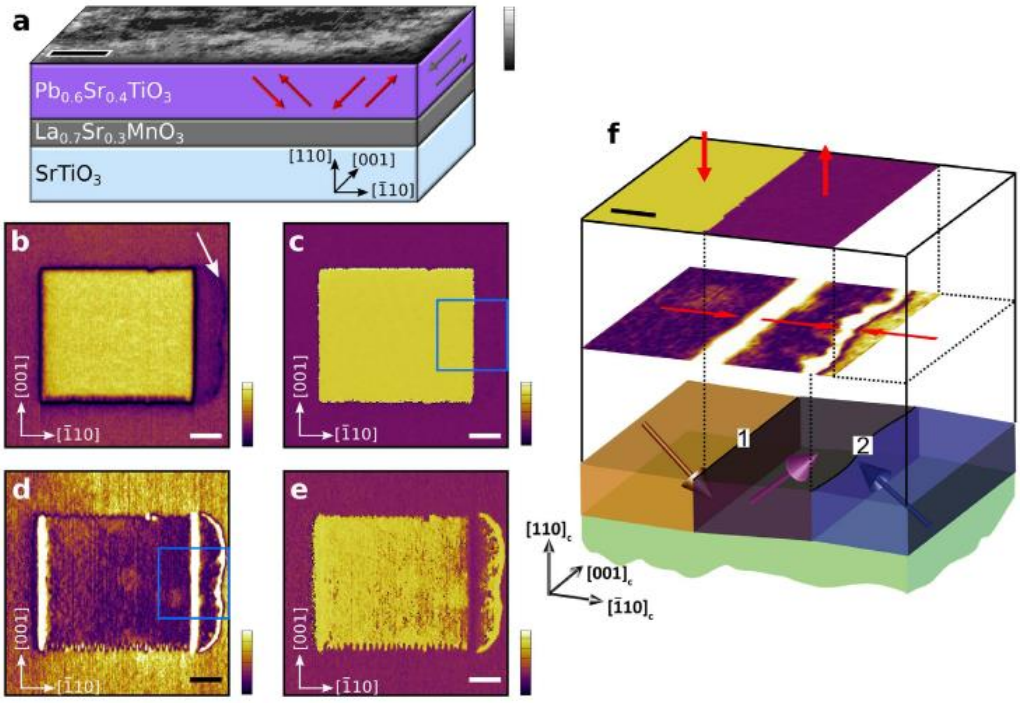

Fig. 2.11 a) AFM topography image of PST top layer together with a schematic of the PST/LSMO//STO (110) multilayer. Vertical PFM b) amplitude and c) phase images after switching a 2.5 × 2.5 µm2 region downwards. The corresponding lateral PFM d) amplitude and e) phase images. f) Close-ups of the PFM signal from the regions marked by the blue squares, adapted from [B.23].

Here, from both vertical and lateral PFM images additional contrast is visible (Fig. 2.11 b), d), e)). The neutral 90˚ domain wall is created between primary and secondary domain (1 in Fig. 2.11 f)) and also head-to-head CDW between the outer boundary of the secondary domain and the as-grown domain (2 in Fig. 2.11 f)). In order not to depend on the PFM tip for the creation of the CDW electrodes can be deposited on the thin film. The polarization switching can be performed by a train of pulses, which successfully creates and moves CDW (see Ref [B.23]). Of course, exist more ways how CDW can be created. In order to get deeper understanding Ref. [B.24] should be checked.

2.4. Ferroelectric relaxors

Ferroelectric relaxors (also known as "relaxor ferroelectrics" or simply "relaxors" for short) are the class of disordered crystalline (or polycrystalline) materials having extraordinary properties like very broad dielectric relaxation dispersion, very high dielectric permittivity, high piezoelectric properties. Relaxors found many applications in electronics such as multilayer ceramic capacitors, electro-optical devises or medical imaging devices [B.25].

At high temperatures relaxors are in non-polar paraelectric phase (PE), which is similar to the paraelectric phase of normal ferroelectrics. During cooling they transform into ergodic relaxor (ER) state in which appears nanometric size polar nanoregions (PNRs) with randomly distributed directions of dipole moments. This transformation which occurs at the so-called Burns temperature (T_B) [B.26] cannot be considered as a structural phase transition because there is no change of crystal structure (symmetry) at the macroscopic and mesoscopic scales. Nevertheless, the polar nanoregions affect crystal properties and for this reason the state below T_B is considered as a new one, different from paraelectric one. At temperatures close to Burns temperature the polar nanoregions are mobile and their behaviour is ergodic [B.27]. On cooling down further their dynamics slows down and at low temperatures T_f (typically hundreds degrees below T_B) PNR becomes frozen or at least their dynamic critically slow down. Relaxors enters nonergodic (NR) state but macroscopic

average structure remains centrosymmetric cubic. Similar behaviour appears in another disordered phase called dipole glass or spin glass phase. The transition to nonergodic phase is manifested in the dielectric constant with characteristic very broad dispersions. Permittivity maximum is the same order of magnitude as in the normal ferroelectric perovskites, but its maximum is diffused and shifts to higher temperatures on measurement frequency increase as it is shown in Fig. 2.12 a).

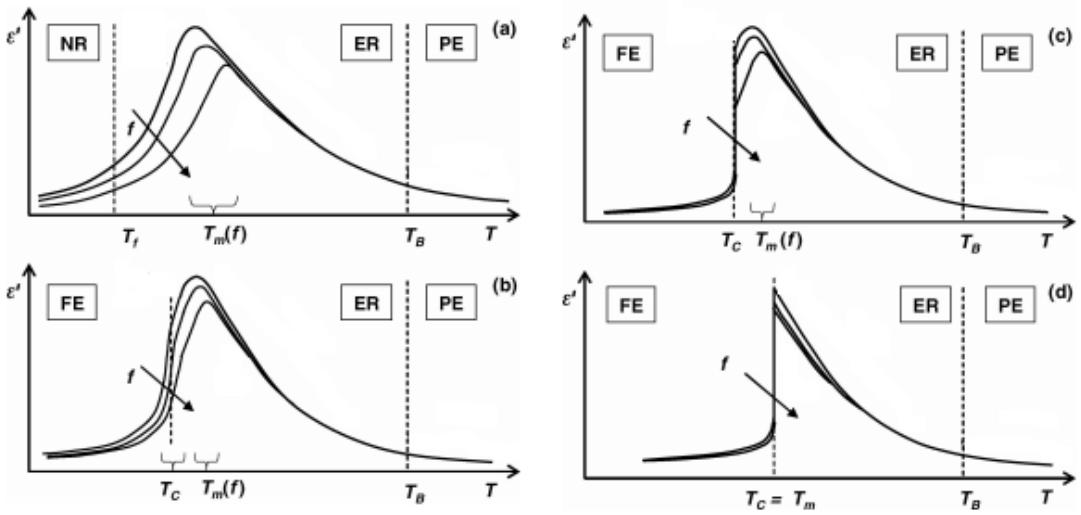

Fig. 2.12 Different possibilities for the temperature evolution of structure and dielectric properties in disordered ferroelectric relaxors, adapted from [B.27].

The nonergodic phase can be transferred to ferroelectric (FE) phase by strong enough external electric field. This feature distinguished relaxors from dipolar glasses. In many relaxors transformation to ferroelectric phase occurs spontaneously at T_C, hence nonergodic phase does not exist at all (Fig. 2.12 b), c) and d)).

Compositional disordered, i.e. the disorder in the arrangement of different ions on the crystallographically equivalent sites, is a common feature of ferroelectric relaxors. The phenomenon was first observed in perovskites with disorder of non-isovalent ions, including the stoichiometric complex perovskite compounds, e.g. $Pb(Mg_{1/3}Nb_{2/3})O_3$ (PMN) [B.28], $Pb(Sc_{1/2}Ta_{1/2})O_3$ (PST) [B.29], $Pb(Sc_{1/2}Nb_{1/2})O_3$ (PSN), $Pb(Zn_{1/3}Nb_{2/3})O_3$ (PZN) or their solid solution with lead titanate – PMN-PT, PZN-PT.

The differences between ferroelectric relaxors and usual ferroelectric materials can be summarized as following:

The Vogel-Fulcher law (instead of Arrhenius relationship) is a common characteristic of ferroelectric relaxors and dipolar glasses for the characteristic relaxation time τ of the corresponding relaxation process:

$$\tau = \tau_0 exp\left(\frac{E_a}{k_B(T - T_{VF})}\right), \tag{2.6}$$

where: τ_0 represents attempt relaxation time, E_a – activation energy, k_B – Boltzmann constant and T_{VF} – freezing temperature.

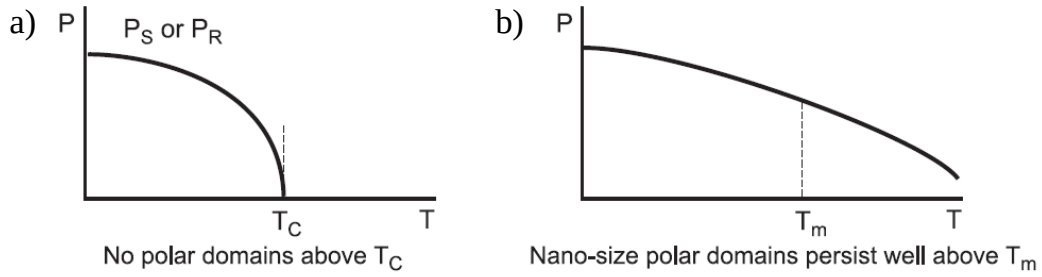

Fig. 2.13 Spontaneous polarization in normal ferroelectrics and relaxor ferroelectrics. Adapted from [B.30].

Polarization of a ferroelectrics decrease with increasing temperature and vanish at the phase transition temperature T_c (see Fig. 2.13 a)). No polar domains exist above T_c. By contrast, the field-induced polarization of a relaxor ferroelectrics decreases smoothly and there is no change of polarization neither at dynamic transition temperature T_m or phase transition temperature T_c.

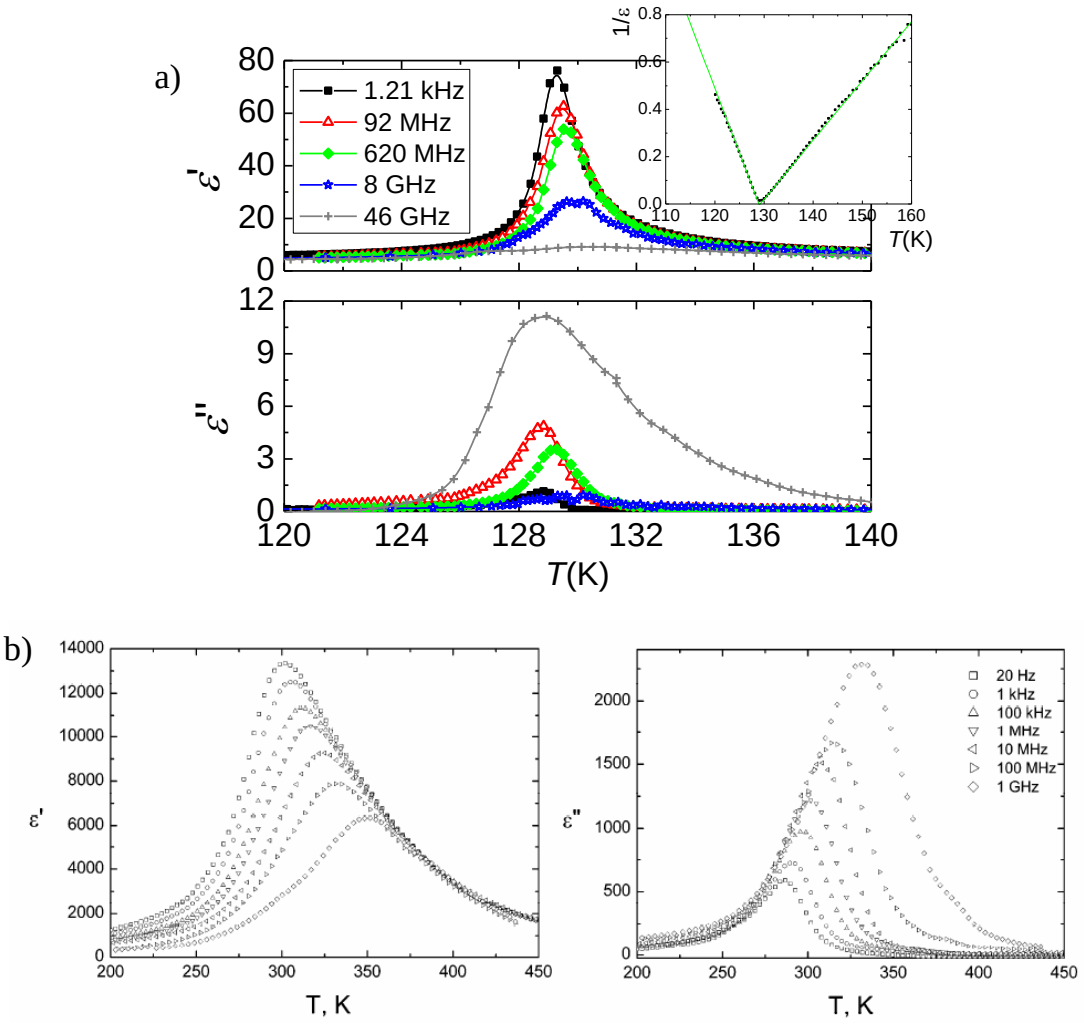

Fig. 2.14 The differences of dielectric permittivity in normal ferroelectrics and relaxor ferroelectrics. a) Temperature dependence of the complex dielectric permittivity of TSCC+3%Br crystal. The inset shows temperature dependence of the reciprocal dielectric permittivity [B.33]. b) Temperature dependences of dielectric permittivity of disordered 0.5PMN-0.5PSN ceramic at different frequencies [B.34].

Static dielectric permittivity at the ferroelectric phase transitions T_C demonstrate sharp and relatively narrow peak (Fig. 2.14 a)). Meanwhile, ferroelectric relaxors exhibits very broad dielectric permittivity peak maximum with strong frequency dispersion (Fig. 2.14 b)). Dielectric permittivity in ferroelectrics obeys Curie-Weiss law above and below phase transition

temperature, while in ferroelectric relaxors strongly deviates from Curie-Weiss behaviour and coincides just above T_B. More detailed information regarding theory of ferroelectric relaxors and differences between ferroelectrics and ferroelectric relaxors can be found here [B.30-B.34].

2.5. Ferroelectric thin films

Ferroelectrics are relevant components in a wide spectrum of applications. In thin film form, ferroelectrics have now been used for several years in radiofrequency devices and in non-volatile memories. Components based on ferroelectric films are also being developed for various sensor and actuator applications and for tunable microwave circuits. The development of ferroelectric thin films started at the late 1960s and early 1970s when progress in integrated Si devices and thin film processing techniques triggered interest in the use of ferroelectric thin films for fabrication of non-volatile memories. Therefore, films might be divided into thin and thick films with thickness equal from 4 to 100 nm (10 to 250 unit cells) in the case of thin films and with thickness equal and more than 100 nm in the case of thick films. It is crucial to describe fundamental properties of thin films and this topic will be touched in the following paragraphs.

Ferroelectrics are used in many shapes and sizes. One of the main advantages to use ferroelectric thin films is that a certain misfit between substrate crystal lattice and film crystal lattice is likely to exist when a thin film is deposited on a substrate and the presenting misfit causes relevant fundamental properties. Substrate and film lattices mismatch is known misfit strain and it is expressed as:

$$e_m(T) = \frac{a_S(T) - a_f(T)}{a_f(T)}, \tag{2.7}$$

where: $e_m(T)$ – misfit strain, $a_S(T)$ and $a_f(T)$ is temperature dependant substrate and film lattice parameters, respectively.

In general, two types of misfit strain exist: epitaxial compressive strain and epitaxial tensile strain which is presented in Fig. 2.15.

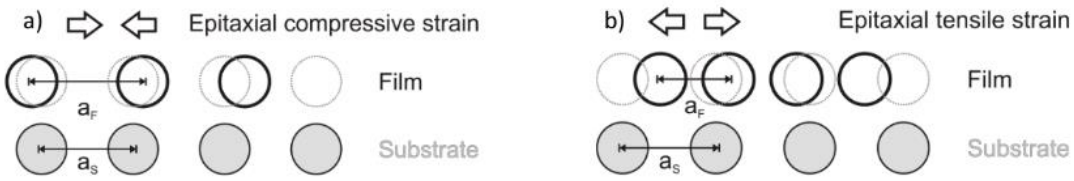

Fig. 2.15 Schematic illustration of epitaxial compressive and tensile strain.

Here, grey and white circles represent atoms in the substrate and film lattices, correspondingly. Due to the limited thickness of the thin film compared to the substrate, the film will tend to strain to fit the substrate. In the case of epitaxial compressive strain (see Fig. 2.15 a)), substrate lattice parameter is smaller than in the case of film lattice ($a_S < a_f$). Hence, film lattice has to shrink with respect to substrate lattice, causing a film strain, which will have a negative misfit strain value (Eq. 2.7). Meanwhile, in the case of epitaxial tensile strain (Fig. 2.15 b)), substrate lattice parameter is greater than in the case of film lattice ($a_S > a_f$). This causes dilation of film lattice with respect to substrate lattice and misfit strain value (Eq. 2.7) will be positive. The method of using a crystal misfit to achieve strain in a thin film and modify its properties is often called "strain engineering". From the strain engineering point of view, substrate and film lattice mismatch is very important topic, because of the possibility to control film properties. This interest in strain engineering has led to the development of high-quality perovskite substrates with a wide range of lattice parameters (3.68–4.17 Å) suitable for imposing various degrees of epitaxial strain (Fig. 2.16, bottom section). In order to use ferroelectric thin films in devices, bottom electrodes that are compatible with the epitaxy and allows for the retention of strain are required. In this regard, several conductive perovskite bottom electrode materials have been implemented (Fig. 2.16, middle section). The set of available single crystal substrates and conductive bottom electrodes provides an appropriate base upon which perovskite ferroelectric films (Fig. 2.16, top section) can be grown, controllably oriented,

strained and probed. Most theoretical and experimental studies of epitaxial strain control have focused on (001)-oriented ferroelectric films (due to the dominant of the pseudocubic (001)-cut of commercial substrates and relative ease of growth). Thus, I will also be focused on the such systems.

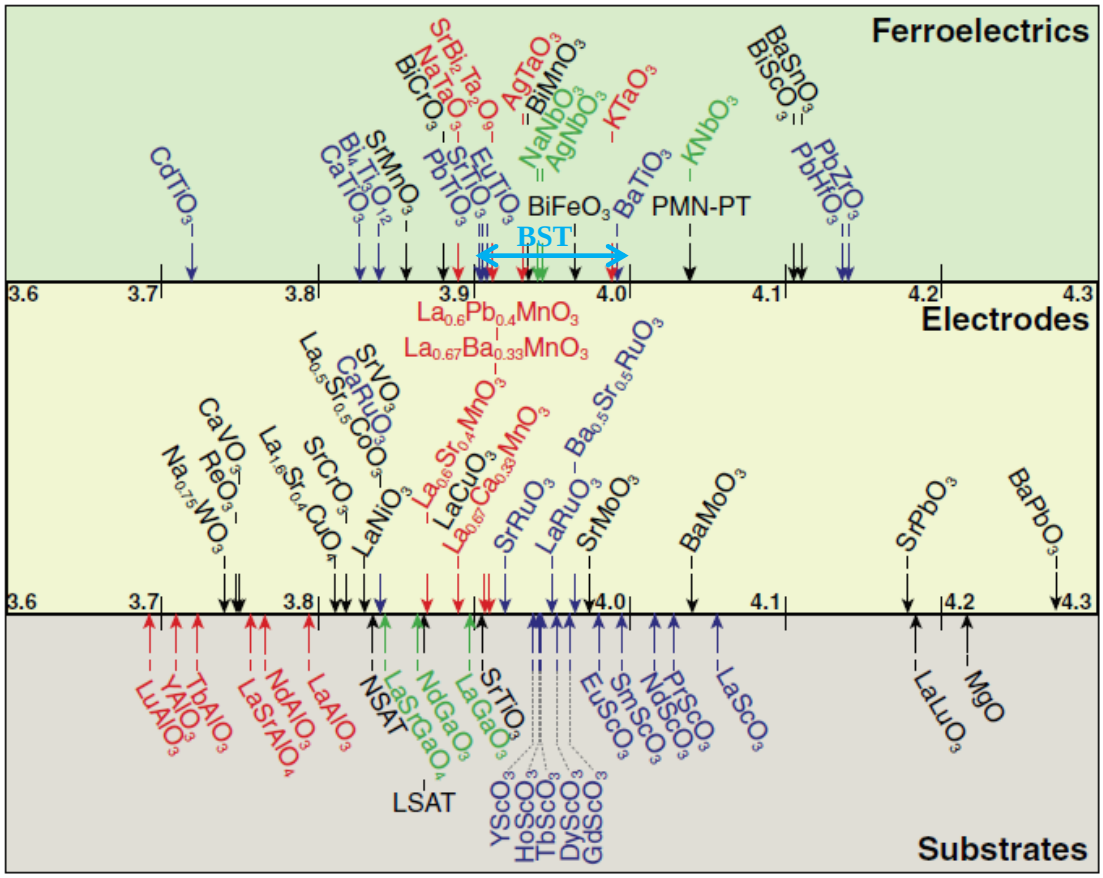

Fig. 2.16 Survey of lattice parameters of commercially available substrate materials (bottom section), a select list of perovskite electrode materials (middle section), and ferroelectric, incipient ferroelectric, and anti-ferroelectric materials (top section), adapted from [B.35].

As it was mentioned above, strain engineering is interesting because of the ability to control and modify thin film properties. The brief description of such properties will be presented in following sections.

One of the first developments of strain engineering was done by theoretical predictions for misfit strain-temperature phase diagrams in the late 1990s based on phenomenological thermodynamic models. Such phase diagrams predicted the ability of epitaxial strain to change the order of the

ferroelectric phase transitions, alter T_C. Different approximations and assumptions for the ferroelectric phases, for example, single-domain states [B.36] or two-dimensional two-domain states [B.37] in thermodynamic analysis, or full three-dimensional multidomain states [B.38] in phase-field simulations, have been used in theoretical investigations in order to understand equilibrium strain-phase diagrams of ferroelectric films.

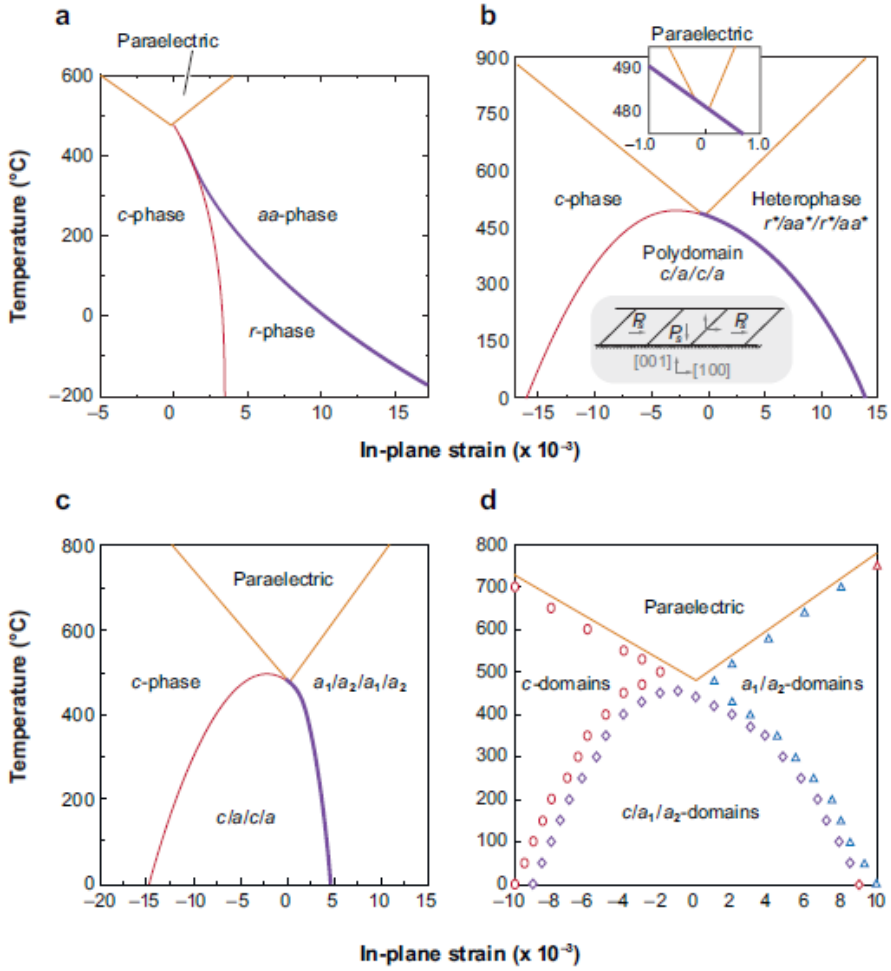

Fig. 2.17 Four strain-phase diagrams of (001)-oriented $PbTiO_3$ calculated using thermodynamic analysis or phase-field simulations and different assumptions of the ferroelectric domain states. a) Single domain for all ferroelectric states, adapted from [B.36]. b) Either single- or double-domain states with domain-wall orientations restricted to be 45º from the film/substrate interface, adapted from [B.37]. c) Single- or double-domain states with domain-wall orientations restricted to be either 45º or 90º from the film/substrate interface, adapted from [B.39]. d) Three-dimensional phase-field simulations, adapted from [B.38].

Figure 2.17 shows examples of strain phase diagrams for (001)-oriented PbTiO3 films from thermodynamic analysis and phase-field simulations, including clear differences for different approximations and assumptions about domain configurations. In order to experimentally realize these predictions, rare-earth scandate perovskite substrates were developed and used in order to demonstrate the power of strain-effects in controlling/inducing ferroelectricity [B.40]. By applying biaxial tensile strains of ~1% to (001)-oriented $SrTiO_3$ thin films grown on $DyScO_3$ substrates, researchers were able to induce room-temperature ferroelectricity (see Fig. 2.18 a)).

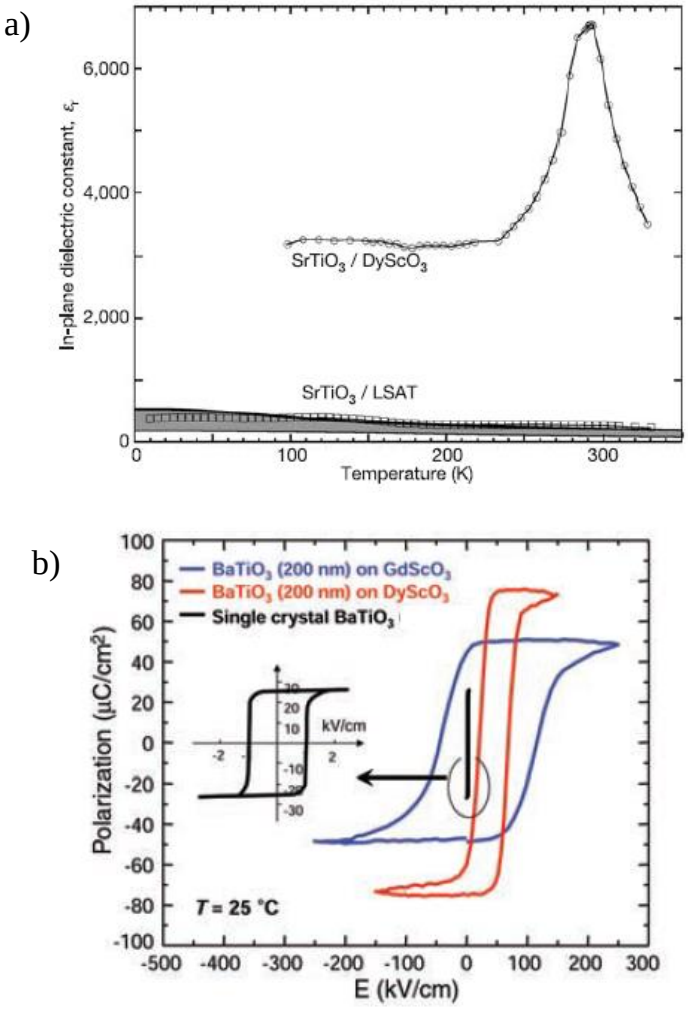

Fig. 2.18 a) In-plane dielectric constant (ε_r) in strained epitaxial $SrTiO_3$ films as a function of temperature, adapted from [B.40]. b) Polarization-electric field hysteresis loops of $BaTiO_3$ thin film capacitors, adapted from [B.41].

Also, application of a few percent compressive strain to $BaTiO_3$ resulted in the enhancement of the ferroelectric transition temperature by 500ºC and remnant polarization by ~250% [B.41]. In general, these studies revealed how theoretical and experimental works can be used to manipulate the electrical and elastic boundary conditions in epitaxial thin films. Using these tools, researchers can deterministically combine phase transition temperatures and phase competition, implement metastable phases, and much more – all of which can dramatically impact ferroelectric susceptibilities and enable the creation of new ferroelectric functionalities. Such work provides the fundamental tools to strain-engineer ferroelectric thin films. There are plenty works which show how strain can tune ferroelastic domain structures which can dramatically influence ferroelectric susceptibility and functionality. *Wada et al.* [B.42] showed that for [111] poled barium titanate single crystals, piezoelectric properties increase with decreasing domain size. Using the 2-phases model, it was revealed that the piezoelectric properties from the 90º domain wall region exhibited ultrahigh piezoelectric property. As the results, the domain size of 3 μm was successfully induced, and the d_{31} was obtained at – 243,2 pC/N. More examples of such phenomena will be presented in another chapter, where the state of art of barium strontium titanate and lead magnesium niobate-lead titanate materials will be presented.

2.6. References

[B.1] **J. F. Nye**, Physical properties of crystals, Clarendon Press, Oxford (1964): ISBN: 0198511655, 9780198511656

[B.2] **N. W. Ashcroft and N. D. Mermin**, Solid State Physics, Harcourt, New York (1976): ISBN 10: 0030839939, ISBN 13: 9780030839931

[B.3] **J. Guyonnet**, Domain Walls in Ferroelectric Materials – from Ferroelectric Domain Walls. Springer Theses pp 7-24 (2014): https://doi.org/10.1007/978-3-319-05750-7_2

[B.4] **B. Jaffe, W. R. Cook, and H. L. Jaffe**, Piezoelectric Ceramics, R. A. N, Ohio, USA (2002)

[B.5] **C. Kittel**, Theory of the Structure of Ferromagnetic Domains in Films and, Small particles. Phys. Rev. 70, 965 (1946): https://doi.org/10.1103/PhysRev.70.965

[B.6] **D. Wei**, Micromagnetics and Recording Materials. Springer Science & Business Media (2012): ISBN: 978-3-642-28577-6

[B.7] **G. Catalan, J. F. Scott, A. Schilling and J. M. Gregg**, Wall thickness dependence of the scaling law for ferroic stripe domains. J. Phys. Condens. Matter. 19, 022201 (2007): https://doi.org/10.1088/0953-8984/19/2/022201

[B.8] **G. Catalan, H. Bea, S. Fusil, M. Bibes, P. Paruch, A. Barthelemy, and J. F. Scott**, Fractal Dimension and Size Scaling of Domains in Thin Films of Multiferroic $BiFeO_3$. Phys. Rev. Lett. 100, 027602 (2008): https://doi.org/10.1103/PhysRevLett.100.027602

[B.9] **D. Lee, R. K. Behera, P. Wu, H. Xu ,Y. L. Li, S. B. Sinnott, S. R. Phillpot, L. Q. Chen, and V.Gopalan**, Mixed Bloch-Néel-Ising character of 180° ferroelectric domain walls. Phys. Rev. B 80, 060102R (2009): https://doi.org/10.1103/PhysRevB.80.060102

[B.10] **Y. Gu, M. Li, A. N. Morozovska, Y. Wang, E. A. Eliseev, V. Gopalan, and L.-Q. Chen**, Flexoelectricity and ferroelectric d omain wall s tructures: Phase-field modeling and DFT calculations. Phys. Rev B 89, 174111 (2014): https://doi.org/10.1103/PhysRevB.89.174111

[B.11] **X.-K. Wei, C.-L. Jia, T. Sluka, B.-X. Wang, Z.-G. Ye, and N. Setter**, Neel-like domain walls in ferroelectric Pb(Zr,Ti)O_3 single crystals. Nat. Commun. 7, 12385 (2016): https://doi.org/10.1038/ncomms12385

[B.12] **W. J. Merz**, Domain Formation and Domain Wall Motions in Ferroelectric $BaTiO_3$, Single Crystals. Phys. Rev. 95, 690 (1954): https://doi.org/10.1103/PhysRev.95.690

[B.13] **W. J. Merz**, Domain properties in $BaTiO_3$. Phys. Rev. 88, 421 (1952): https://doi.org/10.1103/PhysRev.88.421

[B.14] **B.L. Cheng, M. Gabbay, M. Maglione, Y. Jorand and G. Fantozzi**, Domain Walls Motions in Barium Titanate Ceramics. J. Phys. IV, 06, C8, C8-647-C8-650(1996): http://dx.doi.org/10.1051/jp4:19968139

[B.15] **E. Nakamura**, Anomalous dielectric behaviour of KH_2PO_4 type crystals in the ferroelectric phase. Ferroelectrics, 135, 237-247 (1992): http://dx.doi.org/10.1080/00150199208230027

[B.16] **Y. L. Wang,a A. K. Tagantsev, D. Damjanovic, and N. Setter**, Giant domain wall contribution to the dielectric susceptibility in $BaTiO_3$ single crystals. Appl. Phys. Lett. 91, 062905 (2007): https://doi.org/10.1063/1.2751135

[B.17] **Y. L. Wang, Z. B. He, D. Damjanovic, A. K. Tagantsev, G. C. Deng, and N. Setter**, Unusual dielectric behaviour and domain structure in rhombohedral phase of $BaTiO_3$ single crystals. J. Appl. Phys. 110, 014101 (2011): http://dx.doi.org/10.1063/1.3605494

[B.18**] A. K. Tagantsev, L. E Cross, and J. Fousek**, Domains in Ferroic Crystals and Thin Films. Springer, New York (2010): ISBN 78-1-4419-1416-3

[B.19] **P. S. Bednyakov, T. Sluka, A. K. Tagantsev, D. Damjanovic and N. Setter,** Formation of charged ferroelectric domain walls with controlled periodicity. Sci. Rep. 5, 15819 (2015): http://dx.doi.org/10.1038/srep15819

[B.20] **J. Hlinka and P. Marton**, Phenomenological model of a 90° domain wall in $BaTiO_3$-type ferroelectrics. Phys. Rev. B 74, 104104 (2006): https://doi.org/10.1103/PhysRevB.74.104104

[B.21] **M. Y. Gureev, A. K. Tagantsev, and N. Setter**, Head-to-head and tail-to-tail 180º domain walls in an isolated ferroelectric. Phys. Rev. B 83, 184104 (2011): https://doi.org/10.1103/PhysRevB.83.184104

[B.22] **T. Sluka, A. K. Tagantsev, P. Bednyakov and N. Setter**, Free-electron gas at charged domain walls in insulating $BaTiO_3$. Nat. Comm. 4, 1808 (2013): http://dx.doi.org/10.1038/ncomms2839

[B.23**] L. Feigl, T. Sluka, L. J. McGilly, A. Crassous, C. S. Sandu and N. Setter**, Controlled creation and displacement of charged domain walls in ferroelectric thin films. Sci. Rep. 6, 31323 (2016): http://dx.doi.org/10.1038/srep31323

[B.24] **P. Bednyakov, T. Sluka, A. Tagantsev, D. Damjanovic, and N. Setter**, Free-Carrier-Compensated Charged Domain Walls Produced with Super-Bandgap Illumination in Insulating Ferroelectrics. Adv. Mater. 28, 43, 9498–9503 (2016): http://dx.doi.org/10.1002/adma.201602874

[B.25] **S.-E. Park, T. R. Shrout**, Ultrahigh strain and piezoelectric behavior in relaxor based ferroelectric single crystals. J. Appl. Phys. 82, 1804 (1997): http://dx.doi.org/10.1063/1.365983

[B.26] **G. Burns, F.H. Dacol**, Glassy polarization behavior in ferroelectric compounds $Pb(Mg_{1/3}Nb_{2/3})O_3$ and $Pb(Zn_{1/3}Nb_{2/3})O_3$. Solid State Commun. 48, 10, 853-856 (1983): http://dx.doi.org/10.1016/0038-1098(83)90132-1

[B.27] **A. A. Bokov, Z.-G. Ye**, Recent progress in relaxor ferroelectrics with perovskite structure. J. of Mat. Science, 41, 31 (2006): http://dx.doi.org/10.1007/s10853-005-5915-7

[B.28] **D. Viehland, S. J. Jang, L. E. Cross and M. Wuttig**, Freezing of the polarization fluctuations in lead magnesium niobate relaxors. J. Appl. Phys. 68, 6, 2916-2921 (1990): http://dx.doi.org/10.1063/1.346425

[B.29] **F. Chu, N. Setter and A. K. Tagantsev**, The spontaneous relaxor-ferroelectric transition of $Pb(Sc_{0.5}Ta_{0.5})O_3$. J. Appl. Phys. 74, 8, 5129-5134 (1993): http://dx.doi.org/10.1063/1.354300

[B.30] **G. A. Samara**, The relaxational properties of compositionally disordered ABO_3 perovskites. J. Phys.: Condens. Matter 15, R367–R411 (2003): https://doi.org/10.1088/0953-8984/15/9/202

[B.31] **W. Kleemann, G. A. Samara, and J. Dec**, Relaxor Ferroelectrics – from Random Field Models to Glassy Relaxation and Domain States, in Polar Oxides: Properties, Characterization, and Imaging (eds R. Waser, U. Böttger and S. Tiedke), Wiley-VCH Verlag GmbH & Co. KGaA, Weinheim, FRG. (2004): https://doi.org/10.1002/3527604650.ch15

[B.32] **R. A. Cowley, S. N. Gvasaliya, S. G. Lushnikov, B. Roessli, and G. M. Rotaru**, Relaxing with relaxors: a review of relaxor ferroelectrics. Advances in Physics 60, 2, 229–327 (2011): https://doi.org/10.1080/00018732.2011.555385

[B.33] **R Mackeviciute, M Ivanov, J Banys, N. Novak, Z. Kutnjak, M. Wencka and J F Scott**, The perfect soft mode: giant phonon instability in a ferroelectric. J. Phys.: Condens. Matter 25, 212201, 5pp (2013): https://doi.org/10.1088/0953-8984/25/21/212201

[B.34] **R. Grigalaitis, J. Banys, A. Brilingas, A. Sternberg, K. Bormanis, V. Zauls**, Distribution of Relaxation Times in 0.5PMN-0.5PSN Ceramics. Journal of Physics: Conference Series 93, 012019 (2007): https://doi.org/10.1088/1742-6596/93/1/012019

[B.35] **A. R. Damodaran, J. C. Agar, S. Pandya, Z. Chen, L. Dedon, R. Xu, B. Apgar, S. Saremi, and L. W Martin**, New modalities of strain-control of ferroelectric thin films. J. Phys.: Condens. Matter 28, 263001, 36pp, (2016): https://doi.org/10.1088/0953-8984/28/26/263001

[B.36] **N. A. Pertsev, A.G. Zembilgotov, A. K. Tagantsev**, Effect of mechanical boundary conditions on phase diagrams of epitaxial ferroelectric thin films. Phys. Rev. Lett. 80, 1988–91 (1998): https://doi.org/10.1103/PhysRevLett.80.1988

[B.37] **N. A. Pertsev, V. G. Koukhar**, Polarization instability in polydomain ferroelectric epitaxial thin films and the formation of heterophase structures.

Phys. Rev. Lett. 84, 3722–25 (2000): https://doi.org/10.1103/PhysRevLett.84.3722

[B.38] **Y. L. Li, S. Y. Hu, Z. K. Liu, L. Q. Chen**, Phase-field model of domain structures in ferroelectric thin films. Appl. Phys. Lett. 78, 3878–80 (2001): http://dx.doi.org/10.1063/1.1377855

[B.39] **V. G. Koukhar, N. A. Pertsev, R. Waser**, Thermodynamic theory of epitaxial ferroelectric thin films with dense domain structures. Phys. Rev. B 64, 214103 (2001): https://doi.org/10.1103/PhysRevB.64.214103

[B.40] **J. H. Haeni , P. Irvin, W. Chang, R. Uecker, P. Reiche, Y. L. Li, S. Choudhury, W. Tian, M. E. Hawley, B. Craigo, A. K. Tagantsev, X. Q. Pan, S. K. Streiffer, L. Q. Chen, S. W. Kirchoefer, J. Levy, and D. G. Schlom**, Room-temperature ferroelectricity in strained $SrTiO_3$. 2004 Nature 430, 758 (2004): https://doi.org/10.1038/nature02773

[B.41] **K. J. Choi, M. Biegalski, Y. L. Li, A. Sharan, J. Schubert, R. Uecker, P. Reiche, Y. B. Chen, X. Q. Pan, V. Gopalan, L.Q. Chen, D. G. Schlom, and C. B. Eom**, Enhancement of Ferroelectricity in Strained $BaTiO_3$ Thin Films. Science, 306, 5698,1005-9 (2004): https://doi.org/10.1126/science.1103218

[B.42] **S. Wada, T. Muraishi, K. Yokoh, K. Yako, H. Kamemoto, and T. Tsurumi**, DomainWall Engineering in Lead-Free Piezoelectric Crystals. Ferroelectrics, 355, 37–49 (2007): https://doi.org/10.1080/0015019070151

3. Measurement and calculation methods

In this chapter measurements of dielectric and impedance spectroscopies will be described. The method of dielectric spectroscopy was used for single crystal characterization. Meanwhile, impedance spectroscopy was used to characterize thin films. Also, theoretical models for characterization of dielectric and impedance spectra and Johnson approximation of the Landau-Ginsburg-Devonshire theory will be presented.

3.1. Experimental techniques of dielectric and impedance spectroscopy of single crystals and thin films

In the frequency range of 20 Hz – 1 MHz, capacitance C_m and tangent of losses $\mathrm{tg}\delta = \frac{\varepsilon''}{\varepsilon'}$ of the sample were measured using Hewlett Packard 4284 precision LCR meter. The same LCR meter was also used for impedance spectroscopy. In this case the resistance (R) and reactance (X) of complex impedance were measured. For all measurement the silver paste (in some cases magnetron sputtered indium tin oxide (ITO) and silver paste) has been used to ensure electrical contact.

Complex dielectric permittivity was calculated from the plane capacitor formulas [C.1]:

$$\varepsilon' = \frac{(C_m - C_0)d}{\varepsilon_0 S} + 1,$$
$$\varepsilon'' = \varepsilon' tg\delta = \frac{C_m tg\delta_m - C_0 tg\delta_0}{C_m - C_0}, \quad (3.1)$$

where: C_m and $tg\delta_m$ are capacitance and tangent of losses of the systems with the sample, C_0 and $tg\delta_0$ are capacitance and tangent of losses of the systems without the sample, d is height of the sample, S is the area of the sample, ε_0 is the dielectric permittivity of vacuum.

Complex specific resistivity was calculated according to following equation:

$$\rho^* = Z^* \frac{S}{d}, \tag{3.2}$$

where: Z^* is a complex impedance ($Z^* = R - jX$), S is the area of the sample and d is the height of the sample. In order to get complex dielectric permittivity, several steps should be done. The expression of complex conductivity should be taken into account:

$$\sigma^* = \sigma' + j\sigma'' = j\varepsilon_0 \omega \varepsilon^*, \tag{3.3}$$

where: σ' and σ'' are the real and imaginary parts of conductivity, ω is cyclic frequency and ε^* is a complex dielectric permittivity. Also, complex conductivity can be expressed as following:

$$\sigma^* = \frac{\rho^*}{|\rho^*|^2}. \tag{3.4}$$

Taking into account conductivity expressions presented in Eq. 3.3 and Eq. 3.4, the complex dielectric permittivity is equal to:

$$\varepsilon^* = \frac{1}{j\omega\varepsilon_0} \cdot \frac{\rho^*}{|\rho^*|^2}. \tag{3.5}$$

For single crystal measurements, inductance and resistance of cables and silver contact is negligible at low frequencies, thus system was calibrated by capacitance measurement of empty system. The area of the sample was kept larger than the thickness so that the fringing field effects were insignificant. Temperature was measured using 100 Ω platinum sensor and Keithley Integra 2700 multimeter. Temperature was varied with approximately 1 K/min rate. Homemade furnace (from room T up to 500 K) was used for sample heating above room temperature (see Fig. 3.1).

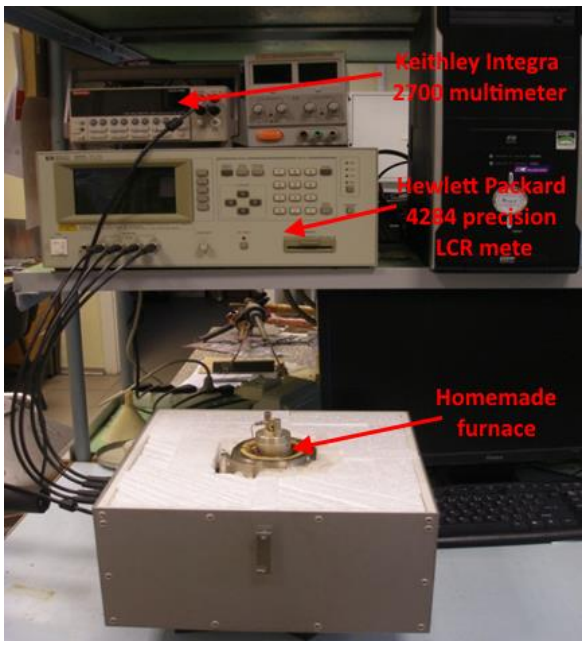

Fig. 3.1 The measuring system of dielectric spectroscopy of bulk materials (in this case, single crystals) at frequency range of 20 Hz – 1 MHz.

For epitaxial film measurements, the thick film sample holder was used to characterize electrical and piezoelectrical properties of thick or thin film samples (Fig. 3.2 a) and b)). Top and bottom contact of the sample are both connected by two probe tips on the sample top surface (see c) in Fig. 3.2). Sample positioning should be done very accurately and responsibly in order to avoid damage of thin film or probe tip. Hence, the following steps should be performed. First of all the acrylic glass box of the thick film sample holder should be removed and the sample should be placed in the centre of the heater unit. Carefully contact to the top and bottom electrode of the sample with the help of the two positioners. For an easy contacting of even small pads, the microscope camera was used. As an example, the area of the top electrode was equal to 0,009 mm^2 and 0,031 mm^2 in the case of PMN-PT and BST thin films respectively. For temperature dependent measurements, the setup was heated by an internal hot plate on which the sample was placed. The measuring temperature range was from room T to 500 K and the temperature change rate was approximately equal to 1 K/min.

a)

b)

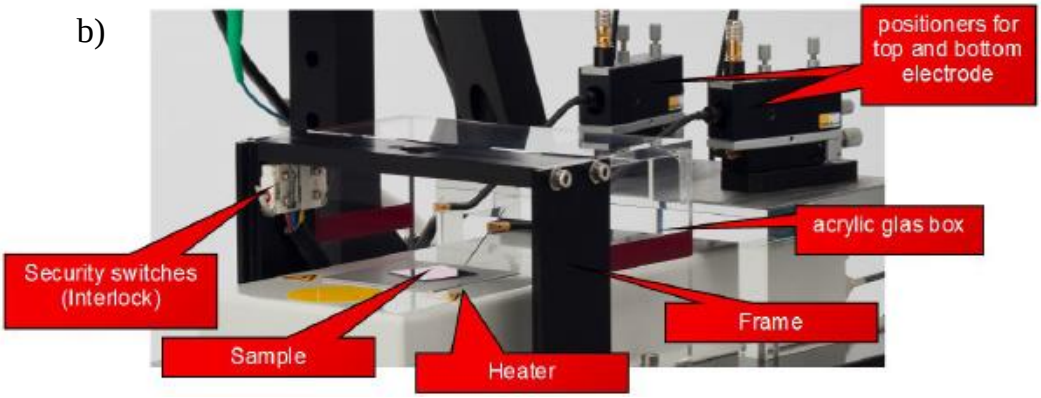

c)

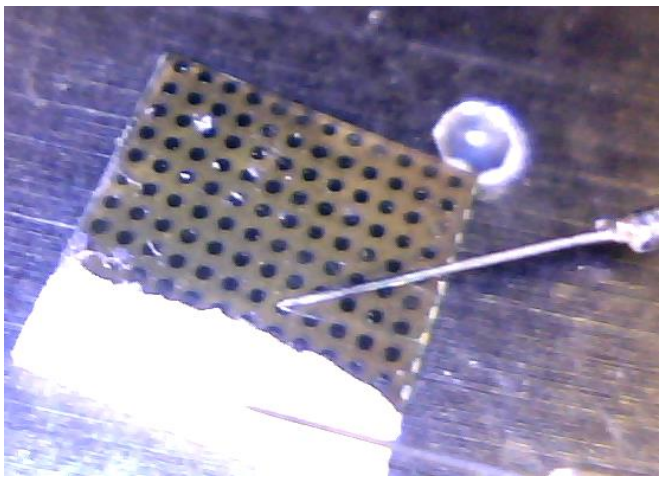

Fig. 3.2 a) and b) represents a view of the aixACCT thick film sample holder, c) represents an enlarged sample view.

In order to perform complex impedance measurements, thick film sample holder was connected to the Hewlett Packard 4284 precision LCR meter. During the system setup and measurement procedure, several obstacles

were faced. First of all, it was very important to find not damaged sample part (the top electrode should not be diffused through all film area). Also, the good electrical contact between the sample and probe tip was disappearing, because of the temperature gradient arising in the thin film during the heating and cooling cycles. These cases caused the repetitions of measuring procedures. In some cases, to get acceptable experimental results the measuring process was repeated more than couple of times.

Meanwhile, thin and thick film characterization equipment TF Analyser 2000 (aixACCT) was used for measurements of ferroelectric hysteresis loops and electric field tunability. Ferroelectric hysteresis loops and electric field tunability of real and imaginary parts of dielectric permittivity were measured in the 300 – 450 K temperature range and at a frequency of 1 kHz.

3.2. Theoretical models for characterization of dielectric and impedance spectra

One of the main attribute of disordered materials like ferroelectric relaxors, dipolar glasses and incipient ferroelectrics is very broad dielectric dispersion close to some critical temperature. Ferroelectric dispersion can be approximated by Debye formula [C.2]:

$$\varepsilon^*(\omega) = \varepsilon_\infty + \frac{\Delta\varepsilon}{1 + i\omega\tau}, \tag{3.6}$$

where: ε_∞ is a contribution from all higher frequency processes, like electronic and ionic contribution, $\Delta\varepsilon$ is relaxation strength and ω is cyclic frequency.

In disordered materials dielectric dispersion is very broad and cannot be described by one relaxation time, thus and ensemble of Debye type processes is considered:

$$\begin{aligned} \varepsilon'(\omega) &= \varepsilon_\infty + \Delta\varepsilon \int_{-\infty}^{+\infty} \frac{f(\ln\tau)}{1 + (\omega\tau)^2} d(\ln\tau), \\ \varepsilon''(\omega) &= \Delta\varepsilon \int_{-\infty}^{+\infty} \frac{f(\ln\tau)(\omega\tau)}{1 + (\omega\tau)^2} d(\ln\tau). \end{aligned} \tag{3.7}$$

These two equations (first kind of Fredholm integral equations) define relaxation time distribution function $f(\tau)$. Different relaxation time distribution function $f(\tau)$ can fulfil (3.7) equations at the same $\varepsilon^*(\omega)$. One of the method for solving Eq. (3.7) system is to choose such $f(\tau)$, that it would be possible to integrate analytically. There are few predefined relaxation time distribution functions; one of them is Cole-Cole function [C.3]:

$$f(\tau) = \frac{\sin \alpha_{cc}\,\pi}{cosh\left[(1-\alpha_{cc})ln2\pi\frac{\tau_{cc}}{\tau}\right] - \cos \alpha_{cc}\pi}, \tag{3.8}$$

where: $0 \leq \alpha_{cc} \leq 1$ is a parameter describing the width of the Cole-Cole function and τ_{cc} is a mean and most probable relaxation time. After insert of Eq. 3.8 to Eq. 3.7, the following expression of $\varepsilon^*(\omega)$ is obtained:

$$\varepsilon^*(\omega) = \varepsilon_\infty + \frac{\Delta\varepsilon}{1 + (i\omega\tau_{cc})^{1-\alpha_{cc}}}. \tag{3.9}$$

This formula describes dielectric permittivity with symmetrical relaxation time distribution. When this function is asymmetric one can use superposition of Cole-Cole functions or another asymmetric function like Cole-Davidson [C.4]:

$$f(\tau) = \frac{\sin \gamma\pi}{\pi}\left(\frac{\tau}{\tau_{CD}-\tau}\right)^{\beta}, \tau < \tau_{CD}, f(\tau) = 0\ when\ \tau > \tau_{CD}, \tag{3.10}$$

where: τ_{CD} is a most probable relaxation time according to Cole-Davidson function. β is a parameter describing asymmetry of spectra. From Eq. 3.10 and Eq. 3.7 the following expression is obtained:

$$\varepsilon^*(\omega) = \varepsilon_\infty + \frac{\Delta\varepsilon}{(1 + i\omega\tau_{CD})^{\beta}}. \tag{3.11}$$

Havriliak-Negami function [C.5, C.6] is obtained after summing Cole-Cole and Cole-Davidson formulas. This function is useful describing very broad and asymmetric dielectric permittivity dispersions:

$$\varepsilon^*(\omega) = \varepsilon_\infty + \frac{\Delta\varepsilon}{(1 + (i\omega\tau_{HN})^{1-\alpha_{cc}})^{\beta}}, \tag{3.12}$$

and relaxation time distribution function:

$$f(\tau) = \frac{1}{\pi} \frac{\left(\frac{\tau}{\tau_{HN}}\right)^{(1-\alpha_{cc})\beta} \sin(\gamma\Theta)}{\left[\left(\frac{\tau}{\tau_{HN}}\right)^{2(1-\alpha_{cc})} + 2\left(\frac{\tau}{\tau_{HN}}\right)^{(1-\alpha_{cc})} \cos\pi(1-\alpha_{cc}) + 1\right]^{\frac{\beta}{2}}}, \tag{3.13}$$

$$\Theta = arctan \frac{\sin\pi(1-\alpha_{cc})}{\left(\frac{\tau}{\tau_{HN}}\right)^{(1-\alpha_{cc})} + \cos\pi(1-\alpha_{cc})}.$$

Dielectric dispersion in disordered materials in the best way is described by Havriliak-Negami function. Major difficulty of using Cole-Cole, Cole-Davidson, Havriliak-Negami, and many more [C.7] is that relaxation time distribution function needs to be known a prior.

The comparison of Cole-Cole, Cole-Davidson, Havriliak-Negami relaxations with Debye type relaxation is shown in Fig 3.3. Here, for theoretical modelling the following parameters were used: $\alpha_{cc} = 0{,}5$, $\alpha_{HN} = 0{,}5$ and $\beta = 0{,}5$. According to these theoretical modelling, some conclusions can be aligned: Debye relaxation is the narrowest and with a fixed width; the width of Cole-Cole relaxation can be varied by changing value of α_{cc} parameter; in the case of Havriliak-Negami relaxation, width and asymmetry can be varied by changing values of α_{cc} and β parameters respectively. Meanwhile, Cole-Davidson relaxation has almost the same width as Debye relaxation, but spectrum becomes asymmetric and can be varied by changing γ parameter.

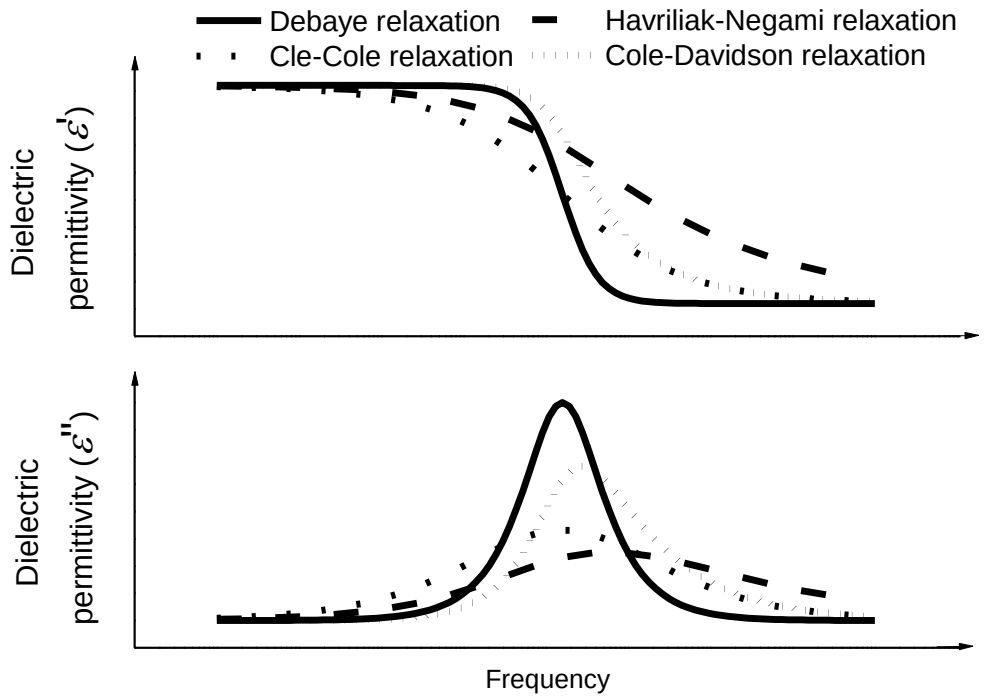

Fig. 3.3 Theoretical comparison of Cole-Cole, Cole-Davidson, Havriliak-Negami relaxations with Debye type relaxation. The following parameters were used: $\alpha_{cc} = 0{,}5$, $\alpha_{HN} = 0{,}5$ and $\beta = 0{,}5$ for theoretical modelling.

The temperature dependence of the mean relaxation time (from Cole-Cole, Cole-Davidson, Havriliak-Negami functions and relaxation times distribution function) can be approximated by Arrhenius (Eq.3.14) or Vogel Fulcher laws (Eq. 2.6):

$$\tau = \tau_0 exp\left(\frac{E_a}{k_B T}\right), \tag{3.14}$$

where: τ_0 is the attempt relaxation time at very high temperature, E_a is the activation energy for the analysed process.

Arrhenius law typically describes ferroelectric materials with almost independently relaxing dipoles and Vogel-Fulcher law (originally developed for glass viscosity description [C.8]) better depicts disordered material behaviour, like dipolar glass freezing phenomena or critical slowing down in nonergodic ferroelectric relaxors phase at positive temperatures [C.9].

3.3. dc electric-field dependence of the dielectric permittivity in polar dielectrics

In most electronic materials the change in dielectric constant with applied electric field is an effect too small to be useful or even easily measurable. But for a special class of high-permittivity materials the effect can be quite pronounced. This chapter presents the way to relate the field dependence of polarization and dielectric constants [C.10].

3.3.1. Landau-Ginsburg-Devonshire theory

The dielectric constant of polar dielectrics changes significantly with the applied external electric field (*E*), and nonlinear behaviour occurs. The phenomenological treatments of the dc electric-field dependence of the dielectric constant in polar dielectrics are currently within the framework of LGD theory [C.11-C.13].

Starting with the LGD expression for the free energy, the dependence of the dielectric constant on the electric field is derived from the polarization-field *P*(E) dependence given by the implicit equation:

$$E = \alpha P + \beta P^3 + \gamma P^5 + \cdots. \tag{3.15}$$

Also, the second derivative of Eq. 3.15 is equal to:

$$\frac{\partial E}{\partial P} = \alpha + 3\beta P^2 + 5\gamma P^4 + \cdots. \tag{3.16}$$

According to the following relation

$$P = \varepsilon_0 \varepsilon_r(E) \cdot E, \tag{3.17}$$

and the definition of the electric susceptibility ($P = \varepsilon_0 \chi_e E$, where $\chi_e = \varepsilon_r(E) - 1$), a relation between permittivity and the applied field is derived:

$$\frac{\varepsilon_r(E)}{\varepsilon_r(0)} = \frac{\left\{1 - \frac{\varepsilon_r(E)}{\varepsilon_r(0)} + \left[\frac{\varepsilon_r(E)}{\varepsilon_r(0)}\right]^3\right\}^{1/3}}{[1 + 3\beta\varepsilon_r(0)^3\varepsilon_0^3 E^2]^{1/3}}, \tag{3.18}$$

here: $\varepsilon_r(0)$ and $\varepsilon_r(E)$ are the permittivity in the absence/presence of the electric field, respectively. Also, the expression of temperature dependant coefficient was taken into account:

$$\alpha = C(T - T_0) = \frac{1}{\varepsilon_0 \varepsilon_r(0)}. \quad (3.19)$$

In this complicated form (see Eq. 3.18) the relation is not useful for fitting the experimental data. Some of the terms can be simplified to give a more adequate and easy working relation, as described in the following.

3.3.2. Johnson's relationship

The Johnson's approximation was developed by assuming small polarization values. Johnson gave a semi empirical relation starting from the equation (3.18), where the numerator was approximated to 1. Thus, a semi-empirical relation is obtained:

$$\varepsilon_r(E) = \frac{\varepsilon_r(0)}{\{1 + 3\beta[\varepsilon_0 \varepsilon_r(0)]^3 (E)^2\}^{1/3}}, \quad (3.20)$$

which is called the Johnson's approximation. This relation can be used only when $\beta > 0$, because in the other case it is necessary to include at least the fourth-order terms in the free energy development.

This theoretical model was approved with experimental results of paraelectric $KTaO_3$ and dielectric relaxor Bi:$SrTiO_3$, which were presented by *Chen Ang et al*. [C.10, C.14]

3.4. Theoretical models for impedance spectroscopy analysis

Impedance spectroscopy is a powerful tool to study many of the electrical properties of bulk materials or thin films. The dielectric relaxation processes observed in the grain, grain boundaries and the electrode interface regions or in the epitaxial thin films and film/electrode interface can be analysed in details. In practice, it is usually possible to find more than one equivalent circuit that fits, numerically, a given data set, but only one of these is likely to provide a realistic representation of the electrical makeup of the sample. In this paragraph theoretical models for impedance analysis in non-epitaxial and epitaxial thin films will be presented.

3.4.1. Theoretical model for impedance analysis in non-epitaxial thin films

The electrical properties observed in non-epitaxial thin films are determined in general by a series combination of impedances, which describes the relaxation process of the grain, grain boundaries and the electrode interface regions [C.15]. Each of these components may be represented by a parallel RC element, and the simplest appropriate equivalent circuit is a series array of parallel RC elements (Fig. 3.4).

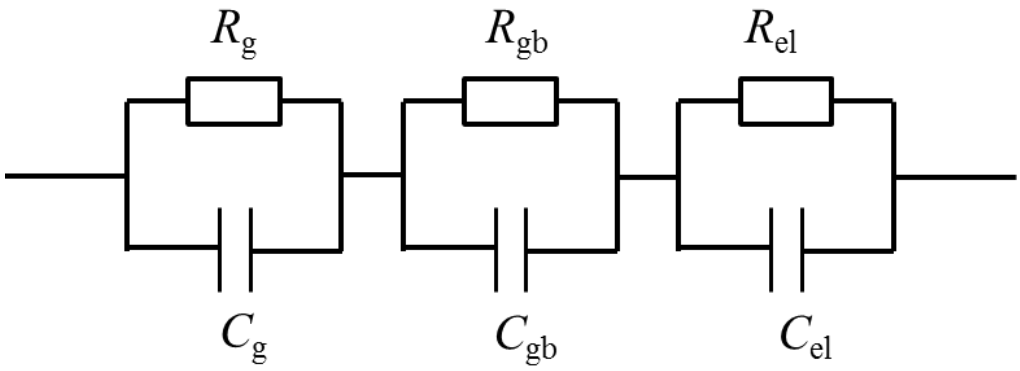

Fig. 3.4 Equivalent circuit used to represent the electrical properties of grain and grain boundary and electrode interface regions effects.

In order to find the total complex impedance, the following equation can be presented:

$$Z^*(\omega) = \left(\frac{1}{R_g} + j\omega C_g\right)^{-1} + \left(\frac{1}{R_g b} + j\omega C_{gb}\right)^{-1} + \left(\frac{1}{R_{el}} + j\omega C_{el}\right)^{-1}, \quad (3.21)$$

where

$$\begin{aligned} Z'(\omega) &= \frac{R_g}{1 + \left(\omega R_g C_g\right)^2} + \frac{R_{gb}}{1 + \left(\omega R_{gb} C_{gb}\right)^2} + \frac{R_{el}}{1 + (\omega R_{el} C_{el})^2}, \\ Z''(\omega) &= \frac{R_g\left(\omega R_g C_g\right)}{1 + \left(\omega R_g C_g\right)^2} + \frac{R_{gb}\left(\omega R_{gb} C_{gb}\right)}{1 + \left(\omega R_{gb} C_{gb}\right)^2} + \frac{R_{el}(\omega R_{el} C_{el})}{1 + (\omega R_{el} C_{el})^2}, \end{aligned} \quad (3.22)$$

here: ω is cyclic frequency; R_g, R_{gb} and R_{el} represent the grain resistance, the grain boundary resistance and the electrode-solid interface resistance,

respectively; C_g, C_{gb} and C_{el} represent the grain capacitance, the grain boundary capacitance and the electrode-solid capacitance.

In general, all these quantities can be treated as fitting parameters whose values can be retrieved from the best fit to the experimental data. The fitting is relatively unambiguous, because the elements of three circuits dominate in different frequency regions. In the ideal case, Nyquist plots looks as semi-circles with centres on the *x*-axis. Meanwhile, in the real measuring systems Nyquist plots consist of semi-circles with centres below the *x*-axis indicating that the measuring system electrical response exhibits a kind of distributed impedance response, i.e. measuring system is not homogenous [C.16]. In order to evaluate this response, a distributing factor (*n*) in the equivalent circuit should be taken into account. Well known way to add distributing factor is to use constant-phase element.

An analogue circuit commonly used to model the electrode/solid interface is called a constant phase element (CPE) [C.17]. Since the first paper devoted to the CPE [C.18], the time constant dispersion was attributed to a dispersion of the capacity or to a change of the capacity with frequency. Cole and Cole [C.3] studied dispersion and absorption in dielectrics, and, obviously, the capacitance was the parameter under investigation. The major part of later theoretical work dedicated to this phenomenon considers the CPE to be associated with a distribution of the capacitance. Several extrinsic effects due to inhomogeneities, such as atomically rough interfaces between the electrode and the dielectric, strong differences between the edges and centres of electrodes and porosity of electrodes, are considered as potential causes for the need for CPEs in equivalent circuits [C.19].

In the literature different equations of CPE impedance CPE were proposed. In the following equations, *j* is the imaginary number and ω is the angular frequency. *Lasia et al.* [C.20] gives the impedance of the CPE as:

$$Z_{CPE} = \frac{1}{T(j\omega)^{\phi}}, \tag{3.23}$$

where: T is a constant in $\mathrm{Fcm^{-2}}\ s^{\phi-1}$ and ϕ is related to the angle of rotation of a purely capacitive line on the complex plane plots. Meanwhile, *Brug et al.* [C.21] proposed:

$$Z_{CPE} = \frac{Q}{(j\omega)^{1-\alpha}}, \tag{3.24}$$

where: Q is a constant (with dimensions $\Omega\mathrm{cm^2\ s^{-(1-\alpha)}}$) and $1-\alpha$ has the same meaning as ϕ in Eq. (4.2). *Zoltowski et al.* [C.22] proposed two definitions:

$$Z_{CPE} = \frac{1}{Q_a(j\omega)^{\alpha}}, \tag{3.25}$$

and

$$Z_{CPE} = \frac{1}{(Q_b j\omega)^{\alpha}}. \tag{3.26}$$

The dimensions of Q_a and Q_b $\Omega^{-1}\mathrm{m^{-2}}s^{\alpha}$or $(Q\mathrm{m^2})^{-1/\alpha}s^{\alpha}$, respectively.

A combination of these expressions can be also found. Here, I would like to use a following CPE impedance expression [C.23]:

$$Z_{CPE} = \left(\frac{1}{A}\right)\cdot(j\omega)^{-n}, \tag{3.27}$$

where: ω is the angular frequency, A and n are experimental parameters and $0 \le n \le 1$. The CPE describes an ideal capacitor with $C = A$ for $n = 1$ and an ideal resistor with $R = 1/A$ for $n = 0$. Thus, equation (3.21) is modified as

$$Z^*(\omega) = \left(\frac{1}{R_g} + A_g(j\omega)^{n_g}\right)^{-1} + \left(\frac{1}{R_{gb}} + A_{gb}(j\omega)^{n_{gb}}\right)^{-1} + \left(\frac{1}{R_{el}} + A_{el}(j\omega)^{n_{el}}\right)^{-1}. \tag{3.28}$$

Using the above equation, measuring systems with distributed impedance response can be described and the distributing factor (n) can be found. From literature is known that distributing factor (n) in ferroelectric perovskite oxides like PZT/Pt and BST/Pt, is typically between 0.93 and 0.99 [C.19]. Meanwhile, *Martinez et al.* [C.16] showed that obtained distributing factor of experimental results of $Ba_{0.7}Sr_{0.3}TiO_3/La_{0.7}Sr_{0.3}MnO_3$ heterostructure after approximation was equal to $n = 0.6 - 0.7$. This value is unusually low and was explained because of large inhomogeneity effects.

3.3.2. Theoretical model for impedance analysis in epitaxial thin films

Several examples of theoretical models used for impedance analysis in epitaxial thin films can be found in the literature. *Tang et al.* [C.24] investigated dielectric relaxation and polaronic conduction in epitaxial $BaFe_{12}O_{19}$ hexaferrite thin film. Here, the equivalent circuit based on brick-layer model [C.25] was suggested in order to analyse experimental results.

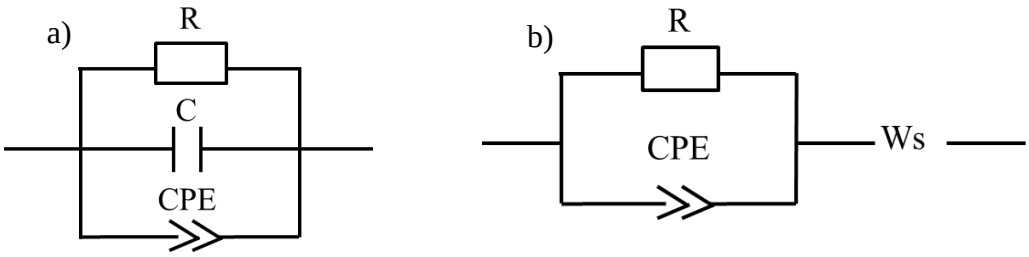

Fig. 3.5 Equivalent circuit based on the brick-layer model for the impedance spectra suggested by *Tang et. all.* (a) and Equivalent circuit for the impedance spectra suggested by *Kosacki et al.* (b).

In Fig. 3.5 (a), *R* and *C* represents the resistance and capacitance of the film material, respectively, CPE is the constant phase element indicating the departure from ideal Debye-type model. The CPE admittance is $Y_{CPE} = A_0(j\omega)^n$, where the parameter *n* is equal to 0 for ideal resistor and 1 for ideal capacitor [C.25, C.26]. Hence, the equivalent circuit in Fig. 3.5 (a) can be represented with the following equation:

$$Z^* = Z' - jZ'' = \frac{1}{R^{-1} + j\omega C + A_0(j\omega)^n}. \tag{3.29}$$

Meanwhile, *Kosacki et al.* [C.27] suggested to use equivalent circuit consisting of the parallel connected resistor (R) and capacitor described by the Constant Phase Element for thin film response and series connected element which is described by Warburg impedance (W_s) for electrode related response (see Fig. 3.5 (b)). It is well known that, in electrochemical systems with diffusion, the impedance is modelled by the so-called Warburg element, where original Warburg impedance formula is following:

$$W_s = A_w(1 - j)\omega^{-1/2}, \tag{3.30}$$

where: A_w is Warburg coefficient, j is the imaginary number and ω is the radial frequency [C.28]. In most cases presented in the literature, Warburg element is used describing complex impedance of botanical systems or solid electrolytes.

As mentioned in this chapter, constant phase element (CPE) can be used analysing impedance spectra of ferroelectric and non-ferroelectric and epitaxial and non-epitaxial thin films. CPE is a non-intuitive circuit element that was discovered (or invented) while looking at the response of real-world systems, i.e. CPE is a mathematical expression which shows that there is some distribution (dispersion) of the value of some physical property of the system. According to author [C.29], impedance distribution factor (n), which appears in all real measuring systems, can be explained and named as a resistivity distribution of the bottom contact of measuring thin film system. Moreover, this theoretical assumption was applied and proved during analysis of experimental results of complex impedance in ferroelectric epitaxial thin films. The detail explanation of electrical model of a thin dielectric film with a bottom electrode of negligible distributed resistance will be presented in the following chapter.

3.5. References

[C.1] **A. Brant**, Issledovanie dielektrikov na sverkhvysokikh chastotakh. Moskva: Fizmatgiz, (1963).

[C.2] **J. Grigas**, Microwave Dielectric Spectroscopy of Ferroelectrics. OPA Amsterdam Gordon & Breach Publ. Inc.: (1996)

[C.3] **K. S. Cole and R. H. Cole**, Dispersion and Absorption in Dielectrics I. Alternating Current Characteristics. J. Chem. Phys. 9, 341 (1941): http://dx.doi.org/10.1063/1.1750906

[C.4] **D. W. Davidson and R. H. Cole**, Dielectric Relaxation in Glycerol, Propylene Glycol, and n-Propanol. J. Chem. Phys. 19, 1484 (1951): http://dx.doi.org/10.1063/1.1748105

[C.5] **S. Havriliak and S. Negami**, A complex plane analysis of α-dispersions in some polymer systems. J. Polym. Sc. C. 14, 99 (1966): http://dx.doi.org/10.1002/polc.5070140111

[C.6] **S. Havriliak and S. Negami**, A Complex Plane Representation of Dielectric and Mechanical Relaxation Processes in Some Polymers. Polymer., 8, 161 (1967): http://dx.doi.org/10.1016/0032-3861(67)90021-3

[C.7] **R. Zorn**, Logarithmic moments of relaxation time distributions. J. Chem. Phys., 116, 8 (2002): http://dx.doi.org/10.1063/1.1446035

[C.8] **L. Dagdug**, A theoretical framework for the Vogel–Fulcher–Tammann equation for covalent network glasses derived by the stochastic matrix method. J. Phys.: Condens. Matter, 12, 9573 (2000)

[C.9] **A. Levstik, Z. Kutnjak, C. Filipic and R. Pirc**, Glassy freezing in relaxor ferroelectric lead magnesium niobate. Phys. Rev. B., 57, 11204 (1998): https://doi.org/10.1103/PhysRevB.57.11204

[C.10] **C. Ang and Z. Yu**, dc electric-field dependence of the dielectric constant in polar dielectrics: Multipolarization mechanism model. Phys. Rev. B., 69, 174109 (2004): https://doi.org/10.1103/PhysRevB.69.174109

[C.11] **K. M. Johnson**, Variation of Dielectric Constant with Voltage in Ferroelectrics and Its Application to Parametric Devices. J. Appl. Phys. 33, 2826 (1962): http://dx.doi.org/10.1063/1.1702558

[C.12] **M. E. Drougard, R. Landauer, and D. R. Young,** Dielectric Behavior of Barium Titanate in the Paraelectric State. Phys. Rev. 98, 1010 (1955): https://doi.org/10.1103/PhysRev.98.1010

[C.13] **E. Stern and A. Lurio**, Dielectric Properties of $BaTi0_3$ Single Crystals in the Paraelectric State from 1 kc/sec to 2000 Mc/sec. Phys. Rev. 123, 117 (1961): https://doi.org/10.1103/PhysRev.123.117

[C.14] **C. Ang and Z. Yu**, Dielectric relaxor and ferroelectric relaxor: Bi-doped paraelectric $SrTiO_3$. J. Appl. Phys. 91, 1487 (2002): http://dx.doi.org/10.1063/1.1428799

[C.15] **D. C. Sinclair and A. R. West**, Impedance and modulus spectroscopy of semiconducting $BaTi0_3$ showing positive temperature coefficient of resistance. J. Appl. Phys. 66, 8 (1989): http://dx.doi.org/10.1063/1.344049

[C.16] **R. Martınez, A. Kumar, R. Palai, J. F. Scott and R. S. Katiyar**, Impedance spectroscopy analysis of $Ba0.7Sr0_3TiO_3/La0.7Sr0.3MnO_3$ heterostructure. J. Phys. D: Appl. Phys. 44, 105302, (8pp) (2011): http://dx.doi.org/ 10.1088/0022-3727/44/10/105302

[C.17] **J. B. Jorcin, M. E. Orazem, N. Pebere and B. Tribollet**, CPE analysis by local electrochemical impedance spectroscopy. Electrochimica Acta, 51, 1473–1479 (2006): http://dx.doi.org/10.1016/j.electacta.2005.02.128

[C.18] **H. Fricke**, The Theory of Electrolytic Polarization. Philos. Mag., 14, 310 (1932)

[C.19] **F. D. Morrison, D. J. Jung and J. F. Scott**, Constant-phase-element (CPE) modeling of ferroelectric random-access memory lead zirconate-titanate (PZT) capacitors. J. Appl. Phys. 101 094112 (2007): http://dx.doi.org/10.1063/1.2723194

[C.20] **A. Lasia**, **R.E. White, B.E. Conway, J.O'M. Bockris** (Eds.), Modern Aspects of Electrochemistry, 32, Kluwer Academic/Plenum Publishers, New York, p. 143. (1999)

[C.211] **G. J. Brug, A. L. G. Van Den Eeden, M. Sluyters-Rehbach and J. H. Sluyters**, The analysis of electrode impedances complicated by the

presence of a constant phase element. J. Electroanal. Chem. 176, 275 (1984): http://dx.doi.org/10.1016/S0022-0728(84)80324-1

[C.22] **P. Zoltowski**, On the electrical capacitance of interfaces exhibiting constant phase element behaviour. J. Electroanal. Chem. 443, 149 (1998): http://dx.doi.org/10.1016/S0022-0728(97)00490-7

[C.23] **S. Sarkar, P. K. Jana and B. K. Chaudhuri**, Colossal internal barrier layer capacitance effect in polycrystalline copper (II) oxide. Appl. Phys. Lett. 92, 022905 (2008): http://dx.doi.org/10.1063/1.2834854

[C.24] **R. Tang, H. Zhou, R. Zhao, J. Jian, H. Wang, J. Huang, M. Fan, W. Zhang, H. Wang and H. Yang**, Dielectric relaxation and polaronic conduction in epitaxial $BaFe_{12}O_{19}$ hexaferrite thin film. J. Phys. D: Appl. Phys. 49, 115305 (6pp) (2016): http://dx.doi.org/10.1088/0022-3727/49/11/115305

[C.25] **O. Raymond, R. Font, N. Suárez-Almodovar, J. Portelles and J. M. Siqueiros**, Frequency-temperature response of ferroelectromagnetic $Pb(Fe_{1/2}Nb_{1/2})O_3$ ceramics obtained by different precursors. Part II. Impedance spectroscopy characterization. J. Appl. Phys. 97, 084108 (2005): http://dx.doi.org/10.1063/1.1870100

[C.26] **Q. Ke, X. Lou, Y. Wang and J. Wang**, Oxygen-vacancy-related relaxation and scaling behaviours of $Bi_{0.9}La_{0.1}Fe_{0.98}Mg_{0.02}O_3$ ferroelectric thin films. Phys. Rev. B 82, 024102 (2010): http://dx.doi.org/10.1103/PhysRevB.82.024102

[C.27] **I. Kosacki, C. M. Rouleau, P. F. Becher, J. Bentley, D. H. Lowndes,** Nanoscale effects on the ionic conductivity in highly textured YSZ thin films. Solid State Ionics 176, 1319–1326 (2005): http://dx.doi.org/10.1016/j.ssi.2005.02.021

[C.28] **E. Warburg**, Ueber die Polarisationscapacität des Platins. Annalen der Physik, 311, 125 (1901): http://dx.doi.org/10.1002/andp.19013110910

[C.29] **R. Mackevičiūtė, M. Ivanov, Š. Bagdzevičius, R. Grigalaitis, J. Banys**, Electrical model of a thin dielectric film with a bottom electrode of non-negligible distributed resistance. Ferroelectrics, 497, 114-125 (2016): http://dx.doi.org/10.1080/00150193.2016.1165023

4. Results and discussion

4.1. Electrical model of a thin dielectric film with a bottom electrode of negligible distributed resistance

In the previous chapter was mentioned that the impedance of measuring epitaxial thin film heterostructure is not homogenous. The impedance distribution can be evaluated by taking into account a distributing factor (*n*) and this can be done by using a constant-phase element (CPE). Here, I would like to propose a way, how the impedance distribution can be evaluated and the distribution factor (*n*), which appears in all real measuring systems, can be explained and named as a resistivity distribution of the bottom contact.

A model of distributed contact was developed and experimentally assessed for BST 70/30 thin film heterostructure ($Ba_{0.7}Sr_{0.3}TiO_3$pc[001]/ $La_{0.8}Sr_{0.2}MnO_3$pc[001]// $(La_{0.18}Sr_{0.82})(Al_{0.59}Ta_{0.41})O_3$pc[001] – BST/LSMO//LSAT for short). Schematic illustration of a model system is shown in Fig. 4.1. The system consists of a bottom electrode, a thin ferroelectric film and top electrode. If we have a system which is infinite along *y* axis, then the task converges to a one dimensional case. This is close to the truth, when top electrode is near to the edge of the substrate, where a metallic contact is present, and the dimensions of top electrode are much larger than the thickness of the thin layer. If we try to compare the resistance of two areas below top contact, we will see that the resistance values will differ, because the distances between the areas and the edge of the sample are different, or in other words, the resistivity of the bottom contact is distributed, i.e. depends on position of the measurement point.

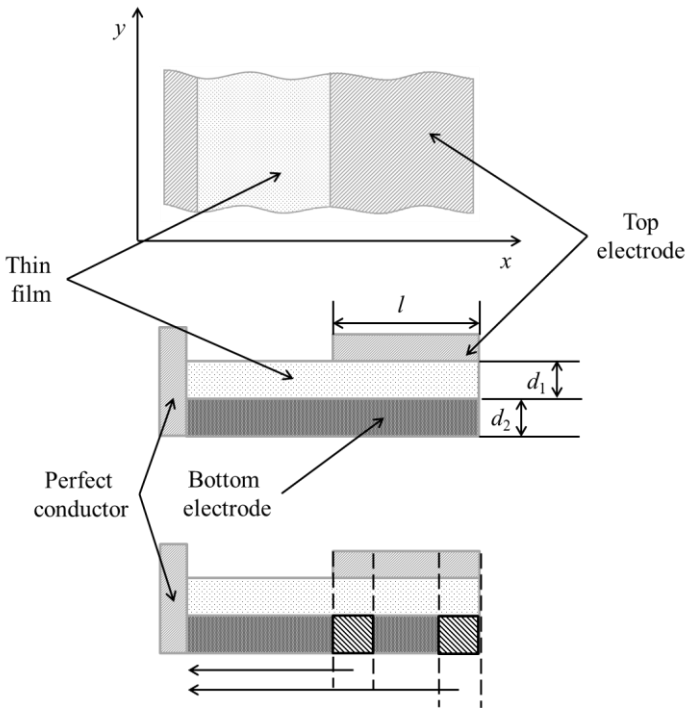

Fig. 4.1 Schematic illustration of the system.

The investigated thin film system could be described as equivalent circuit which consist only of resistors (*R*') and conductors (*G*'), where resistors and conductors represents top electrode and thin film respectively (see Fig. 4.2).

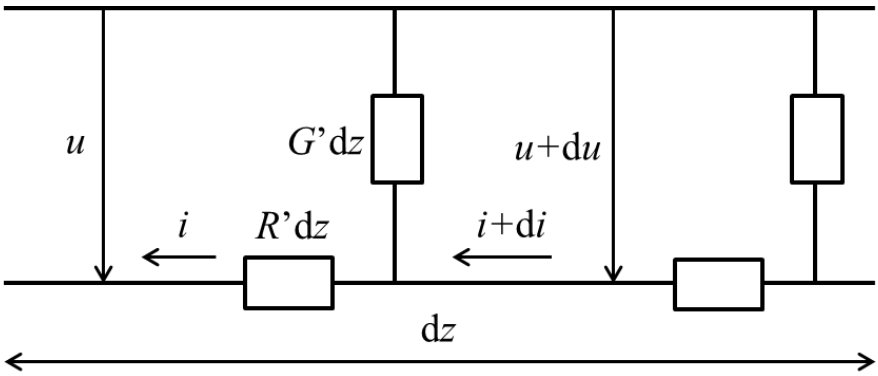

Fig. 4.2 Equivalent circuit of a small part of the system.

Therefore, our aim is mathematically to describe such a system. The theoretical model is based on the transition line with losses [D.1] and for this reason the differential equations of equivalent circuit with losses will be developed.

In order to find differential equations of equivalent circuit with losses, first of all, voltage and current propagation along the transition line should be introduced:

$$\begin{aligned} \mathrm{d}u &= \frac{\partial u}{\partial z}\mathrm{d}z, \\ \mathrm{d}i &= \frac{\partial i}{\partial z}\mathrm{d}z. \end{aligned} \tag{4.1}$$

Using the first and the second Kirchhoff laws the differential equations will be found, where resistivity (*R*') and conductivity (*G*') of the bottom contact and the film, correspondingly, both per unit length will be evaluated.

$$\begin{cases} u = iR'\mathrm{d}z + u + \dfrac{\partial u}{\partial z}\mathrm{d}z \\ i = uG'\mathrm{d}z + i + \dfrac{\partial i}{\partial z}\mathrm{d}z \end{cases}. \tag{4.2}$$

After mathematical transformations and introduction of propagation constant $\gamma^2 = R'G'$, which will be taken into account, Eq. 4.2 gets a following form:

$$\begin{cases} \dfrac{\partial^2 u}{\partial z^2} = \gamma^2 u \\ \dfrac{\partial^2 i}{\partial z^2} = \gamma^2 i \end{cases}. \tag{4.3}$$

The aim is to find a solution of the Eq. 4.3 in the form of $u = U(z)e^{i\omega t}$; $i = I(z)e^{i\omega t}$, where voltage and current amplitudes are equal to

$$\begin{aligned} U(z) &= U_a e^{-\gamma z} + U_b e^{\gamma z}, \\ I(z) &= I_a e^{-\gamma z} - I_b e^{\gamma z}. \end{aligned} \tag{4.4}$$

In order to find a solution of Eq. 4.3, the boundary conditions for the current and voltage should be found. Amplitudes of the current and voltage are related and has a following form: $I_a = \sqrt{\frac{G'}{R'}}U_a$; $I_b = \sqrt{\frac{G'}{R'}}U_b$. Using this relation and replacing *z* by *l* in the second equation of Eq. 4.4, boundary conditions for the current is found:

$$I(l) = \sqrt{\frac{G'}{R'}}U_a e^{-\gamma l} - \sqrt{\frac{G'}{R'}}U_b e^{\gamma l} = 0. \tag{4.5}$$

The total current is equal to zero, because the edge of the top electrode is not connected to any other circuit. Meanwhile, the boundary condition for the voltage at the edge of the electrode, which is closest to the edge of the substrate, can be found taking into account that the total voltage must be equal to the excitation voltage coming from an external generator. Now, I can write equations, which relate propagating signals in opposite directions:

$$\begin{cases} U_a e^{-\gamma l} - U_b e^{\gamma l} = 0 \\ U_a + U_b = U_0 \end{cases}. \tag{4.6}$$

After mathematical transformations, voltage amplitudes are equal to

$$U_a = U_0 \frac{e^{\gamma l}}{e^{-\gamma l} + e^{\gamma l}};\ U_b = U_0 \frac{e^{-\gamma l}}{e^{-\gamma l} + e^{\gamma l}}. \tag{4.7}$$

Therefore, the impedance of measuring thin film system is defined after taking into account both, current and voltage, boundary conditions:

$$Z = \sqrt{\frac{R'}{G'}} \cdot \frac{e^{\gamma l} + e^{-\gamma l}}{e^{\gamma l} - e^{-\gamma l}} = \sqrt{\frac{R'}{G'}} \cdot \frac{1}{\tanh(\gamma l)}. \tag{4.8}$$

Last step is to relate the unit length resistivity *R*' and unit length conductivity *G*' to the properties of the film and the bottom electrode:

$$G' = j\omega \frac{\varepsilon^* \varepsilon_0 l}{d_1}, \tag{4.9}$$

$$R' = \rho^* \frac{1}{l d_2}, \tag{4.10}$$

where: ρ^* is a complex resistivity of bottom electrode, l – size of the top electrode along y axis (the electrode will further be assumed of a square shape), d_1 – thickness of thin film, d_2 – thickness of bottom electrode, ε^* – complex dielectric permittivity of thin film, ε_0 – dielectric permittivity of vacuum.

Complex resistivity (ρ^*) and dielectric permittivity (ε^*) depend on frequency and could in the most general case be described as a superposition of the Havriliak-Negami type relaxations:

$$\rho^* = \frac{\Delta\rho}{(1 + (j\omega\tau_1)^{\alpha_1})^{\gamma_1}}, \tag{4.11}$$

$$\varepsilon^* = \varepsilon_\infty + \frac{\Delta\varepsilon}{(1 + (j\omega\tau_2)^{\alpha_2})^{\gamma_2}} + \frac{1}{j\omega\varepsilon_0\rho_c},$$

where: $\Delta\rho$ and $\Delta\varepsilon$ are relaxations strengths, τ_1 and τ_2 are mean relaxation times, α_1, α_2 and γ_1, γ_2 describes the asymmetry and broadness of the spectra respectively, ρ_c – a resistivity of thin film, ε_∞ – dielectric permittivity at high frequency limit.

Now, we are able to use Eq. (4.8) to approximate experimental data. This model is valid only if we have data of impedance in the whole dispersion region including all relevant processes. Unfortunately, this is rarely possible and leads to several problems. Frequency dependence of the simulated complex impedance using the model of distributed contact is presented in Fig. 4.3. Here, simulations were repeated two times with different values of dielectric permittivity at high frequency limit.

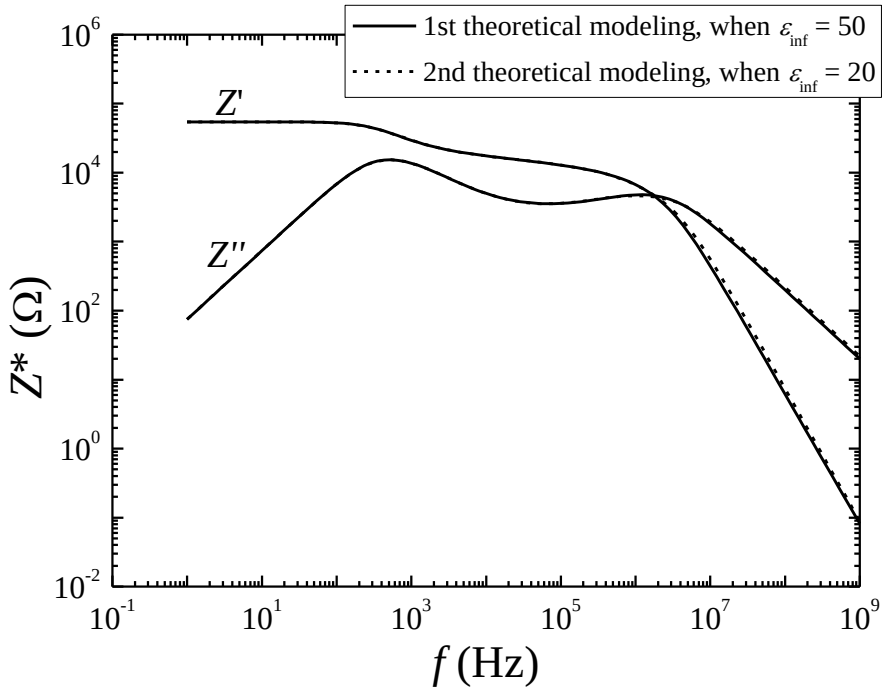

Fig. 4.3 Frequency dependence of the simulated complex impedance using the model of distributed contact.

There are no significant differences between simulated curves at frequency region from 1 Hz to 10^7 Hz despite different values of ρ_c and $\Delta\varepsilon$. This means

that the resistivity of thin film (ρ_c) and the relaxation strength of dielectric permittivity ($\Delta\varepsilon$) are tightly related i.e. parameter ρ_c is inversely proportional to parameter $\Delta\varepsilon$ (see Table 1), as they define the effective relaxation time of the impedance, which is macroscopically observed.

Table 1. Parameters values used for theoretical modelling of Eq. 4.8

	$\Delta\rho\ (\Omega \cdot m)$	$\tau_1\ (s)$	α_1	γ_1	$\rho_c\ (\Omega \cdot m)$
1st TM	$2 \cdot 10^6 \pm 0.2 \cdot 10^6$	$4.8 \cdot 10^{-8} \pm 0.2 \cdot 10^{-8}$	1	1	8946 ± 42
2nd TM	$7 \cdot 10^5 \pm 0.3 \cdot 10^5$	$3.4 \cdot 10^{-8} \pm 0.4 \cdot 10^{-8}$	1	1	26225 ± 1137
	$\Delta\varepsilon$	$\tau_2\ (s)$	α_2	γ_2	ε_∞
1st TM	5422 ± 47	$7 \cdot 10^{-5} \pm 0.1 \cdot 10^{-5}$	0.86 ± 0.01	0.89 ± 0.01	50
2nd TM	1855 ± 80	$6.6 \cdot 10^{-5} \pm 0.15 \cdot 10^{-5}$	0.84 ± 0.01	0.93 ± 0.01	20

Thus, initial values of these parameters are required for approximation of experimental results. In order to assess these values, we have to make some approximations. To achieve this goal, we will find a mathematical expression of the impedance at low frequency limit, because the low frequency measurements are widely available. Later, we will use a large contact limit and from these equations we will find initial values of resistivity and dielectric permittivity of the thin film.

In the case of the low frequency limit, when $\gamma l < 1$, we can separately find limits of exponential and root terms:

$$\lim_{\substack{\omega\to 0 \\ \gamma l\to 0}} Z = \lim_{\substack{\omega\to 0 \\ \gamma l\to 0}} \left(\sqrt{\frac{R'}{G'}} \cdot \frac{e^{\gamma l} + e^{-\gamma l}}{e^{\gamma l} - e^{-\gamma l}} \right). \tag{4.12}$$

So, after mathematical transformations, the equation of complex impedance becomes

$$\lim_{\substack{\omega\to 0\\ \gamma l\to 0}} Z = \frac{d_1}{l^2}\cdot\frac{1}{j\omega\varepsilon^*\varepsilon_0}. \tag{4.13}$$

Here we can insert the expression of complex dielectric permittivity, which separates electric conductivity of the film from the (possible complex) dielectric permittivity:

$$\varepsilon^* = \varepsilon_c^* + \frac{1}{j\omega\rho_c\varepsilon_0}, \tag{4.14}$$

where: ε_c^* – complex dielectric permittivity of thin film, ρ_c – a resistivity of thin film and ε_0 – dielectric permittivity of vacuum.

Assuming that the complex dielectric permittivity is described by Eq. 4.14 and also assuming that frequency is very low, the complex impedance adopts the form:

$$\lim_{\substack{\omega\to 0\\ \gamma l\to 0}} Z = \frac{d_1}{l^2}(\rho_c - j\omega\varepsilon_0\varepsilon_c^*\rho_c^2). \tag{4.15}$$

In the case of the large contact limit, we can ignore exponential term at Eq. (4.8), because in the case when $\gamma l \gg 1$ the hyperbolic tangent term becomes equal to unity. For example, if we say that γl is equal to 2 ($\gamma l = 2$), then hyperbolic tangent of γl is equal to 0.964, what is approximately unity. So, complex impedance equation takes a form of

$$\lim_{\gamma l\to\infty} Z = \sqrt{\frac{R'}{G'}} = \sqrt{\frac{\rho^*}{j\omega\varepsilon^*\varepsilon_0 l^2}\cdot\frac{d_1}{d_2}}. \tag{4.16}$$

Next step is to insert the expression of complex dielectric permittivity (Eq. 4.14) into previous equation and such transformation gives the expression

$$\lim_{\gamma l\to\infty} Z = \sqrt{\frac{d_1}{d_2 l^2}}\cdot\sqrt{\frac{\rho^*\rho_c}{1 + j\omega\varepsilon^*\varepsilon_0\rho_c}}. \tag{4.17}$$

If the bottom contact is epitaxial, it is safe to assume that its resistivity is frequency independent, and is a real number $\rho^* = \rho$. Now we can define a relaxation time, which is equal to $\tau_c = \varepsilon^*\varepsilon_0\rho_c$, and relaxation strength of the resistivity as the following: $\Delta\rho = \sqrt{\rho^*\rho_c}$. Therefore, complex impedance is equal to

$$\lim_{\substack{\omega\to 0 \\ \gamma l\to\infty}} Z = \sqrt{\frac{d_1}{d_2 l^2}} \cdot \frac{\Delta\rho}{(1+j\omega\tau_c)^{\frac{1}{2}}}. \tag{4.18}$$

From this limit, we get information about frequency dependence of complex impedance, i.e. the shape is the same as in the case of Cole-Davidson relaxation. It means that we are able to use equivalent circuit for investigating thin film system description, which consist of shunted resistor and capacitor:

$$Z = \frac{d_1}{l^2} \cdot \frac{\Delta\rho}{(1+j\omega\tau_c)^{\frac{1}{2}}}. \tag{4.19}$$

Next step is to find initial values of resistivity ($\rho_{c)}$ and dielectric permittivity (ε_c) of thin film based on the equivalent circuit description. These values will be used as known parameters during approximation with Eq. (4.8). After using Taylor expansion, complex impedance from Eq. (4.19) takes the following form in the case of low frequencies:

$$Z = \frac{d_1}{l^2} \cdot \Delta\rho \left(1 - \frac{1}{2} j\omega\tau_c\right). \tag{4.20}$$

If we take imaginary parts of Z from low frequency limit (Eq. 4.15) and equivalent circuit approximation (Eq. 4.20) and equate them, we will get the resistivity of the thin film:

$$-\mathrm{Im}Z = \frac{d_1}{l^2} \cdot \Delta\rho \frac{1}{2} \omega\tau_c = \frac{d_1}{l^2} \cdot \omega\tau_c\rho_c. \tag{4.21}$$

Then initial value of a resistivity of thin film should be equal to a half of relaxation strength:

$$\rho_c = \frac{1}{2}\Delta\rho. \tag{4.22}$$

Meanwhile, the initial value of a dielectric permittivity of thin film is following:

$$\varepsilon_c = \frac{\tau_c}{\varepsilon_0\rho_c}. \tag{4.23}$$

Lastly, it is important to evaluate a frequency from which the contact can be assumed as large. For this reason we rewrite an expression of propagation constant:

$$\gamma^2 = R'G' = \frac{j\omega\rho^*\varepsilon^*\varepsilon_0}{d_1 d_2}. \quad (4.24)$$

Here we claim that the resistivity of bottom electrode and dielectric permittivity of thin film are real numbers. So, propagation constant is a complex number, which has equal real and imaginary parts. Consequently, Eq. (4.16) can be rewritten as following

$$\gamma^2 = \frac{\omega\rho\varepsilon\varepsilon_0}{2d_1 d_2}. \quad (4.25)$$

Here, propagation constant can be expressed as $\gamma = \frac{N}{l}$, where N is a real number. Then frequency equation gets form

$$\omega = \frac{2d_1 d_2 N^2}{\rho\varepsilon\varepsilon_0 l^2}. \quad (4.26)$$

If we have a real system where the dimension of top electrode is $l = 10^{-3}$m, the thickness of thin film and bottom electrode are equal to $d_1 = 10^{-7}$m and $d_2 = 10^{-8}$m respectively, the resistivity of bottom electrode is $\rho = 10^{-3}\Omega \cdot$ m (e.g. LSMO), the dielectric permittivity of thin film is $\varepsilon = 10^3$ and we say that $N = 2$, then frequency approximately will be equal to $f = 100$ Hz. This means that large contact limit can be applied for experimental data above 100 Hz, which is in nearly all frequency range, which is usually available in an experiment.

4.1.1. Experimental assessment of electrical model of a thin dielectric film with a bottom electrode of negligible distributed resistance

In order to prove effectiveness of the theoretical model, we present experimental results of a measured thin film system approximated by equivalent circuit model, which mathematical expression is presented in Eq. 4.27 and the model of distributed contact (see Fig. 4.4).

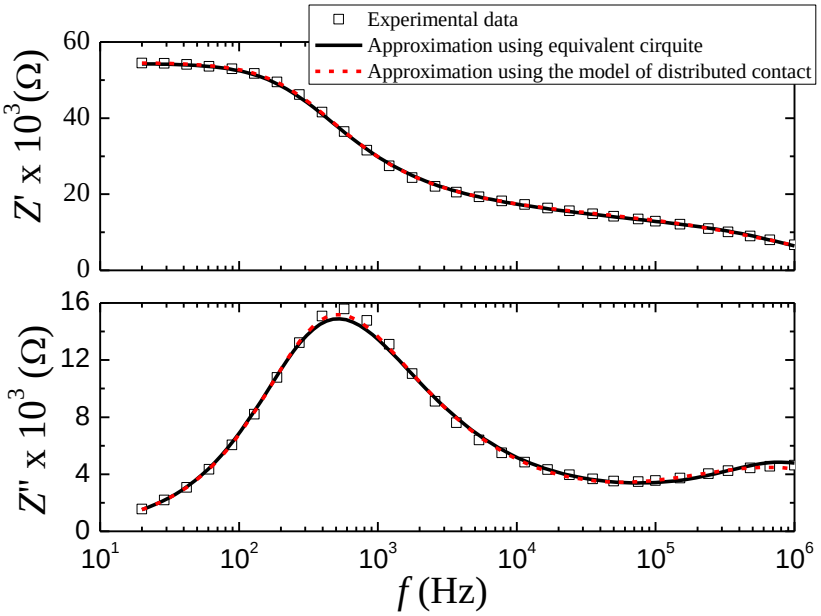

Fig. 4.4 Frequency dependence of the complex impedance of BST 70/30 thin film: solid line represents an approximation by equations of equivalent circuit, when all parameters are without restrictions; dashed line represents an approximation using the model of distributed contact.

The approximation by equivalent circuit method was made using the following expression:

$$Z^*(\omega) = Z(\infty) + \frac{\Delta Z_1}{(1 + (i\omega\tau_1)^{\alpha_1})^{\gamma}} + \frac{\Delta Z_2}{1 + (i\omega\tau_2)^{\alpha_2}}. \qquad (4.27)$$

Here all parameters are free, without any restrictions. Equation 4.27 consist of two parts: first one describes low frequency relaxation (from 20 Hz to 10^5 Hz) and second one, which is responsible for high frequency relaxation (from 10^5 Hz to 10^6 Hz). The differences between the two approximations are almost indistinguishable. The mismatches are caused by absence of full spectra registered at high frequencies. High frequency process is due to charge relaxation in the bottom electrode and it is not relevant in our investigations. For this reason, we can neglect these mismatches. Meanwhile, the low frequency relaxation describes relaxation in ferroelectric thin film and only these approximation parameters are used recalculating dielectric permittivity. Thus, if we try to recalculate and compare the dielectric permittivity from

equivalent circuit method and the model of distributed contact, we will get huge discrepancies between the values, which are shown in Fig. 4.5.

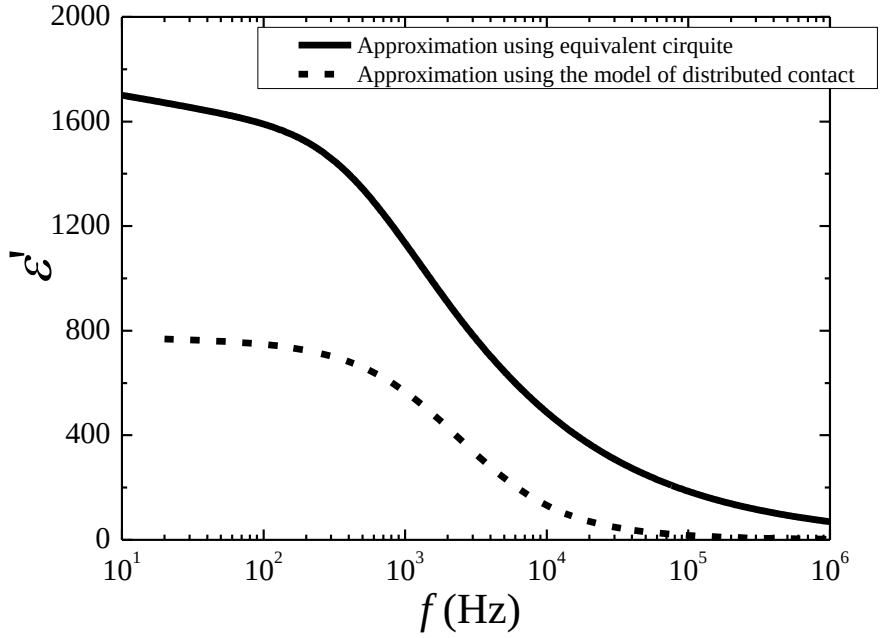

Fig. 4.5 Frequency dependence of the recalculated dielectric permittivity of BST 70/30 thin film using different approximation models: solid line represents the dielectric permittivity obtained from equivalent circuit and flat capacitor approximation, dashed line represents the dielectric permittivity obtained from the model of distributed contact.

The biggest differences are observed at low frequencies (from 20 Hz to 10^3 Hz). The value of dielectric permittivity varies more than twice in this frequency region. Moreover, equivalent circuit approximation fails at determination of the static permittivity, as in the limit of $\omega \to 0$ the dielectric permittivity from Eq. (4.27) diverges to infinity in the case when alpha and gamma are not equal to unity, while the proposed model does not suffer from the problem. However, the decrease of the dielectric permittivity at high frequencies (from 10^3 Hz to 10^6 Hz) is not corrected, and it is currently not known if this is an artefact.

It is very important to notice that depicted theoretical model has significant advantages, but also has some drawbacks. First of all the main advantage is that this theoretical model effectively describes electrical response (combined dielectric relaxation in the film and real conduction through the electrodes and film itself) of a fairly complicated heterostructure (BST/LSMO//LSAT). Unfortunately, the model of distributed electrode also has some disadvantages. This model is only valid if we use harmonic signals and is unusable for non-linear measurements. In the case of DC bias, the DC field will also become dependent on position. In the case of a tunable material this will also lead to a distribution of dielectric properties, which is not taken into account in the current model. Another potential problem is injection of charge carriers from the bottom electrode into the film. This injection is most likely to happen in the presence of the DC bias field, and can modify conductivity of the dielectric material. Despite these disadvantages, the model of a thin dielectric film with a bottom electrode of negligible distributed resistance was applied for epitaxial $Ba_{0.7}Sr_{0.3}TiO_3$ thin film. Experimental results will be discussed in the following chapter.

4.1.2. Summary

The model of a thin dielectric film with a bottom electrode of negligible distributed resistance was developed and verified for complicated thin film heterostructure (leaky functional layer, bad conduction of electrode layer, nontrivial properties at the heterointerfaces). The quasi one dimensional case was analysed, when system is infinite along *y* axis. Also, the effectiveness of characterized theoretical model was proved by approximation of experimental data. The model has several drawbacks, such as complexity, suitability for linear systems only, potential failure in presence of electric DC bias. Despite the disadvantages, the model describes the experimental data in a physically proper way, unlike equivalent circuit model. Furthermore, an algorithm to find static resistivity and dielectric permittivity of the film in a simple way was also proposed.

4.2. Barium strontium titanate thin films

Barium strontium titanate, $Ba_{1-x}Sr_xTiO_3$ (here referred to as BST) is well known and widely investigated material from the engineering point of view. Barium titanate $BaTiO_3$ (BTO in short) and strontium titanate $SrTiO_3$ (STO in short) gives a continuous solid solution: barium strontium titanate (BST) over the whole concentration range. Both, experimental reports and theoretical studies of the BST phase diagram of single crystals and ceramic were published in a number of papers [D.2-D.5]. It was shown that the temperatures of all three phase transitions of undoped barium titanate decrease linearly in the BST solid solution with increasing of the Sr content up to $0.2 < x < 0.25$.

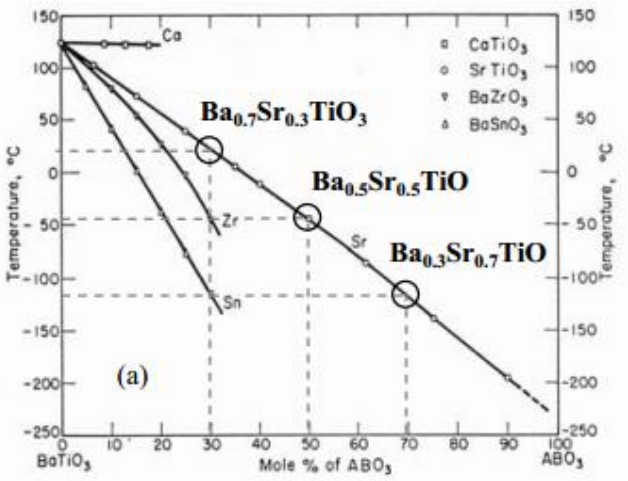

Fig. 4.6 Variation in Curie temperature of bulk BTO with various additives, adapted from [D.6].

In this solid solution region all phase transitions merge into one and the paraelectric–ferroelectric phase transition type transforms from the first order to the second order one [D.5]. As a result, the transition temperature (see Fig. 4.6) and hence the electrical and optical properties of BST ceramic can be tuned in a controllable way to get various functionalities for electronic and electromechanical applications.

In general, BST has a cubic perovskite structure, with the large barium and strontium ions occupying the corners of the unit cell as it is shown in Figure 4.7.The oxygen ions form an octahedral, which surrounds the small

central titanium atom. Therefore, barium strontium titanate has the chemical formula ABO_3, where Ba and Sr atoms occupy the A site, while Ti atoms occupy the B site. In the paraelectric phase, the high permittivity of the material derives from the fact that the titanium ion can be easily displaced by an applied field, determining a large induced dipole moment or polarization.

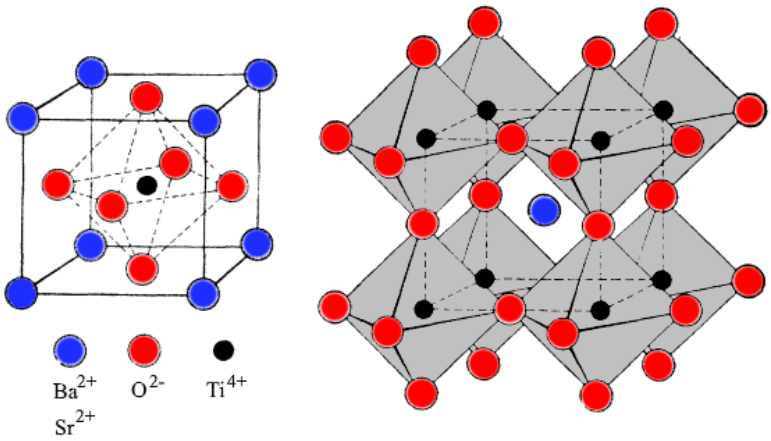

Fig. 4.7 Ideal perovskite structure of cubic BST showing oxygen octahedral surrounding the titanium ion, adapted from [D.7].

his effect is further enhanced by long range ordering effects at low temperatures. The displacement or polarizations begins to saturate at high fields, leading to a reduction in the small-signal effective dielectric constant. The dielectric response of roughly several thousand can be obtained with BST material [D.8, D.9]. In bulk materials, the dielectric constant is strongly temperature dependent, with a sharp peak at the Curie point. Meanwhile, thin films usually have a lower, less temperature dependent permittivity than bulk materials, as it is shown in Fig. 4.8. The lower permittivity in thin films might be related with small grain size. *Zhao et al.* [D.10] investigated grain size effect in BTO ceramics and it was seen that with decreasing grain size, the dielectric permittivity decreases and becomes more flatten.

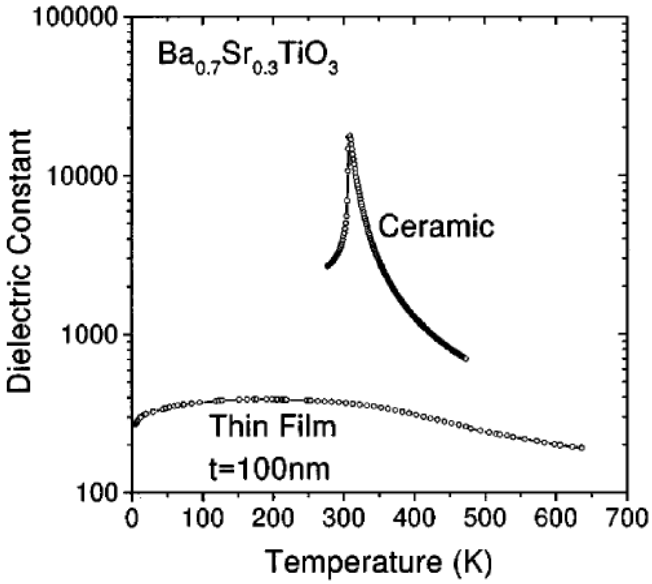

Fig. 4.8 Comparison of bulk and thin film BST material, adapted from [D.11]

Smaller temperature dependence of dielectric permittivity is desire, because of the fact that electronic components fabricated from these kinds of thin films are more likely to maintain their performance over a wide operating temperature range. In order to fulfil this requirement, electrical properties of thin film should be strictly controlled. One way is to control a phase transition temperature and this can be done by thin film strain engineering. Variation of phase transition temperature by different lattice mismatches is presented in Figure 4.9.

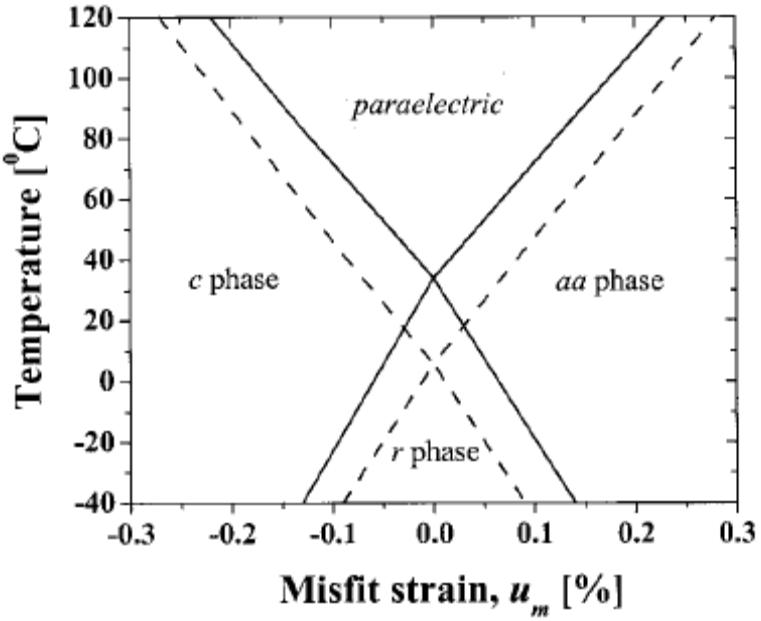

Fig. 4.9 Phase diagrams of (001) single-domain BST 70/30 (solid line) and BST 60/40 (dashed line) thin films epitaxially grown on the cubic substrate, adapted from [D.12].

Here, is shown that phase transition temperature can be varied with misfit strains. Another reason, why BST thin films are attractive for practical applications is the significant changes in the dielectric constant with applied electrical field. In the previous researches, *Padmini et al.* [D.13] showed that dielectric permittivity of BST 70/30 thin film might decrease by about 50 % if applied electric field is equal ~1 MV/cm.

Summing up, the changes in chemical composition gives one way to tailor phase transition temperature, but meanwhile lattice mismatches opens another way how phase transition temperature can be controlled. Therefore, this statement should be examined more in details. For this reason, the experimental results of complex impedance spectroscopy of barium strontium titanate thin films will be presented in the following chapter. Also, the influence of different electrode materials in film heterostructure will be discussed. Hence, $Ba_{0.7}Sr_{0.3}TiO_3$ (BST70/30) epitaxial thin films, which were deposited by pulsed laser deposition technique (PLD with a KrF excimer laser,

λ=248 nm) on (001) oriented low miscut (<0.1°) $SrTiO_3$ (STO) single crystalline commercially available substrates (CrysTec GmbH, Germany) were investigated. $La_{0.8}Sr_{0.2}MnO_3$ (LSMO) or $SrRuO_3$ (SRO) was used as a bottom electrode in the metal-insulator-metal structures. The substrates were etched in buffered HF (buffered oxide etchant) solution and annealed in O_2 flow according to the procedure described in the work of *Koster et al.* [D.14] to obtain a single site terminated and atomically smooth surface. Complex impedance measurements have been performed in frequency range from 20 Hz to 1MHz with HP4284 LCR meter and in temperature range from 300 K to 500 K. Measurements were performed during the cooling cycles down to 300 K at a rate of about 1 K/min. The model of distributed electrode was applied for the approximation of experimental results in the case of BST thin film with LSMO bottom electrode.

4.2.1. Complex impedance spectroscopy of $Ba_{0.7}Sr_{0.3}TiO_3$ / $La_{0.8}Sr_{0.2}MnO_3$ // $SrTiO_3$ heterostructures

Frequency dependence of the complex impedance of 76 nm thickness of $Ba_{0.7}Sr_{0.3}TiO_3$ / $La_{0.8}Sr_{0.2}MnO_3$ // $SrTiO_3$ (for short BST 70/30) epitaxial thin film is presented in Fig. 4.10. Solid lines represent a fit of the model of distributed electrode. Measuring frequency region can be divided into two regions: first is high frequency region (from 100 kHz to 1 MHz) and second is low frequency region (from 20 Hz to 100 kHz). The dispersion at low frequency region is related with processes observed in thin film; meanwhile, the dispersion observed at high frequencies is related with LSMO bottom electrode. This assumption might be approved according to experimental measurement results presented in Fig. 4.11, where added extern electric field decreases the values of complex impedance only at low frequencies. Fig. 4.10 shows that both dispersions are overlapped and the value of static impedance of high frequency dispersion is comparable with all measuring systems impedance. For this reason low and high frequency dispersions cannot be separated and special theoretical model should be applied in order to analyse experimental results. In consequences, the model of distributed bottom

electrode was applied in order to obtain temperature dependence of static dielectric permittivity. Obtained results will be presented in Fig. 4.10.

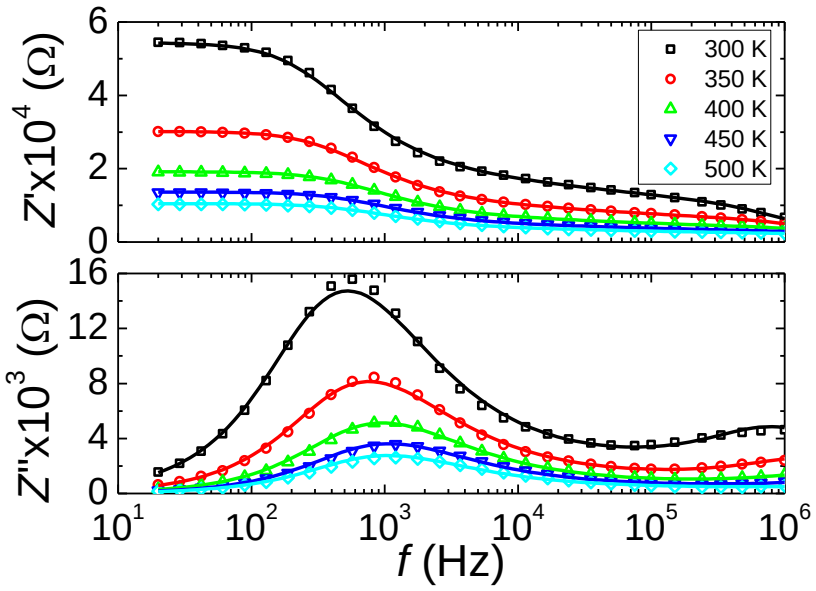

Fig. 4.10 Frequency dependence of the complex impedance of $Ba_{0.7}Sr_{0.3}TiO_3$ thin film. Solid line represents fits of the model of distributed electrode.

Frequency dependence of the complex impedance of $Ba_{0.7}Sr_{0.3}TiO_3$ thin film with and without added external electric field at room temperature is shown in Fig. 4.11. The decrease of complex impedance was observed only at low frequencies after adding external electric field which was equal approximately to E = 1 MV/cm. Hence, capacitive part of the impedance spectra is diminished (low frequency part in Fig. 4.11) and resistive (series combination of conductance through the bottom electrode and the BST 70/30 film) part is intact (high frequency part in Fig. 4.11).

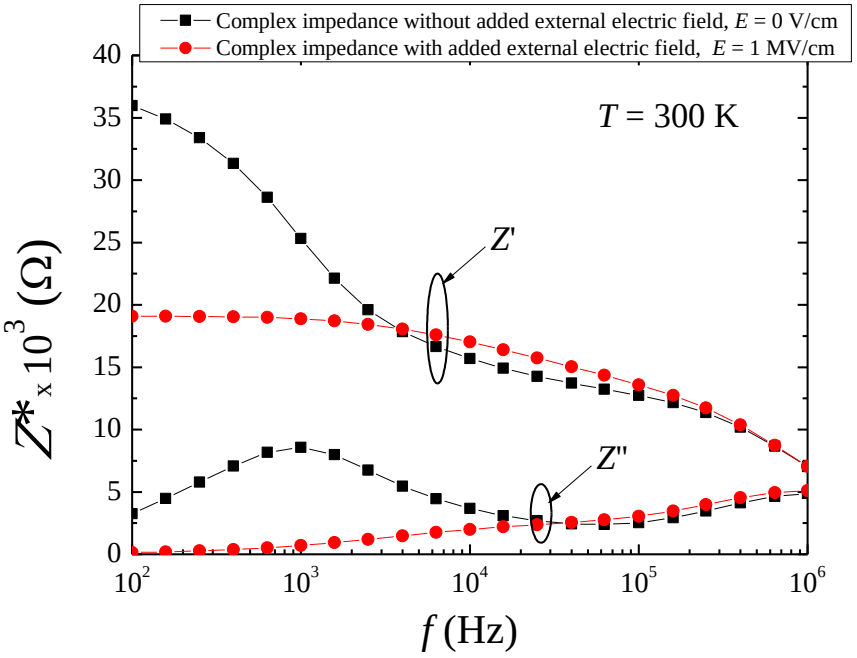

Fig. 4.11 Frequency dependence of the complex impedance of $Ba_{0.7}Sr_{0.3}TiO_3$ thin film with and without added external electric field.

Comparability of LSMO resistivity values with the resistivity values of all measuring system prevents a possibility to neglect high frequency dispersion during the approximation of experimental results. In other words, dispersion observed at high frequency range has to be evaluated during the approximation of the model of distributed electrode. With respect of previously mentioned limitation, the model of distributed electrode was applied and dielectric strength was calculated in a temperature range from 300 K to 500 K (see Fig. 4.12).

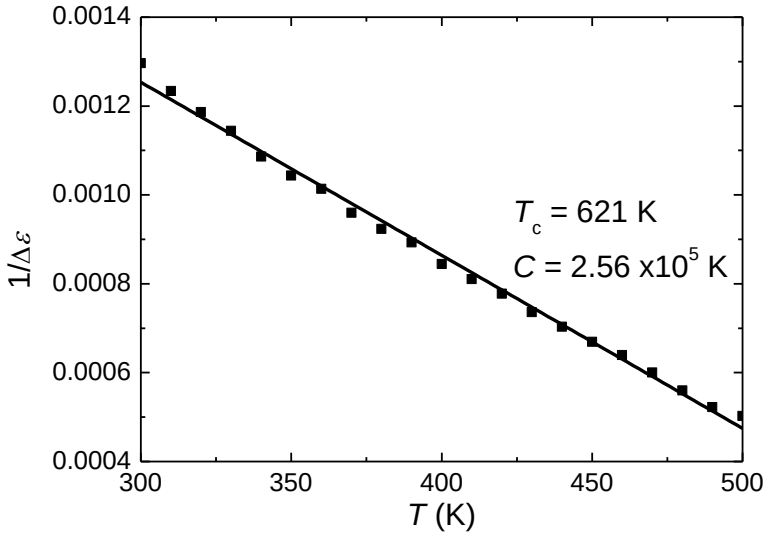

Fig. 4.12 Temperature dependence of the reciprocal dielectric strength of relaxation. Solid line is a fit of Curie-Weiss law.

The reciprocal dielectric strength was found to decrease with temperature and follows Curie –Weiss law, where Curie temperature is approximately equal to 620 K. The value of Curie temperature obtained after fitting procedure can be compared with the value shown in phase diagram of single domain BST 70/30 thin film epitaxially grown on the cubic substrate (see Fig. 4.9). In order to get theoretical prediction of phase temperature, in-plane and out-of-plane mechanical compression should be calculated. Bulk $Ba_{0.7}Sr_{0.3}TiO_3$ at room temperature is in ferroelectric phase and has a tetragonal crystal structure where the pseudocubic lattice parameter [D.15], at room temperature, is equal to a_b = 0.3965 nm which is used in phenomenological calculations of misfit strain [D.12] – temperature diagrams. From XRD reciprocal space mapping calculations [D.16], it was shown that BST 70/30 film in-plane lattice constant is around a_f = 0.391006 nm. Therefore, in-plane mechanical compression of BST 70/30 thin film at room temperature is ε (RT) = $(a_f - a_b)/a_b$ = -1.4 %. Meanwhile, BST 70/30 film out-of-plane lattice constant is around c_f = 0.40598 nm and out-of-plane mechanical compression of BST 70/30 thin film at room temperature is ε (RT) = $(c_f - a_b)/a_b$ = 2.4 %. Hence, from the

theoretical calculations performed by *Z.-G. Ban et al.* [D.12] ferroelectric phase transition temperature can be increased more than 300 K at -1.4 % negative strain and roughly is equal to T_c = 650 K, thus BST 70/30 at room temperature is in ferroelectric phase, what is confirmed by PFM experiments (*Bagdzevicius et al.* [D.16]). To sum up, experimentally obtained Curie temperature of $Ba_{0.7}Sr_{0.3}TiO_3$ / $La_{0.8}Sr_{0.2}MnO_3$ // $SrTiO_3$ heterostructure is in a good agreement with phase transition temperature theoretically predicted by *Z.-G. Ban et al.*

In order to show that BST 70/30 at room temperature is in ferroelectric phase, PFM studies of 76 nm BSTpc(001)/LSMOpc(001)//STOc(001) thin film at room temperature were presented by *Bagdzevicius et al*. [D.16]. Below the ferroelectric phase transition temperature BST 70/30 lattice experience additional spontaneous strain due to the lowering of crystal symmetry from cubic to tetragonal structure (in bulk). Meanwhile, BST 70/30 film possesses tetragonal symmetry even at film deposition temperature, which was 750 – 800 ºC, due to misfit strain and additional strain is relaxed forming a/c domain pattern below Curie temperature, as observed in PFM image (Fig. 4.13).

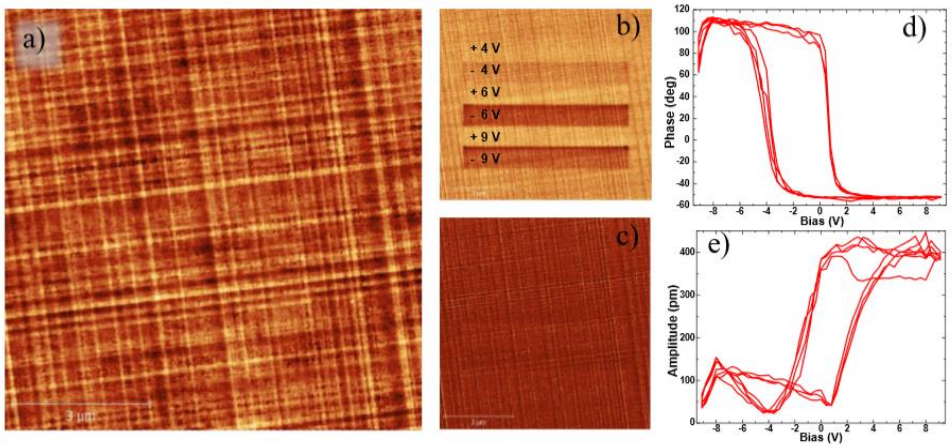

Fig. 4.13 PFM (dual AC resonance tracking mode – DART mode) images of strained 76 nm BST 70/30 thin film at room temperature: a) topography (0.8 nm height difference), b) PFM out of plane amplitude (80 pm amplitude difference) and c) PFM phase (15° difference) after poling experiment (up to 9V). Piezoelectric strain hysteresis loops d) phase and e) amplitude measured by PFM.

Therefore, built in electric field appeared as self-poling, in c-domains polarization pointing up (Fig. 4.13 b)) and asymmetric deflected piezoelectric hysteresis loops (Fig. 4.13 e)). PFM amplitude contrast in Fig. 4.13 b) is coming from electrostatic force due to charging effect of the film - electron injection from bottom electrode at high enough voltages.

Built in electric field is revealed also in macroscopic measurements – in the complex impedance analysis – as asymmetric tunability curves. Thus, calculated tunability of the strength of relaxation is shown in Fig. 4.14. Dielectric strength decreases more than 50 % at all temperatures after applied external voltage. The asymmetry of dielectric strength branches is determined by imprinted internal field. It can be seen that dielectric constant is not saturated at 1 MV/cm (20 V), and further decrease of the dielectric constant may be expected.

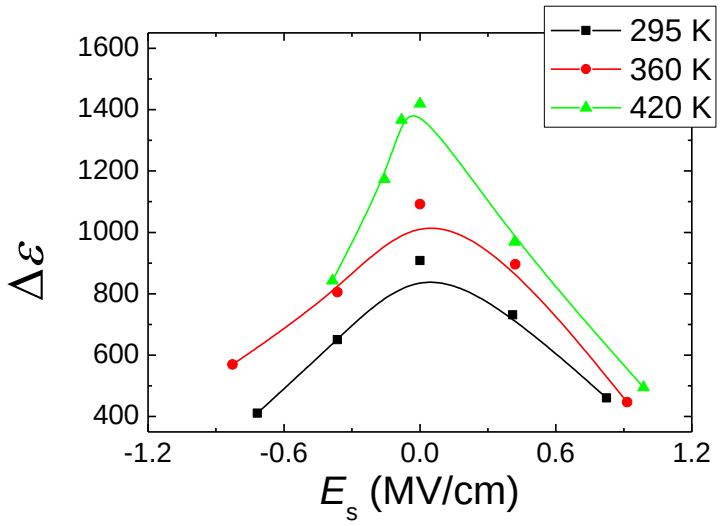

Fig. 4.14 Electric field tunability of the strength of relaxation. Dots – experimental points (taking into account the voltage drop at the bottom electrode), lines – approximation in the Landau-Ginsburg-Devonshire theory frame by the Johnson relation (see Eq. 3.20).

Tunability is comparable to other epitaxial thin films [D.13, D.17] deposited by physical vapour deposition (PVD) methods and the built in electrical field (approximately 88 kV/cm at RT and slightly decreases at

elevated temperature) and mechanical clamping (-1.4 % misfit strain at RT) are not detrimental for tunability. A bit lower overall dielectric permittivity can be the consequence of the flexoelectric effect caused by very inhomogeneous strains arising close to the 90° FE domain walls.

4.2.2. Complex impedance spectroscopy of $Ba_{0.7}Sr_{0.3}TiO_3$ / $SrRuO_3$ //$SrTiO_3$ heterostructure

Frequency dependences of complex specific resistance of $Ba_{0.7}Sr_{0.3}TiO_3$ / $SrRuO_3$ // $SrTiO_3$ heterostructure of two different thicknesses: 215 and 160 nm are presented in Fig. 4.15. A strong and only one dispersion of specific resistivity can be seen below ~10 kHz frequency for both samples.

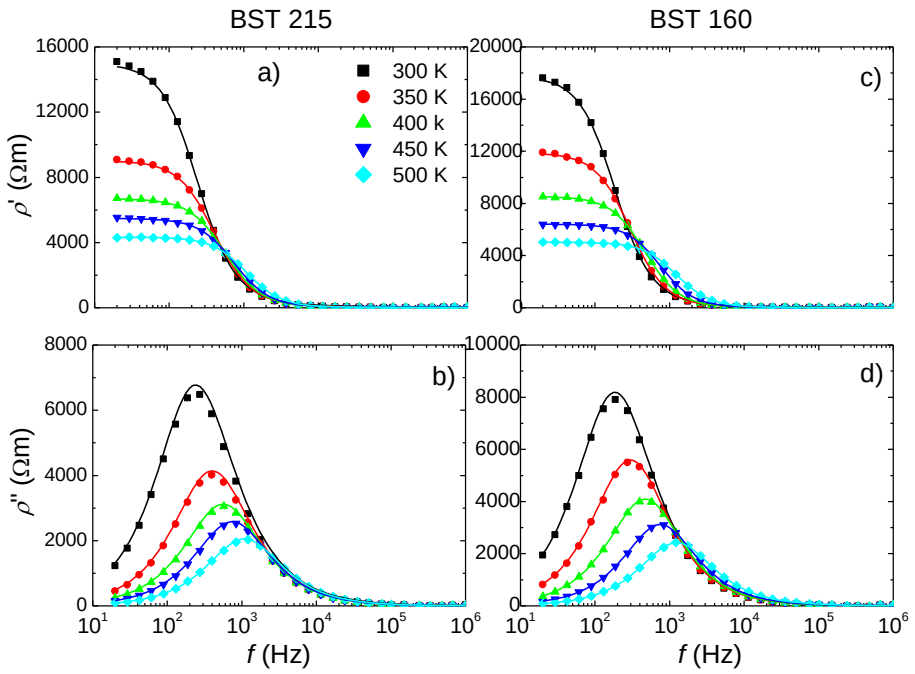

Fig. 4.15 a) and b) frequency dependence of the complex specific resistance of BST 70/30 215 thin film. c) and d) are frequency dependence of the complex specific resistance of BST 70/30 160 thin film. Solid line represents the fits of the Havriliak-Negami equation.

In consequence, the complex theoretical model of distributed bottom electrode becomes unnecessary during the analysis of experimental results. Here, in Fig.

4.15, on cooling the maximum of the imaginary part of ρ* moves toward lower frequencies indicating the thermally stimulated behaviour of this dispersion. In order to gain more information from this dispersion we fitted it to the Havriliak–Negami equation which generalises all relaxation-type dispersion relations:

$$\rho^* = \rho_\infty + \frac{\Delta\rho}{(1 + (j\omega\tau)^{1-\alpha})^\gamma}, \tag{4.28}$$

here: $\Delta\rho$ corresponds to the static specific resistivity, τ is the relaxation time of the process, α describes the spectral width, and γ is related to both the spectral width and asymmetry. ω is the angular frequency. During the data approximation it was found that α and γ parameters differ by less than 0.05 from 0 and 1, respectively. Thus, if one replaces these parameters in Eq. (4.28) by the respective constant values, we arrive at the situation where our system can be described as a single parallel RC circuit.

The values of dielectric permittivity, which were recalculated from the complex resistivity data, are presented in Fig. 4.16. Experimental investigations of the phase diagram of BST crystals [D.18], supported by theoretical calculations [D.19], have shown that the addition of Sr to $BaTiO_3$ leads to the decrease of temperatures of all three phase transitions and at 30 percent of strontium doping the ferroelectricity appears slightly below the room temperature. In the case of thin films, substrate-induced stress shifts the ferroelectric phase transition to higher temperatures when compared to the bulk material [D.12]. Indeed, in Fig. 4.16 the dielectric anomaly can be observed at somewhat higher (approx. 400 K) temperature but only at the highest frequencies. In other words, this dielectric anomaly temperature is between phase transition temperature in bulk materials (slightly below room temperature) and phase transition temperature induced by misfit strain in thin film (around 650 K). While it does not show the real peak of the dielectric permittivity at the phase transition point, it could be that this peak is blurred due to high electrical conductivity. As it is clearly seen from Fig. 4.16 b) and d), low frequency dielectric losses are really high and screens the dielectric

response. Another reason could be the weakening of the ferroelectric properties due to the size effect. In nanosized materials it is often the case [D.10]. It could be that in our films we have the superposition of both effects.

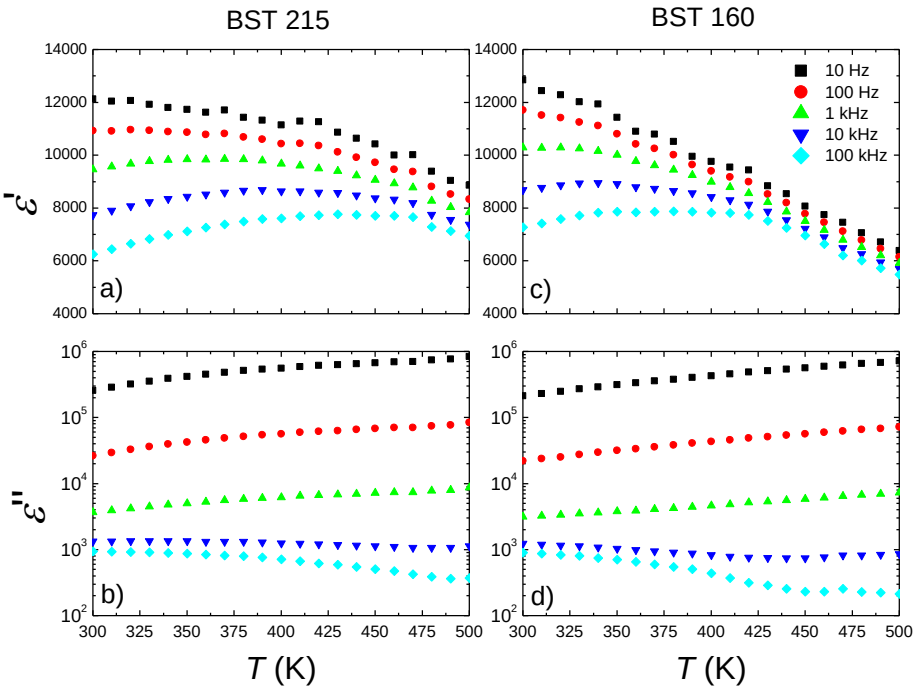

Fig. 4.16 a) and b) temperature dependence of the complex dielectric permittivity of BST 70/30 215 thin film. c) and d) temperature dependence of the complex dielectric permittivity of BST 70/30 160 thin film.

XRD patterns measured for 215 and 160 nm thick samples are presented in Fig. 4.17. STO, SRO and BST 70/30 peaks are clearly distinguishable and indexed in both heterostructures. Here, XRD experiments (coupled ω–2Θ and rocking curve – ω scans) were performed at room temperature with a Bruker D8 Discover high resolution diffractometer using a Ni filtered monochromatic Cu Kα radiation source. Therefore, in the both cases SRO and BST 70/30 layers were epitaxially deposited, evidenced by the STO having only <001> family diffraction peaks, and the corresponding SRO_{pc} and BST 70/30 showing only (00l) diffraction peaks.

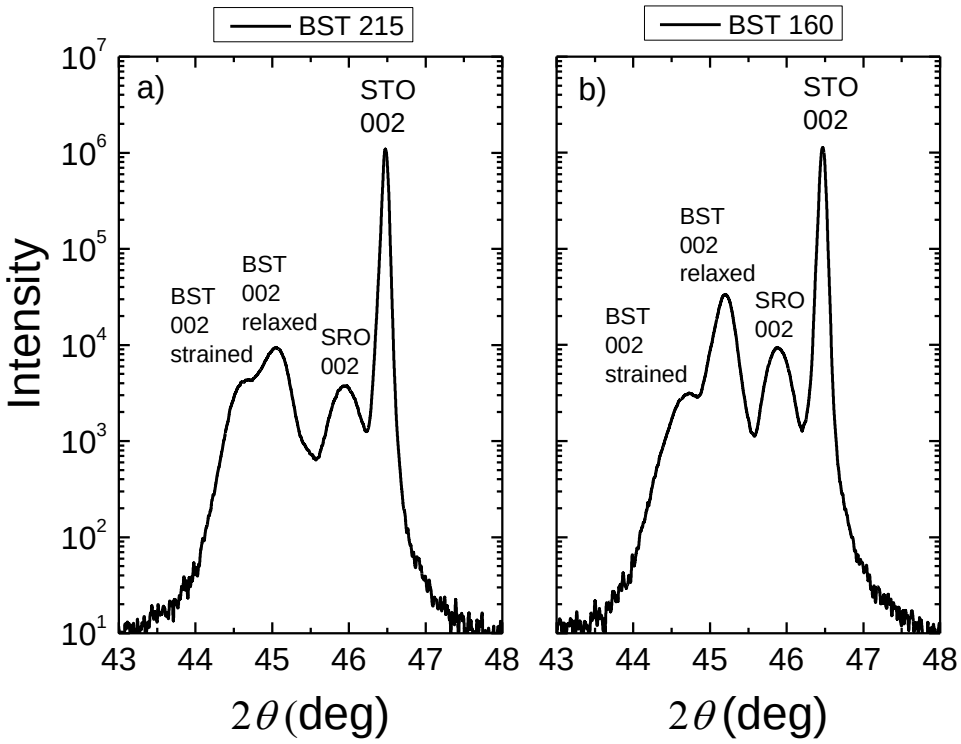

Fig. 4.17 X-ray diffraction (ω–2Θ scan) patterns of (a) 215 and (b) 160 nm films, adapted from.

It was indexed that SRO has pseudo cubic lattice symmetry – SRO_{pc}; this is usually a sufficient approximation when the SRO film is fully strained and serves only as an electrode, but not as a strain relaxation layer. No secondary phases or misoriented grains were observed by XRD (large angle scans are not shown here). Out-of-plane lattice parameters of BST 70/30 and SRO_{pc} were elongated due to the presence of epitaxial strain and clamping by the underneath STO lattice. For the SRO layer, the strain arises from mismatches of the lattice parameter and thermal expansion coefficient compared to the substrate. For the BST 70/30 layer, there was an additional strain component due to the ferroelectric phase transformation at T_c (ferroelectric phase transition from cubic/paraelectric to a tetragonal/ferroelectric phases in a bulk material), evidenced as formation of an a/c ferroelastic/ferroelectric domain pattern below T_c is presented by author [D.20, see Fig. 5].

In the 215 nm heterostructure, the BST 70/30 002 peak is split into a double peak at 44.63° and 45.06° (44.71° and 45.2° in BST 70/30 160 case). Such splitting can be related to the differently oriented *a* and *c* ferroelectric (and ferroelastic) domains (with different out of plane lattice parameters) or an accidentally formed BST 70/30 bilayer – two separated sublayers with different relaxation state and defect densities. The unavoidable strain relaxation in thick enough epilayers (thicker than critical thickness [D.21]) and probable formation of two sublayers, also observed by other researchers in similar BST/SRO//STO heterostructures [D.22], was chosen as the most probable scenario. No splitting of the BST 70/30 (002) peak was observed in thinner films even with a/c ferroelastic domain patterns (see Fig. 5 in [D.20]). The formation of two BST 70/30 sublayers is due to the change of the film growth mode, from a perfectly coherent (to substrate) lattice (probably step-flow mode) without any dislocations, to a less coherent one, with considerable strain relaxation (2D growth mode). Unfortunately, the transition between these two growth modes was not observed by RHEED, most likely due to fast roughening of the film surface and transition to the 3D (island) mode (also observed in [D.22]).

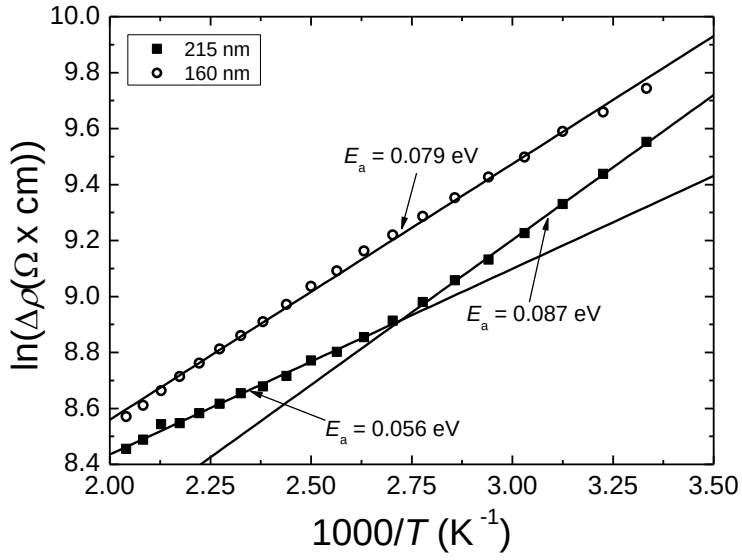

Fig. 4.18 Reciprocal temperature dependence of the static specific resistivity of thin BST 70/30 films.

In the 160 nm film, the diffraction intensity of the relaxed part is much higher than that of the strained part (absolute intensity differs more than 10 times). The intensity must be proportional to the volume. This indicates that almost all thin film is relaxed. On the other hand, the thicker film has two distinct regions with different strain, which give similar diffraction intensity and, correspondingly, volume. Unequal volume fractions of strained and relaxed sublayers (in different thickness BST 70/30 films) are confirmed by reciprocal temperature dependences of the static specific resistivity, which are plotted in Fig. 4.18. These graphs show the Arrhenius-type behaviour, therefore the experimental data was fitted to Eq. (4.29) (solid lines in the figure):

$$\Delta\rho = \rho_0 e^{E_a/kT}, \tag{4.29}$$

here: ρ_0 is the specific resistivity at infinite temperature, E_a is the activation energy, and T is the temperature.

It was found that the 160 nm thick film has a single section with activation energy of 0.079 eV. Meanwhile, the 215 nm thick film has two regions with different activation energies: 0.056 above and 0.087 eV below the 370 K temperature. This can be explained by the (non-) uniform strain of the films. Below the model for result explanation will be proposed.

Let us assume that a thin film consists of a bottom electrode, a top electrode and two functional layers (strained and relaxed) as shown in Fig. 4.19.

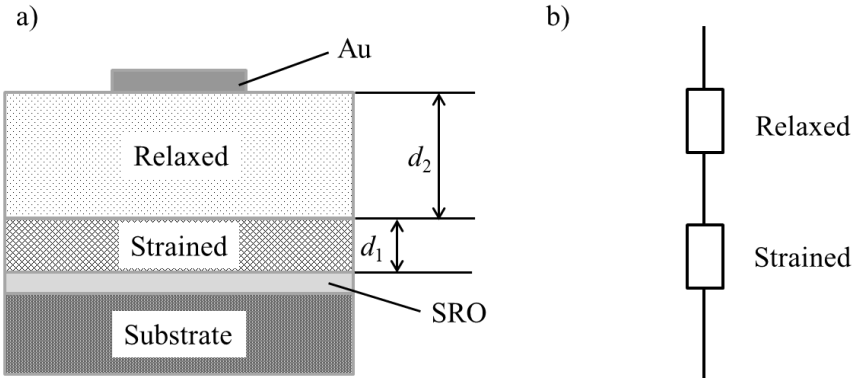

Fig. 4.19 Schematic illustration of a double layered thin film (a) and its equivalent circuit (b).

In the case of the 215 nm film the two layers are of roughly the same thickness, while in the other case one of the layers (the relaxed one) is much thicker than the other. For example, in the case of the 215 nm film, layer thicknesses can be assumed to be roughly equal to $d_1 = d_2 = 100$, and in the case of 160 nm film, $d_1 = 10$ and $d_2 = 150$ nm. We can rewrite the Arrhenius law for electrical resistance of each functional layer:

$$\begin{aligned} R_{strained} &= \rho_1 \cdot \frac{d_1}{S} \cdot e^{\left(\frac{E_1}{kT}\right)}, \\ R_{strained} &= \rho_2 \cdot \frac{d_2}{S} \cdot e^{\left(\frac{E_2}{kT}\right)}, \end{aligned} \tag{4.30}$$

here: S is the area of the top electrode.

The total sample resistance is equal to a sum of the resistances of the strained and relaxed functional layers, as it is equivalent to the series connection of the layers (Fig. 4.19 b)):

$$R = R_{strained} + R_{relaxed}. \tag{4.31}$$

In such a case, the biggest resistance will dominate the total resistance, and the experimentally observed value of the activation energy will be determined by the activation energy of the dominating resistance. A schematic illustration of the reciprocal temperature dependence of the total electrical resistance of double layered thin films is presented in Fig. 4.20.

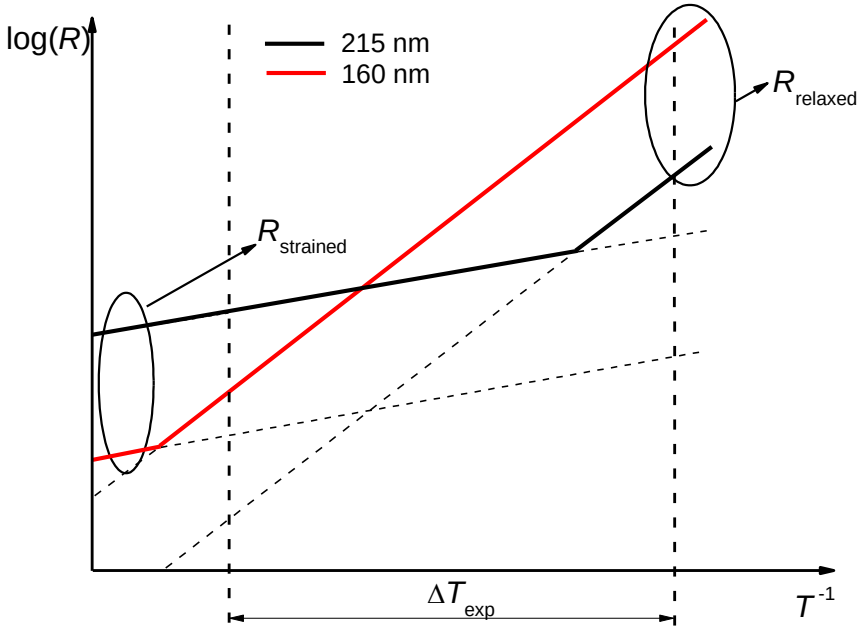

Fig. 4.20 Schematic illustration of reciprocal temperature dependence of electrical resistance of double layered thin films. Solid lines (red and black online) represent the total resistance of the sample, while short-dashed lines are resistances of the uniform layers.

Here, vertical black dashed lines show an experimental temperature range. Red and black solid lines represent the total resistance of the films with 160 and 215 nm thicknesses, respectively. This illustration indicates that both samples exhibit the same behaviour. In the case of the 160 nm film, the resistance of the strained layer dominates at much higher temperatures than in the case of the 215 nm sample, thus the change of activation energy is visible only in the latter case.

This model allows us to associate the activation energies with strain in the layers. It is possible due to the fact that both samples are fabricated with the same deposition parameters except the deposition time, which was needed to alter the total thickness. Thus, the nature of defects (and the source of electrons or holes) in the samples can be expected to be the same.

The dependence of activation energy on strain in thin BST 70/30 films was calculated according to the relation $(c_f–c_b)/c_f$ where c_f and c_b are the out-of-plane lattice constants of the film and bulk material, respectively. The lattice constants for our films have been obtained from X-ray measurements and cb was taken from the literature [D.23]. The results of the calculations are presented in Table 1.

Table 1. Dependence of the activation energy on the out of-plane strain in thin BST 70/30 films of various thicknesses.

Film thickness	Strain, %		Activation energy, meV	
	Strained	Relaxed	Strained	Relaxed
160 nm	1.38	0.33	-	79±0.9
215 nm	1.56	0.65	56±1.1	87±1.2

As we can see from Table 1, the activation energies of relaxed layers in different films are different. The BST 70/30 layers were deposited at the same PLD conditions but at different strain state at deposition temperature. The strain state depends on the density of dislocations at deposition temperature. The latter depends on the thickness of the layer [D.24], which was varied. As a result, different concentration of defects (dopants) in different samples was obtained even though the deposition conditions were the same, as evident from different activation energies for the relaxed layers. However, the activation energy of the specific resistivity is inversely proportional to the strain of the film if all other parameters (i. e. dopant concentration) are the same. This is easily realised in the case of physically the same film, which is in BST 70/30 215. Furthermore, the concentration of possible structural defects is smaller in the strained layers, since relaxation is realised by defects, i. e. displacement of ions. This means that higher activation energy in the case of a relaxed layer can only be related to strain. Keeping in mind the low values of E_a, the conductivity must be coming from some easily ionised defects, which are the source of either electrons or holes. However, the activation energy of the resistivity depends on the ionisation energy of the defects (which is unlikely to change as drastically with strain) as well as the activation energy

of the electron/hole mobility. Furthermore, the induced strain must be creating an anisotropic environment around the defects. This would lead to anisotropic mobility of the charge carriers. As the investigated films are epitaxial and the resistivity was measured in the out-of-plane geometry, this means that the positive out-of-plane strain lowers the activation energy of mobility, leading to the decrease in the activation energy of specific resistivity.

4.2.3. Summary

Experimental investigations of $Ba_{0.7}Sr_{0.3}TiO_3$ / $La_{0.8}Sr_{0.2}MnO_3$ // $SrTiO_3$ and $Ba_{0.7}Sr_{0.3}TiO_3$ / $SrRuO_3$ // $SrTiO_3$ epitaxial thin films were presented. First of all, it was found that the choice of conductive layer plays a significant role during the analysis of experimental results. Consequently, complex impedance of measuring system is strongly influenced by bad conductivity of electrode layer (LSMO layer) resulting the appearance of impedance dispersion at high frequencies (from 100 kHz to 1 MHz), which cannot be neglected. For this reason, additional effort should be put in order to analyse experimental results. Meanwhile, in the case of heterostructure, where SRO electrode layer is used, high frequency dispersion is not observed resulting less complicated analysing algorithm of experimental results.

Secondly, the built in electrical and strain fields influence on functional BST 70/30 properties (dielectric permittivity and tunability) was investigated. There was experimentally confirmed the enhancement of ferroelectric phase transition temperature T_c in $Ba_{0.7}Sr_{0.3}TiO_3$ / $La_{0.8}Sr_{0.2}MnO_3$ // $SrTiO_3$ thin films with negative -1.4 % compressive strain. Impedance analysis allowed to conclude that Curie temperature is enhanced more than 300 K ($T_c \approx 620$ K) and it matches theoretical calculations. Nevertheless I have showed that built in 88 kV/cm electric and -1.4 % misfit strain fields does not deteriorate dielectric tunability (observed tunability was more than 50 % at all temperatures). Meanwhile, in the case of $Ba_{0.7}Sr_{0.3}TiO_3$ / $SrRuO_3$ // $SrTiO_3$ dielectric anomaly is observed around 400 K and only at high frequencies. Therefore, it does not show the real peak of the dielectric permittivity at the phase transition point.

To sum up, it was observed that increasing misfit strain of epitaxial thin film, phase transition temperature can be controlled.

Thirdly, after analysis of $Ba_{0.7}Sr_{0.3}TiO_3$ / $SrRuO_3$ // $SrTiO_3$ epitaxial thin films it was observed that the films consist of two BST 70/30 sub-layers, one of them fully strained by the substrate and the other relaxed. These layers have different activation energies of the specific resistivity. A model was proposed to explain the experimental results, which points to an important conclusion – the positive out-of-plain strain lowers the activation energy of the mobility of electrons (or holes) in the investigated films.

Lastly, after investigation of BST 70/30 epitaxial thin film, it was observed that the curves of dielectric permittivity are flattening and the values are much lower than in the case of bulk BST 70/30 materials. The behaviour of dielectric permittivity of BST 70/30 thin films can be explained in two ways: low frequency dielectric losses are really high and screen completely the dielectric response or because of the weakening of the ferroelectric properties due to the size effect. Most probably in our films we have the superposition of both effects.

4.3. Lead magnesium niobate – lead titanate single crystals and thin films

In the recent years, lead magnesium niobate – lead titanate, (1-x)$Pb(Mg_{1/3}Nb_{2/3})O_3$ – x$PbTiO_3$ solid solution (here referred to as PMN-PT) was widely investigated because as an alternative to $PbZr_{1-x}Ti_xO_3$ (PZT) solid solution. Different compositions of the PMN-PT present various physical properties. Undoped $Pb(Mg_{1/3}Nb_{2/3})O_3$ is a typical relaxor ferroelectric which is characterized by a diffuse maximum of the dielectric constant associated with significant frequency dispersion [D.25]. PMN exhibits a non-polar paraelectric phase at high temperature, which is similar in many aspects to the paraelectric phase of normal ferroelectrics. After cooling, a transformation occurs from the paraelectric phase to the ergodic relaxor state, characterized by the presence of polar nanoregions randomly distributed by the specimen. This transformation which occurs at the so-called Burns temperature (T_B) cannot be considered as structural phase transition, because it is not caused by any change of crystal structure on the macroscopic or mesoscopic scale. On the other hand, $PbTiO_3$ shows a typical ferroelectric-paraelectric phase transition with a high Curie temperature [D.26]. Thus, ferroelectric relaxor PMN-PT is a solid solution between a relaxor (PMN) and a ferroelectric (PT) material. In this system, with the increase in PT content, T_C increases and relaxor behaviour decreases and between 0.7PMN-0.3PT to 0.5PMN-0.5PT compositions, there exists a morphotropic phase boundary (MPB) which is associated with abnormally high dielectric response and giant electromechanical properties (see Fig. 4.21).

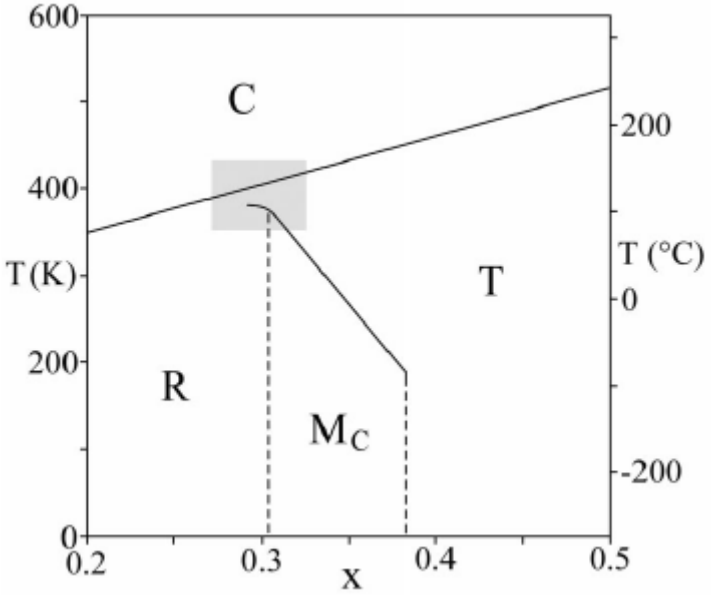

Fig. 4.21 Temperature – composition phase diagram of (1-x)PMN–xPT, adapted from [D.27].

The nature of the MPB is still debated in the literature, but a consensus seems to emerge as to the existence of a sequence of phase transitions (second order transitions) that accommodate the rhombohedral to the tetragonal transition, thus allowing for easy rotation of the polarization vector [D.28].

PMN-PT, the same as BST, has ABO_3–type structure (see Fig. 4.7), but here Mg^{2+}, Nb^{5+} and Ti^{4+} ions randomly occupy the oxygen octahedral centre, while the A site is occupied by the Pb^{2+} ion. The pyroelectric and dielectric properties of 0.71PMN-0.29PT single crystals have not yet been investigated in a broad temperature and frequency ranges. Pyroelectric coefficients has been measured for (1–x)PMN-xPT (x = 0.28, 0.33) single crystals [D.29] and (1–x)PMN-xPT (x = 0.30, 0.32, 0.34) ceramics [D.30]. Dielectric properties of PMN-PT single crystal with different concentrations were investigated at various temperature ranges. More detailed information can be found in ref. [D.31, D.32]. Also, there are several reports presented in the field of electrical properties of PMN-PT thin films. *Wasa et al.* studied properties of sputtered and single c-domain/single crystal 0.67PMN-0.33PT thin films [D.33-D.35]. He showed that sputtered 0.67PMN-0.33PT films exhibit the fully relaxed

structure above the critical film thickness, which is around 300 nm. Also, at thicknesses bellow 50 nm thin film is fully strained. Meanwhile, at the transition region, which is in between, thin film showed the antiphase domain structure[2]. Relaxed 0.67PMN-0.33PT thin films were used for the evaluation of the dielectric and ferroelectric properties in order to reduce the effect of the strain on their properties. The relaxed 0.67PMN-0.33PT thin films showed that the low voltage dielectric permittivity at room temperature was 1500 to 4000. A broad temperature anomaly was observed at T_c= 80 ˚C. The sputtered PMNT thin films showed P-E hysteresis curve at the temperature below 200 ˚C.

$0.71Pb(Mg_{1/3}Nb_{2/3})O_3$-$0.29PbTiO_3$ (0.71PMN-0.29PT) single crystals oriented along three different crystallographic directions, <001>, <011> and <111> were supplied by H.C. Materials Corporation (USA). All crystals were acquired in the form of 10 x 10 x 0.5 mm^3 plates and four roughly equal-sized samples (of nominal area 5 x 5 mm^2) were cut from it. These samples were coated with indium tin oxide (ITO) and silver paste to ensure a good electric contact. The plates of 0.71PMN-0.29PT single crystals were poled with poling field applied along the [001], [011] and [111] directions at room temperature. The poling fields were equal to 2, 3.2 and 1.6 kV/cm for the <001>, <011> and <111>-oriented crystals, respectively.

Epitaxial $0.67Pb(Mg_{1/3}Nb_{2/3})O_3$-$0.33PbTiO_3$ (0.67PMN-0.33PT) thin film of 500 nm thickness was deposited by pulsed laser deposition technique (PLD) using a KrF excimer laser (λ = 248 nm) on (001) oriented $SrTiO_3$ substrate. $SrRuO_3$ (SRO) was used as base and top electrodes with thickness equal to 100 nm. More detailed deposition conditions of 0.67PMN-0.33PT functional layer and SRO electrodes are reported elsewhere [D.37, D.38].

An HP4284 precision LCR-meter was used for dielectric and complex impedance measurements were performed at temperature range from 300 K to 500 K during the heating and cooling cycles and only during cooling cycle at rates of about 1 K/min, in the cases of 0.71PMN-0.29PT single crystals and

[2] Antiphase domains are forming a structure, where atoms are displaced by ½[±1 ±1 0]. The schematic illustration (Fig. 2 b) is provided in ref. [**Error! Reference source not found.**]

thin film, respectively. Measuring frequency range was from 20 Hz to 1 MHz. Ferroelectric hysteresis loops and electric field tunability of real and imaginary parts of dielectric permittivity of 0.67PMN-0.33PT thin film were measured in the 300 – 450 K temperature range and at a frequency of 1kHz. Measurements were performed using a TF Analyser 2000 (aixACCT) ferro- and piezoelectric thin film analysis system. Also, pyroelectric response of each 0.71PMN-0.29PT single crystal samples was measured with the same test system TF Analyser 2000 (aixACCT) at temperatures from 220 K to 420 K. While changing the temperature the current flow through the sample was recorded. The pyroelectric coefficient was calculated taking into account the following formula:

$$p \approx \frac{1}{A}\frac{I\Delta t}{\Delta T}, \tag{4.32}$$

where: I is the pyroelectric current, A is the area of the electrodes and $\frac{\Delta T}{\Delta t}$ is the rate of change of temperature.

4.3.1. Dielectric and pyroelectric investigation of $0.71Pb(Mg_{1/3}Nb_{2/3})O_3$-$0.29PbTiO_3$ single crystals

Temperature dependences of the real and imaginary parts of dielectric permittivity of $0.71Pb(Mg_{1/3}Nb_{2/3})O_3$-$0.29PbTiO_3$ (in short, 0.71PMN-0.29PT) single crystal oriented and poled along three different crystallographic directions, <001>, <011> and <111>, during the heating and cooling cycles are shown in Fig. 4.22, 4.23 and 4.24 (square dots and solid lines, respectively).

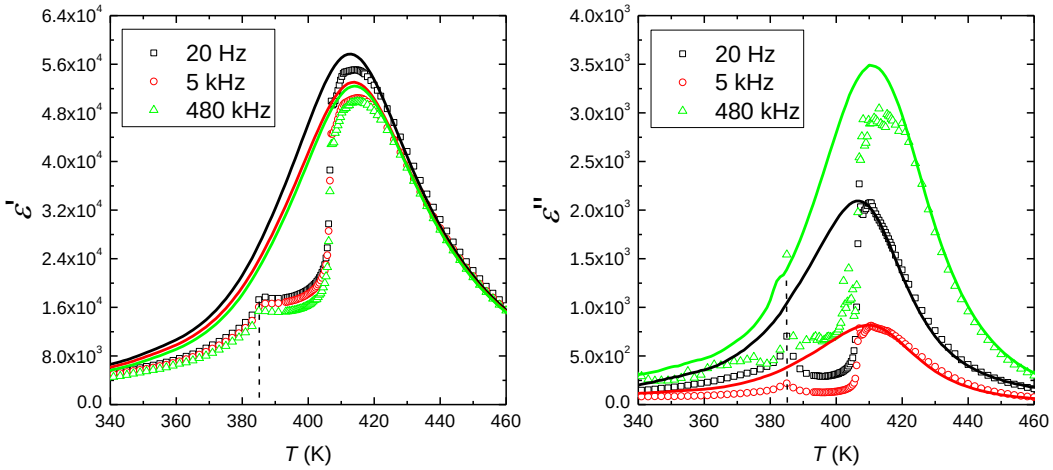

Fig. 4.22 Temperature dependences of the real and imaginary parts of dielectric permittivity of the <111>-oriented 0.71PMN-0.29PT single crystal measured in the 20 Hz – 480 kHz frequency range during the heating (square dots) and cooling (solid lines) cycles.

During the heating cycle, the 0.71PMN-0.29PT crystal oriented along <111> crystallographic direction shows a dielectric constant maximum at $T_c \approx 410$ K that denotes the Curie temperature for the tetragonal to cubic (T-C) phase transitions (see Fig. 4.22 square dots). A second anomaly is clearly observed around T = 380 K, while heating from room temperature. This anomaly is ascribed to the rhombohedral-tetragonal (R-T) phase transition [D.39]. Quite different situation is seen during the cooling cycle as only one transition from cubic to rhombohedral phase is observed around 410 K temperature (see Fig. 4.22 solid lines). The dielectric measurements were repeated several times, even with unpoled samples and the dielectric responses were indistinguishable from initially poled samples. The difference between heating and cooling cycles could be interpreted as follows. During the heating cycle direct transition from rhombohedral to cubic phase involves large structural changes that are energetically not favourable, i.e. an intermediate phase or several phases are required [D.40]. While during cooling cycle, the metastable phase is not detected, because the change of temperature is too fast.

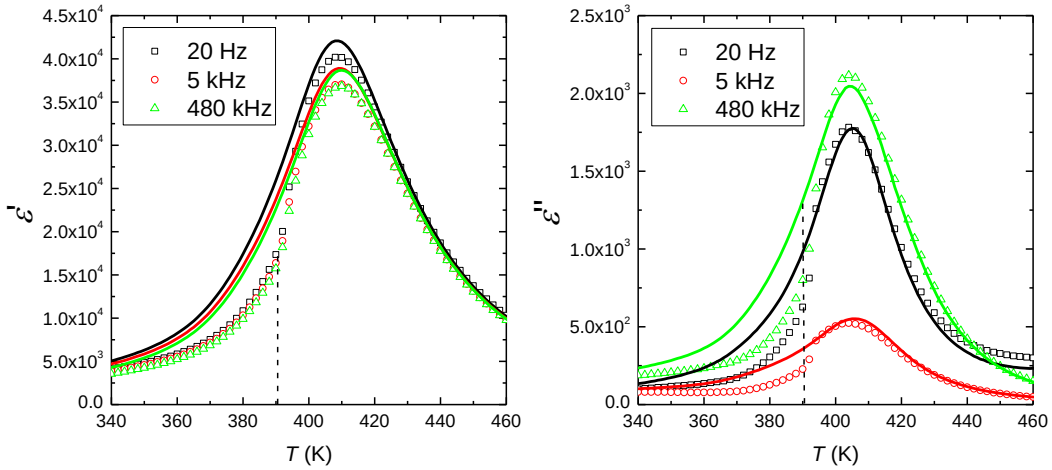

Fig. 4.23 Temperature dependences of the real and imaginary parts of dielectric permittivity of the <011>-oriented 0.71PMN-0.29PT single crystal measured in the 20 Hz – 480 kHz frequency range during the heating (square dots) and cooling (solid lines) cycles.

Figure 4.23 shows the dielectric behaviour of the <011>-oriented 0.71PMN-0.29PT single crystal as a function of temperature at different frequencies. During the heating cycle, the dielectric constant shows only one broad maximum at $T_C \approx 410$ K, which is related to the T-C phase transition, as in the case of <111>-oriented 0.71PMN-0.29PT single crystal. On the other hand, below the Curie temperature, a dielectric loss shoulder is detected around 390 K temperature, which is associated with R-T phase transition (see Fig. 4.23 square dots). During the cooling cycle, the same situation is observed for the <111>-oriented single crystal: only one anomaly is detected.

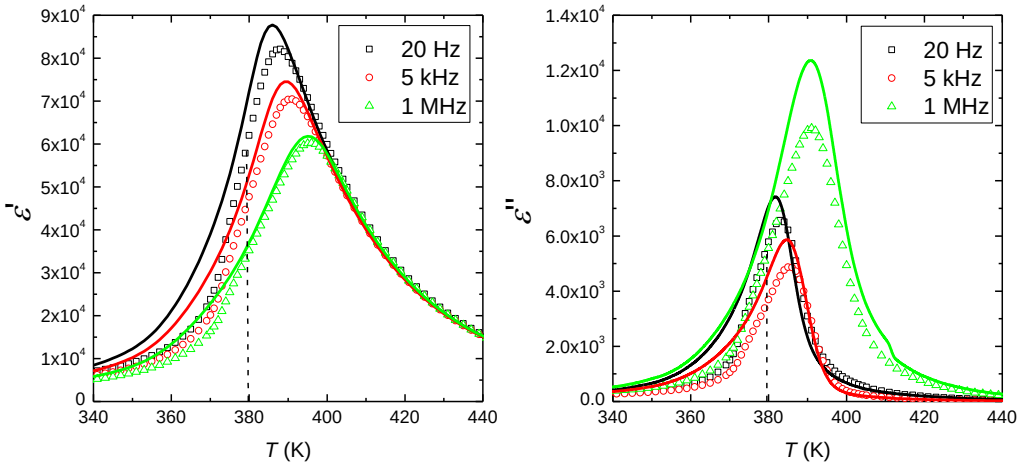

Fig. 4.24 Temperature dependences of the real and imaginary parts of dielectric permittivity of the <001>-oriented 0.71PMN-0.29PT single crystal measured in the 20 Hz – 480 kHz frequency range during the heating (square dots) and cooling (solid lines) cycles.

Meanwhile, the temperature dependences of the real and imaginary parts of dielectric permittivity of the <001>-oriented 0.71PMN-0.29PT single crystal is presented in Fig. 4.24. The behaviour of phase transitions is the same as in the cases of <111> and <011>-oriented crystals during the heating and cooling cycles. However, we clearly see that the dielectric dispersion is observed below Curie point ($T < T_C$), which could be related to domain wall dynamics [D.41, see Fig. 2]. In our case, it is clearly observed, that domain walls gives additional contribution to the total dielectric permittivity i.e. dielectric permittivity value increases almost two times at maximum position.

Experimental results of the pyroelectric coefficients of the 0.71PMN-0.29PT single crystal oriented along three different crystallographic directions, <001>, <011> and <111> are shown in Fig 4.25.

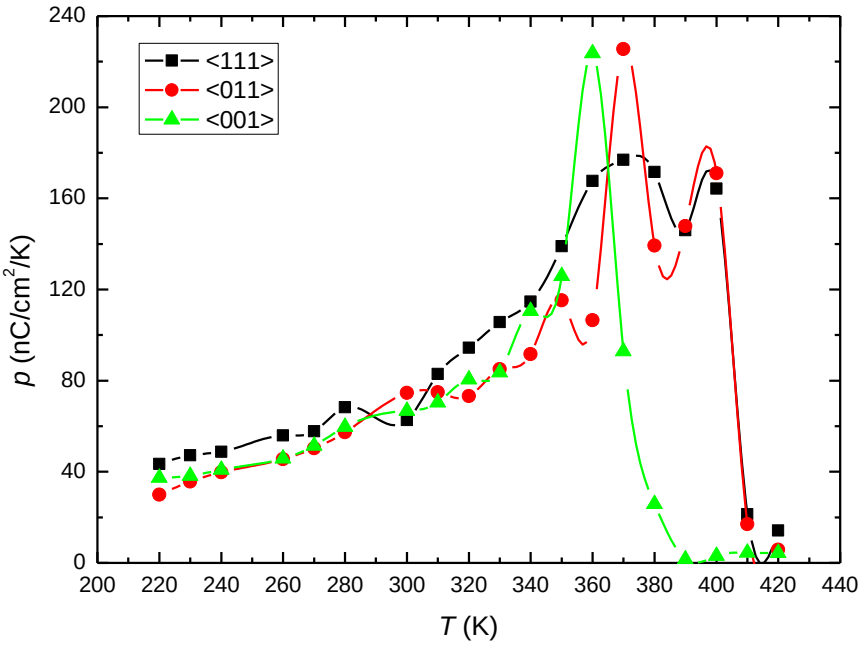

Fig. 4.25 Temperature dependence of the pyroelectric coefficients of the 0.71PMN-0.29PT single crystal oriented along three different crystallographic directions, <001>, <011> and <111>. Solid lines represent the connection of experimental points.

The value of pyroelectric coefficient is practically temperature-independent up to room temperature (300 K) and is found to be ~50 nC/cm^2/K for the 0.71PMN-0.29PT single crystal oriented along the <111> direction and ~40 nC/cm^2/K for the <011> and <001>-oriented crystals. At room temperature the values of *p* are equal to 63 nC/cm^2/K, 75 nC/cm^2/K and 67 nC/cm^2/K for the <111>, <011> and <001>-oriented single crystals, respectively. These values are comparable to those reported earlier on the 0.72PMN-0.28PT single crystals [D.29]. The variations of pyroelectric coefficients with temperature show two maxima, one at 370 K and another at 400 K for the crystals oriented along the <111> and <011> directions, respectively, while for the <001>-oriented crystal, only one maximum is observed at 360 K. The maximum values of *p* are equal to 176, 225 and 223 nC/cm^2/K at 370 K and 360 K for crystals oriented along the <111>, <011> and <001> directions and 164 and

170 nC/cm^2/K at 400 K for the <111> and <011>-oriented crystals, respectively. The T_c values obtained by pyroelectric measurements are in a good agreement with the values obtained from the dielectric measurements. The behaviour of pyroelectric coefficient of the 0.71PMN-0.29PT single crystal oriented along the <001> direction needs a deeper discussion. The <001> crystal direction actually represents a set of directions: [001], [010] and [100]. Polarization component in the tetragonal phase is perpendicular to the sample's surface in the 0.71PMN-0.29PT single crystal oriented along the <111> and <011> crystallographic directions. Therefore, the pyroelectric response is observed for the given directions. On the other hand, the <001> crystal direction actually represents a set of directions: [001], [010] and [100] and the polarization component in the tetragonal phase can be either perpendicular or parallel to the sample's surface. In our case, the dipolar moment lies in the sample plane and it is perpendicular to the external electric field. As a result, the pyroelectric response is not observed.

4.3.2. Impedance spectroscopy of $0.67Pb(Mg_{1/3}Nb_{2/3})O_3$-$0.33PbTiO_3$ thin films

The frequency dependencies of the real and imaginary parts of the specific impedance of the $0.67Pb(Mg_{1/3}Nb_{2/3})O_3 - 0.33PbTiO_3$ (in short, 0.67PMN-0.33PT) thin film is shown in Fig. 4.26. Here, the linear behaviour of the imaginary part of specific resistance is observed in log-log scale. The slope is between –0.95 and –0.99, thus very close to –1. This result suggests that the imaginary part of the complex specific resistance is related to a capacitance as it is expected in the case of a ferroelectric capacitor. The similar behaviour of complex impedance was observed in BTO and PZT epitaxial thin films deposited on single crystal $SrTiO_3$ substrates with (001) and (111) orientations [D.42]. In order to gain more information about processes in the 0.67PMN-0.33PT thin film, the complex dielectric permittivity was calculated from complex specific resistance and is presented in the following figures.

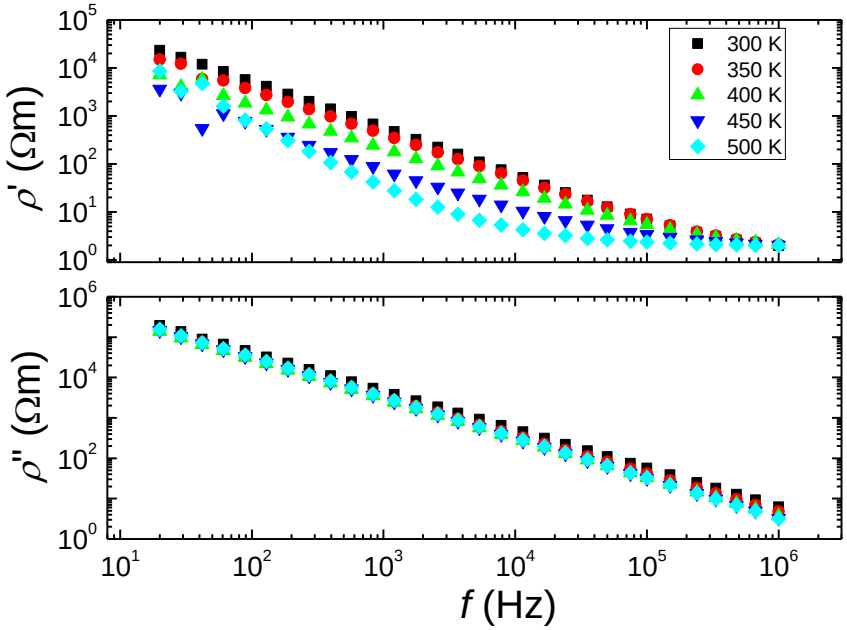

Fig. 4.26 Frequency dependence of the real and imaginary parts of specific impedance.

On purpose to avoid the influence of SRO conductivity, first of all mathematical corrections of experimental results were performed. Figure 4.27 shows the frequency dependences of the real and imaginary part of the complex dielectric permittivity before and after correction for the series resistance due to the SRO electrode, calculated from the measured specific impedance using Eq. 4.33.

$$\begin{aligned} \rho'_{\text{cor}} &= \rho'_{\text{exp}} - \rho_{\infty} \\ \rho''_{\text{cor}} &= \rho''_{\text{exp}} \end{aligned}, \tag{4.33}$$

here: ρ'_{cor} and ρ''_{cor} correspond to the real and imaginary parts of the corrected measured resistance, ρ'_{exp} and ρ''_{exp} corresponds to the experimental results of the real and imaginary parts of specific resistance and ρ_{∞} corresponds to serial resistance of SRO electrode.

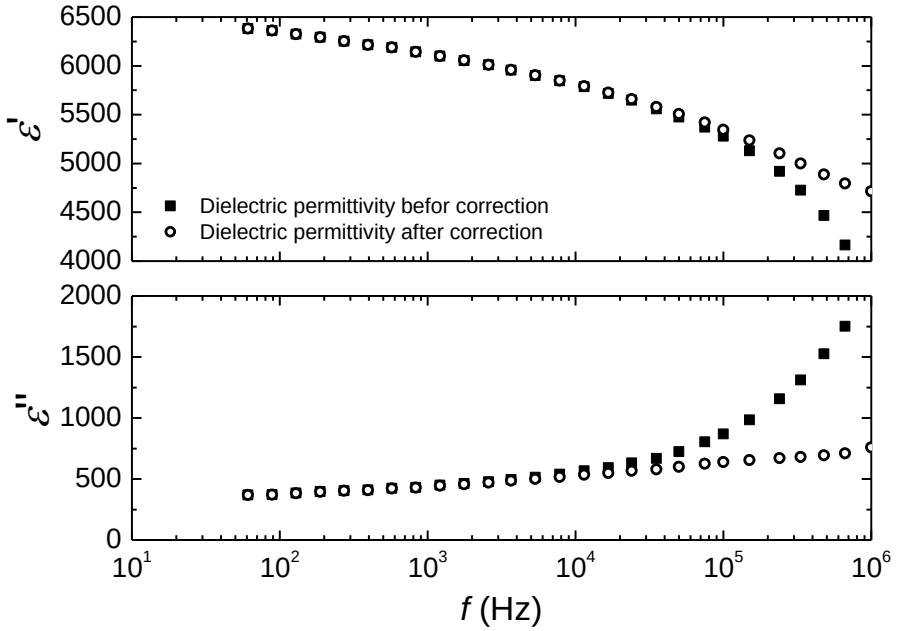

Fig. 4.27 Frequency dependence of the complex dielectric permittivity, before (black squares) and after (red dots) correction for the series resistance due to the electrodes.

Corrections at frequencies from 100 kHz were made by subtracting the constant value of serial resistance of SRO electrode ($\rho_\infty = 2\ \Omega$m), which was obtained during the experimental measurements. Dielectric permittivity was calculated using equations provided in section 3.1. It is obvious to see that after corrections, the change of the complex dielectric permittivity with frequency is strongly reduced at high frequencies (see Fig. 4.27). Therefore, presented mathematical correction was applied for experimental results at all temperature range.

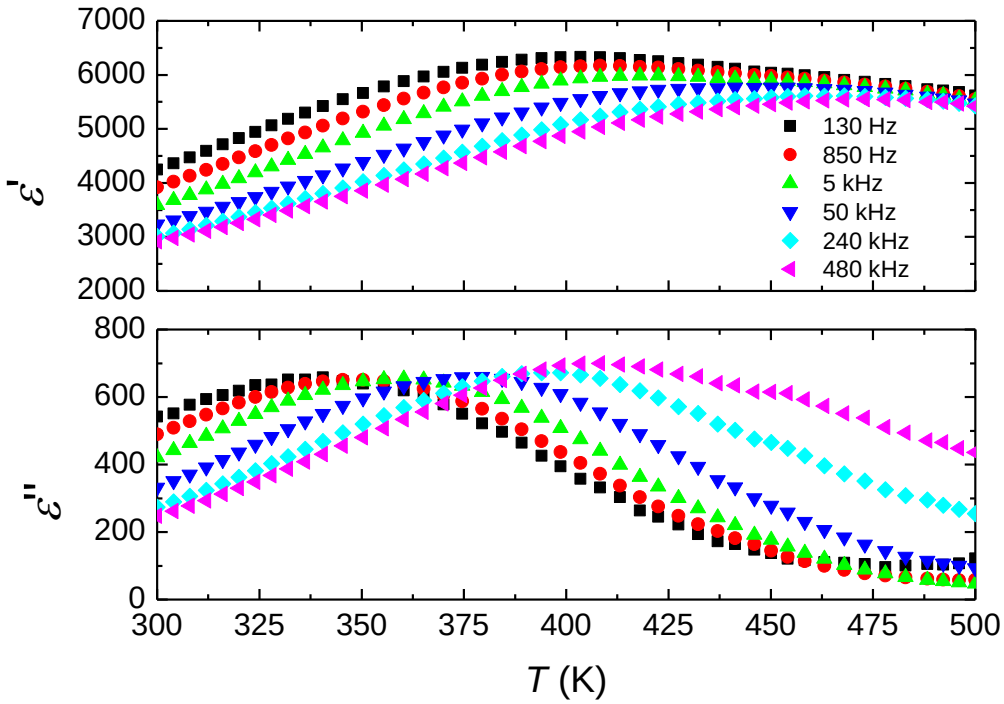

Fig. 4.28 Temperature dependence of complex dielectric permittivity after correction.

Dielectric permittivity recalculated from the complex resistivity, measured as a function of temperature at different frequencies are presented in Fig. 4.28. The real part of the dielectric permittivity shows two broad and overlapping dielectric anomalies: first one around T = 400 K and another around T = 480 K, which might indicate phase transitions from rhombohedral to tetragonal and from tetragonal to cubic phases, respectively. The dielectric constant of 0.67PMN-0.33PT thin film is approximately equal to 6000 at 1 kHz, which is almost five times smaller than in the case of a bulk 0.67PMN-0.33PT [D.43, D.44]. The decrease and flattening of dielectric permittivity observed in thin films might also be related to size effect, which was observed by *Zhao et al.* [D.10].

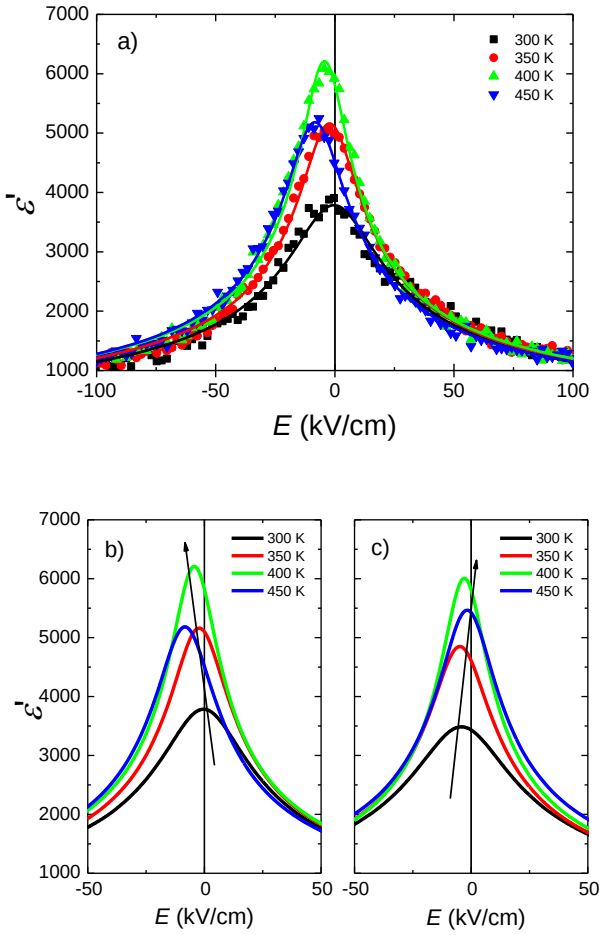

Fig. 4.29 a) Electric field tunability of the real part of the dielectric permittivity. Dots represent the experimental points and lines represent the Johnson approximation of the Landau-Ginsburg-Devonshire (see Eq. 3.203.203.20) b) and c) experimental results approximation when the field change was from positive to negative and vice versa, respectively.

The electric field tunability of the real part of the dielectric permittivity is presented in Fig. 4.29 a) in the temperature range 300 to 450 K. Dots represent the experimental points and lines represent the Johnson approximation of the Landau-Ginsburg-Devonshire (GLD) theory Eq. 3.20.

Fig. 4.29 b) and 4.29 c) represent the measured and fitted curves when the field is changed from positive to negative and vice versa, respectively (see Eq. 3.20). It is clearly seen that the position of the maximum of dielectric permittivity depends on the direction of the applied electric field. This might

be due to charge injection from bottom electrode to functional layer. Dielectric strength decreases more than 70 % at all temperatures after applied external voltage. It can be seen that dielectric constant is almost saturated at 100 kV/cm (5 V) and further decrease of the dielectric constant is not very likely.

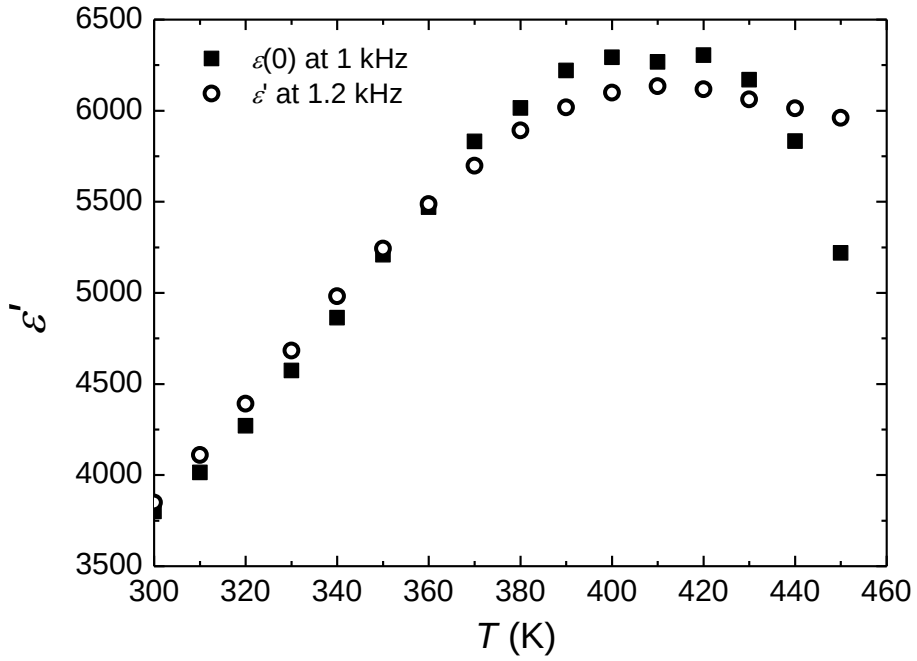

Fig. 4.30 Temperature dependence of the dielectric permittivity obtained from Johnson approximation in the Landau-Ginsburg-Devonshire theory (black squares) and from dielectric permittivity results after electrode resistivity correction (red squares).

In order to see the correlation between dielectric permittivity values obtained from electrical field tunability measurements at 0 kV/cm applied field and recalculated dielectric permittivity, both dependences were plotted in Fig. 4.30. Dielectric permittivity values differ less than 4 % almost at all measuring temperature range and only increases (difference is around 16 %) at temperatures above 440 K. Such low difference of dielectric permittivity values indicates that experimental results are reliable and repeatable, because complex impedance and electrical tunability measurements were performed at different time and with different measurement equipment.

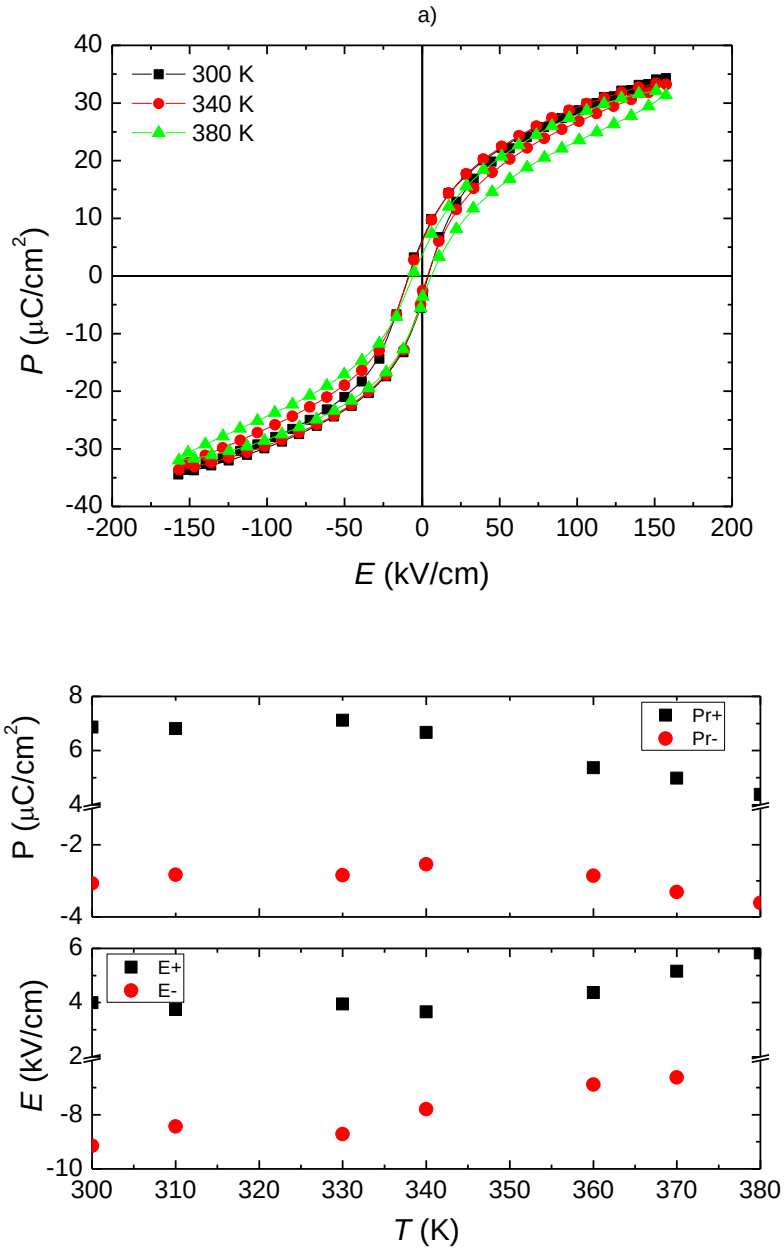

Fig. 4.31 a) Ferroelectric hysteresis curves of 0.67PMN-0.33PT thin film measured at 1 kHz frequency at different temperatures. b) Temperature dependence of remnant positive and negative (P_r+ and P_r- respectively) polarization and positive and negative coercive field (E+ and E- respectively).

Fig. 4.31 a) shows polarization-electric field (P-E) loops measured at 1 kHz frequency of the 0.67PMN-0.33PT thin film up to 150 kV/cm applied electric field. This 0.67PMN-0.33PT thin film shows a clear hysteresis property with a remnant polarization of $2P_r \approx 10$ μC/cm^2 and a coercive field

of $2E_c \approx 12$ kV/cm in the temperature range 300 - 380 K (see Fig. 4.31 b)). The shape of the hysteresis loop of 0.67PMN-0.33PT thin film is sloped and slim. These results correspond well with the results presented by *Wasa et al.* [D.45]. PMN-PT is a typical relaxor ferroelectric material which has nanodomain structure. The nanodomains of the relaxor can be oriented with the field leading to large polarization. However, most of these domains reacquire their random orientation resulting in a small remnant polarization when the applied electric field is removed [D.46, D.47].

4.3.3. Summary

Experimental investigations of $0.71Pb(Mg_{1/3}Nb_{2/3})O_3$-$0.29PbTiO_3$ single crystals and $0.67Pb(Mg_{1/3}Nb_{2/3})O_3$-$0.33PbTiO_3$ epitaxial thin film were presented. First of all, in the case of 0.71PMN-0.29PT single crystals, it was observed that during the heating cycle, the dielectric measurements show two phase transitions, i.e. an intermediate phase is observed, while the direct transition from rhombohedral to cubic phase involves large structural changes that are energetically not favourable. On the contrary, during the cooling cycle only one phase transition is observed i.e. the metastable phase is not detected, because the change of temperature is too fast (temperature rate was about 1 K/min). Secondly, the additional domain walls contribution to the total dielectric permittivity was observed. Dielectric permittivity value increased almost two times in the <001>-oriented 0.71PMN-0.29PT single crystal at the maximum position. Thirdly, due to the fact that the polarization component is perpendicular to the sample's surface in the tetragonal phase, the pyroelectric response was observed only for the <111> and <011>-oriented crystals, but not for the crystal oriented along <001> direction, because the dominant polarization component is parallel to the sample's surface.

In the case of $0.67Pb(Mg_{1/3}Nb_{2/3})O_3$-$0.33PbTiO_3$ epitaxial thin film the frequency dependencies of the real and imaginary parts of the specific impedance suggested that observed specific resistance might be related to a capacitance as it is expected in the case of a ferroelectric capacitor. Also, it was observed that experimental results of specific impedance are strongly

influenced by series resistance due to the SRO electrode. In order to reduce such an influence, mathematical corrections were applied before recalculation of dielectric permittivity. Secondly, after investigation of 0.67PMN-0.33PT epitaxial thin film, it was observed that the curves of dielectric permittivity are flattening and the values are much (almost five times) lower than in the case of bulk 0.67PMN-0.33PT materials. The behaviour of dielectric permittivity might also be related with a weakening of the ferroelectric properties due to the size effect like in the case of BST thin films. Nevertheless, I have showed that 0.67PMN-0.33PT epitaxial thin films is a good tunable material; dielectric strength decreases more than 70 % at all temperatures after applied external voltage. Also, dielectric constant is almost saturated at 100 kV/cm and further decrease of the dielectric constant is not very likely. Moreover, 0.67PMN-0.33PT is a better tunable material comparing with epitaxial $Ba_{0.7}Sr_{0.3}TiO_3$ / $La_{0.8}Sr_{0.2}MnO_3$ // $SrTiO_3$ heterostructure; observed electric field tunability is stronger around 1.4 times and in order to reach saturated dielectric constant, much lower fields are needed.

4.4. References

[D.1] **R. E. Collin**, Foundations for Microwave Engineering, Second Edition, Wiley-IEEE Press (2000): ISBN 978-0-7803-6031-0

[D.2] **L. Benguigui**, Disordered ferroelectrics: $Ba_xSr_{1-x}TiO_3$ single crystals. Phys. Status Solidi A 46 (1), 337 342 (1978): http://dx.doi.org/10.1002/pssa.2210460144

[D.3] **V.V. Lemanov, E.P. Smirnova, P.P. Syrnikov, and E.A. Tarakanov**, Phase transitions and glasslike behavior in $Sr_{1-x}Ba_xTiO_3$. Phys. Rev. B 54(5), 3151–3157 (1996): http://dx.doi.org/10.1103/PhysRevB.54.3151

[D.4] **C. Ménoret, J.M. Kiat, B. Dkhil, M. Dunlop, H. Dammak, and O. Hernandez**, Structural evolution and polar order in $Sr_{1-x}Ba_xTiO_3$. Phys. Rev. B 65(22), 224104 (2002): http://dx.doi.org/10.1103/PhysRevB.65.224104

[D.5] **E.P. Smirnova, A.V. Sotnikov, R. Kunze, M. Weihnacht, O.E. Kvyatkovskii, and V.V. Lemanov**, Interrelation of antiferrodistortive and ferroelectric phase transitions in $Sr_{1-x}A_xTiO_3$ (A=Ba, Pb). Solid State Commun. 133(7), 421–425 (2005): http://doi.org/10.1016/j.ssc.2004.12.016

[D.6] **F. Jonan ad G. Shirane**, Ferroelectric crystals. New York: Dover, 1993

[D.7] **A. von Hippel**, Ferroelectricity, Domain Structure, and Phase Transitions of Barium Titanate. Rev. Mod. Phys. 22, 221, (1950): https://doi.org/10.1103/RevModPhys.22.221

[D.8] **A. D. Hilton, and B. W. Ricketts**, Dielectric properties of $Ba_{1-x}Sr_xTiO_3$ ceramics. J. Phys. D: Appl. Phys. 29, 1321–1325 (1996): https://doi.org/10.1088/0022-3727/29/5/028

[D.9] **B. Su, and T. W. Button**, Microstructure and dielectric properties of Mg-doped barium strontium titanate ceramics. J. Appl. Phys., 95, 3 (2004): http://dx.doi.org/10.1063/1.1636263

[D.10] **Z. Zhao, V. Buscaglia, M. Viviani, M.T. Buscaglia, L. Mitoseriu, A. Testino, M. Nygren, M. Johnsson, and P. Nanni**, Grain-size effects on the ferroelectric behavior of dense nanocrystalline $BaTiO_3$ ceramics. Phys. Rev. B 70, 024107 (2004): http://dx.doi.org/10.1103/PhysRevB.70.024107

[D.11] **T. M. Shaw, Z. Suo, M. Huang, E. Liniger, R. B. Laibowitz, and J. D. Baniecki**, The effect of stress on the dielectric properties of barium strontium titanate thin films. Appl. Phys. Lett., 75, 14 (1999): http://dx.doi.org/10.1063/1.124939

[D.12] **Z.-G. Ban, and S. P. Alpay**, Phase diagrams and dielectric response of epitaxial barium strontium titanate films: A theoretical analysis. J. Appl. Phys., 91, 11 (2002): http://dx.doi.org/10.1063/1.1473675

[D.13] **P. Padmini, T. R. Taylor, M. J. Lefevre, A. S. Nagra, R. A. York, and J. S. Speck**, Realization of high tunability barium strontium titanate thin films by rf magnetron sputtering. Appl. Phys. Lett., 75, 20 (1999): http://dx.doi.org/10.1063/1.125272

[D.14] **G. Koster, B.L. Kropman, G.J.H.M. Rijnders, D.H.A. Blank, and H. Rogalla**, Quasi-ideal strontium titanate crystal surfaces through formation of strontium hydroxide. Appl. Phys. Lett. 73, 20, 2920 – 2922 (1998): http://dx.doi.org/10.1063/1.122630

[D.15] **J. A. Basmajian, R. C. DeVries**, Phase Equilibria in the System $BaTiO_3$–$SrTiO_3$. J. Am. Ceram. Soc. 40, 373 (1957): http://dx.doi.org/10.1111/j.1151-2916.1957.tb12556.x

[D.16] **S. Bagdzevicius, R. Mackeviciute, M. Ivanov, B. Fraygola, C. S. Sandu, N. Setter, and J. Banys**, Internal electrical and strain fields influence on the electrical tunability of epitaxial $Ba_{0.7}Sr_{0.3}TiO_3$ thin films. Appl. Phys. Lett. 108, 132901 (2016): http://dx.doi.org/10.1063/1.4944997

[D.17] **O. Lee, S. a. Harrington, A. Kursumovic, E. Defay, H. Wang, Z. Bi, C.-F. Tsai, L. Yan, Q. Jia, and J.L. MacManus-Driscoll**, Extremely High Tunability and Low Loss in Nanoscaffold Ferroelectric Films. Nano Lett. 12, 4311 (2012): http://dx.doi.org/10.1021/nl302032u

[D.18] **L. Benguigui**, Disordered ferroelectrics: $Ba_xSr_{1-x}TiO_3$ single crystals. Phys. Status Solidi A 46(1), 337–342 (1978): http://dx.doi.org/10.1002/pssa.2210460144

[D.19] **V.B. Shirokov, V.I. Torgashev, A.A. Bakirov, and V.V. Lemanov**, Concentration phase diagram of $Ba_xSr_{1-x}TiO3$ solid solutions. Phys. Rev. B 73(10), 104116 (2006): http://dx.doi.org/10.1103/PhysRevB.73.104116

[D.20] **R. Mackevičiūtė, Š. Bagdzevičius, M. Ivanov, B. Fraygola, R. Grigalaitis, N. Setter, and J. Banys**, Strain engineering of electrical conductivity in epitaxial thin $Ba_{0.7}Sr_{0.3}TiO_3$ film heterostructures. Lith. J. Phys. 56, 173–181 (2016): http://dx.doi.org/10.3952/physics.v56i3.3366

[D.21] **J.W. Matthews and A.E. Blakeslee**, Defects in epitaxial multilayers: I. Misfit dislocations. J. Cryst. Growth 27, 118–125 (1974): http://dx.doi.org/10.1016/S0022-0248(74)80055-2

[D.22] **J.Q. He, E. Vasco, C.L. Jia, R. Dittmann, and R.H. Wang**, Microstructure of epitaxial $Ba_{0.7}Sr_{0.3}TiO_3/SrRuO_3$ bilayer films on $SrTiO_3$ substrates. J. Appl. Phys. 97(10), 104907 (2005): http://dx.doi.org/10.1063/1.1897067

[D.23] **Y. Fan, S. Yu, R. Sun, L. Li, Y. Yin, K.-W. Wong, and R. Du**, Microstructure and electrical properties of Mn-doped barium strontium titanate thin films prepared on copper foils. Appl. Surf. Sci. 256(22), 6531–6535 (2010): http://dx.doi.org/10.1016/j.apsusc.2010.04.042

[D.24] **P.-E. Janolin, A.S. Anokhin, Z. Gui, V.M. Mukhortov, Y.I. Golovko, N. Guiblin, S. Ravy, M.E. Marssi, Y.I. Yuzyuk, L. Bellaiche, and B. Dkhil**, Strain engineering of perovskite thin films using a single substrate. J. Phys. Condens. Matter 26(29), 292201 (2014): http://dx.doi.org/10.1088/0953-8984/26/29/292201

[D.25] **A. A. Bokov, and Z.-G. Ye**, Recent progress in relaxor ferroelectrics with perovskite structure. J. Mater. Sci. 41, 31–52 (2006): http://dx.doi.org/10.1007/s10853-005-5915-7

[D.26] **G. Shirane, and S. Hoshino,** On the Phase Transition in Lead Titanate. J. Phys. Soc. Jpn. 6, 265 (1951): http://dx.doi.org/10.1143/JPSJ.6.265

[D.27] **D. Zekria, and A. M. Glazer**, Automatic determination of the morphotropic phase boundary in lead magnesium niobate titanate $Pb(Mg_{1/3}Nb_{2/3})_{(1-x)}Ti_xO_3$ within a single crystal using birefringence imaging. J.

Appl. Cryst., 37, 143-149 (2004): https://doi.org/10.1107/S002188980302733X

[D.28] **H. Fu, and R. E. Cohen**, Polarization rotation mechanism for ultrahigh electromechanical response in single-crystal piezoelectrics. Nature. 403, 281–283 (2000): https://doi.org/10.1038/35002022

[D.29] **M. Davis, D. Damjanovic, and N. Setter**, Pyroelectric properties of (1-x)$Pb(Mg_{1/3}Nb_{2/3})O_3$-x$PbTiO_3$ and (1-x)$Pb(Zn_{1/3}Nb_{2/3})O_3$-x$PbTiO_3$ single crystals measured using a dynamic method. J. Appl. Phys. 96, 5(2004): https://doi.org/10.1063/1.1775308

[D.30] **P. Kumar, S. Singh, O. P. Thakur, C. Prakash, and T. C. Goel**, Effect of compositional modifications of dielectric, ferroelectric and pyroelectric response of PMN-PT solid solutions near MPB. Modern Physics Letters B. 20, 21, 1335–1342 (2006): https://doi.org/10.1142/S0217984906011359

[D.31] **X. Zhao, B. Fang, H. Cao, Y. Guo, and H. Luo**, Dielectric and piezoelectric performance of PMN-PT single crystals with compositions around the MPB: influence of composition, poling field and crystal orientation. Materials Science and Engineering B96, 254–262 (2002): http://dx.doi.org/10.1016/S0921-5107(02)00354-9

[D.32] **W. Guo, D. Jin, W. Wei, and H. J. Maris, J. Tian, X. Huang, and P. Han**, Low temperature piezoelectric and dielectric properties of lead magnesium niobate titanate single crystals. J. Appl. Phys. 102, 084104 (2007): http://dx.doi.org/10.1063/1.2798879

[D.33] **K. Wasa, I. Kanno, T. Suzuki, S. H. Seo, D. Y. Noh, H. Okino, and T. Yamamoto**, Structure and Ferroelectric Properties of Sputtered PMNT Thin Films. 2004 IEEE International Ultrasonics, Ferroelectrics, 12 and Frequency Control Joint 50th Anniversary Conference: https://doi.org/10.1109/ISAF.2004.1418326

[D.34] **K. Wasa, S. H. Seo, D. Y. Noh, I. Kanno and T. Suzuki**, Heteroepitaxial growth of stress free single crystal perovskite thin films. Surf. Rev. Lett. 13, 167 (2006): http://dx.doi.org/10.1142/S0218625X06008189

[D.35] **K. Wasa, I. Kanno and T. Suzuki**, Structure and Electromechanical Properties of Quenched PMN-PT Single Crystal Thin Films. Advances in Science and Technology 45, 1212-1217 (2006): http://dx.doi.org/10.4028/www.scientific.net/AST.45.1212

[D.36] **S. H. Seo, H. C. Kang, D. Y. Noh, Y. Yamada, and K. Wasa**, Antiphase-type planar defects in $Pb(Mg_{1/3}Nb_{2/3-\delta})O_3/SrTiO_3$thin films. Appl. Phys. Lett., 84, 16 (2004): http://dx.doi.org/10.1063/1.1710714

[D.37] **M. Boota, E. P. Houwman, M. Dekkers, M. Nguyen, and G. Rijnders**, Epitaxial $Pb(Mg_{1/3}Nb_{2/3})O_3$-$PbTiO_3$ (67/33) thin films with large tunable self-bias field controlled by a $PbZr_{1-x}Ti_xO_3$ interfacial layer. Appl. Phys. Lett. 104, 182909 (2014): http://dx.doi.org/10.1063/1.4874978

[D.38] **M. D. Nguyen, H. Nazeer, K. Karakaya, S. V. Pham, R. Steenwelle, M. Dekkers, L. Abelmann, D. H. A. Blank, and G. Rijnders, J. Micromech**, Characterization of epitaxial $Pb(Zr,Ti)O_3$ thin films deposited by pulsed laser deposition on silicon cantilevers. J. Micromech. Microeng. 20, 085022, 11pp (2010): https://doi.org/10.1088/0960-1317/20/8/085022

[D.39] **Y. Tang, L. Luo, Y. Jis, H. Luo, X. Zhao, H. Xu, D. Lin, J. Sun, X. Meng, J. Zhu, and M. Es-Souni**, Mn-doped $0.71Pb(Mg_{1/3}Nb_{2/3})O_3$-$0.29PbTiO_3$ pyroelectric crystals for uncooled infrared focal plane arrays applications. Appl. Phys. Lett. 89, 162906 (2006): http://dx.doi.org/10.1063/1.2363149

[D.40] **H. Katzke, M. Dietze, A. Lahmar, M. Es-Souni, N. Neumann, and S.-G. Lee**, Dielectric, ultraviolet/visible, and Raman spectroscopic investigations of the phase transition sequence in $0.71Pb(Mg_{1/3}Nb_{2/3})O_3$-$0.29PbTiO_3$ crystals. Phys. Rev. B. 83, 174115 (2011): https://doi.org/10.1103/PhysRevB.83.174115

[D.41] **B. L. Cheng, M. Gabbay, M. Maglione, Y. Jorand, and G. Fantozzi**, Domain Walls Motions in Barium Titanate Ceramics. J. Phys. IV. 6, C8 (1996): https://doi.org/10.1051/jp4:19968139

[D.42] **L. Pintilie, L. Hrib, I. Pasuk, C. Ghica, A. Iuga, and I. Pintilie**, General equivalent circuit derived from capacitance and impedance

measurements performed on epitaxial ferroelectric thin films. J. Appl. Phys. 116, 044108 (2014): http://dx.doi.org/10.1063/1.4891255

[D.43] **C.B. DiAntonio, F.A. Williams, S.M. Pilgrim, W.A. Schulze**, Characterization study of the growth and electromechanical properties of 67PMN-33PT single crystals. Proceedings of the 13th IEEE International Symposium on Applications of Ferroelectrics, 2002. ISAF 2002: https://doi.org/10.1109/ISAF.2002.1195960

[D.44] **M. Pham-Thi, C. Augier, H. Dammak, P. Gaucher**, Fine grains ceramics of PIN–PT, PIN–PMN–PT and PMN–PT systems: Drift of the dielectric constant under high electric field. Ultrasonics 44, e627–e631 (2006): http://dx.doi.org/10.1016/j.ultras.2006.05.017

[D.45] **K. Wasa, I. Kanno and T. Suzuki**, Structure and Electromechanical Properties of Quenched PMN-PT Single Crystal Thin Films. Advances in Science and Technology, 45, 1212-1217 (2006): http://dx.doi.org/10.4028/www.scientific.net/AST.45.1212

[D.46] **G. A. Samara**, The relaxational properties of compositionally disordered ABO_3 perovskites. J. Phys.: Condens. Matter, 15, 9, R367–R411 (2003): https://doi.org/10.1088/0953-8984/15/9/202

[D.47] **S. B. Vakhrushev, A. A. Naberezhnov, B. Dkhil, J. M. Kiat, V. Shwartsman, A. Kholkin, B. Dorner, and A. Ivanon**, Structure of Nanodomains in Relaxors. Fundamental Physics of Ferroelectrics, 677, 74–83 (2003): https://doi.org/10.1063/1.1609940

5. Conclusions

This thesis describes an experimental investigation of epitaxial thin films and single crystals. The following conclusions are obtained:

1. The model of a thin dielectric film with a bottom electrode of negligible distributed resistance describes experimental data of complex heterostructure in a physically proper way, unlike equivalent circuit model.
2. The misfit strain influences the ferroelectric phase transition temperature and the activation energy of charge carrier mobility: the phase transition temperature enhances, while activation energy diminishes with the increase of misfit strain.
3. The values of dielectric permittivity of epitaxial BST 70/30 and 0.67PMN-0.33PT thin films are strongly suppressed comparing with their bulk equivalent; the curves of dielectric permittivity are flattening – the clear and characteristic dielectric anomaly is not observed.
4. Built in electric and misfit strain fields does not deteriorate dielectric tunability in the case of epitaxial thin films – observed tunability was decreasing more than 50 % and 70 % at all temperatures in the cases of BST 70/30 and 0.67PMN-0.33PT thin films, respectively.